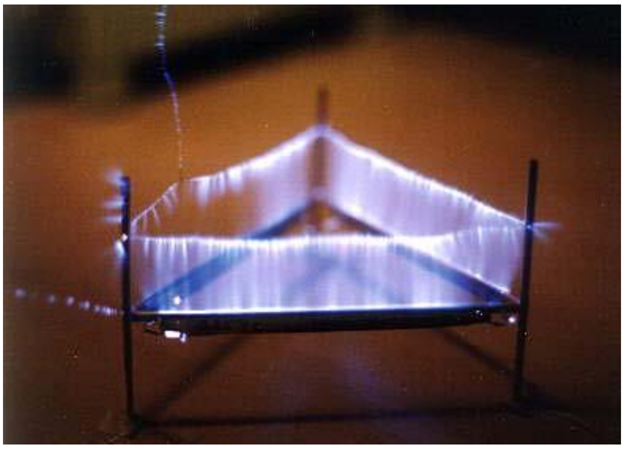

A contribution to a better understanding of EHD thrusters in order to optimize their construction and adequate operation conditions

Eduardo Calvo
Mestrado Integrado em Engenharia Física
Departamento de Física e Astronomia, FCUP
Departamento de Engenharia Física, FEUP
2020

Orientador
Paulo de Araújo Sá, PhD
Professor Associado, Departamento de Engenharia Física e
Centro de Estudos de Fenómenos de Transporte,
Faculdade de Engenharia da Universidade do Porto

ceft
TRANSPORT PHENOMENA RESEARCH CENTER

U.PORTO
FEUP FACULDADE DE ENGENHARIA
UNIVERSIDADE DO PORTO

U.PORTO
FC FACULDADE DE CIÊNCIAS
UNIVERSIDADE DO PORTO

Todas as correções determinadas pelo júri, e só essas, foram efetuadas.

O Presidente do Júri,

Porto, ______/______/_________

‘It is possible that in time, we may use electricity to produce

a large velocity for the particles ejected from a rocket device."

Konstantin Tsiolkovsky, 1911

Acknowledgements

First and foremost, I would like to express my deepest gratitude to my supervisor, professor Paulo Araújo Sá. You were always receptive to help me whenever I had questions or simulation troubles during the research. I would like to extend the vote of gratitude to professor Mário Pinheiro, scientific advisor of this work, for the patience and valuable insights.

A word of acknowledgement to the *Centro de Estudos de Fenómenos de Transporte* (CEFT), and the Department of Engineering Physics, DEF, both from the Faculty of Engineering, for their financial support and for the computational facilities, respectively.

To all my friends, a word of appreciation, without them I couldn't be who I am today. Without the experiences, the tea sessions, the night sessions, the adventure of fighting in dungeons to defeat some dragons. To my longest friend just one word, I guess you have luck in love, because at gambling, you are just a stain. To my girl in arms, Rita, I just want to acknowledge that without you, this thesis wouldn't be possible.

A special word to all of my family, to my uncle Paulo I wish you to say that I grew a lot with our conversations. To my parents, Eduardo and Felismina and to my sister, Sara, thank you for the eternal and unconditional support.

Muito Obrigado.

Abstract

In this present study dedicated to EHD propellants, we continued and developed the work started with a doctoral thesis of 2018. We considered a needle-shaped anode, a cylindrical cathode, and two working gases, argon and xenon, and applying a pressure of 10 $Torr$.

In this work, we started by investigating the consistency of the appropriate volume force term used on the Navier-Stokes equation in a plasma medium. In the current state-of-art there is some confusion in writing this term, and although all density force terms give practically the same results regarding thruster parameters, for physical consistency and computational time, it is advised the use of the space charge density term.

In the second part of this work, we studied the influence of the discharge parameters such as the variation of the ballast resistor, variation of the applied voltage and secondary electron emission coefficient, γ_i. We reported that by increasing the discharge current, the net thrust would increase as well, with a linear tendency. On the opposite, by increasing γ_i, the output thrust decreases, confirming what's in the literature about this subject. Using the experimental coefficients measured for copper surfaces, we reach an output thrust of 2.75 μN and efficiency of 259mN/kW for the case of Ar and an output thrust of 3.80μN and efficiency of 434mN/kW for the Xe.

In terms of geometry, we began by changing the hollow radius of the cathode. Using argon, we verified that this parameter was already optimized in 12mm, since any other variation, upper or lower, would decrease the output thrust and the thruster efficiency. On the opposite hand, when using xenon, we concluded that the optimal hollow radius was 20mm since it was the one who produced better thruster results. Then, we proceeded to verify the influence of the cathode's cylinder height. At 20kV, we discovered that for Ar, the Cathode's height should be halved, to around 10.5mm, and that for the Xe, the cathode's height should be reduced by about 30%, i.e. to 14.7mm, from what was used by Granados (2018).

Finally, it was investigated the dual stage thruster. It was started by exploring the sliding effect of the electric field in a dielectric surface by introducing a chimney shape dielectric beneath the cathode, using Argon as propellant. With the increase of the aperture angle, the morphology of the electric potential and field lines inside the cathode are changed and the species distributions vary as well. In these circumstances, there is an increase of the net thrust. We observed that at 9 kV, the thrust output is higher, given 500 nN (with a cathode of 10.5 mm), a 2 times increase, regarding the same single stage EHD thruster without the dielectric chimney. Then we modulated two distinct set of electrodes geometries.

Keywords

electric propulsion, electrohydrodynamic thrusters, plasma discharge, modelling plasma fluids, sliding effect, dual-stage thrusters.

Resumo

Neste estudo dedicado a propulsores EHD, demos continuação e desenvolvimento ao trabalho começado com uma tese de douturamento de 2018. Consideramos um ânodo em forma de agulha, um cátodo cilindrico e usamos dois gases de trabalho, o argon e o xenon, admitindo uma pressão de 10 $Torr$.

Neste trabalho, começamos por investigar a consistência do termo da força volúmica apropriado usado na equação de Navier-Stokes em plasmas. Na bibliografia mais recente há alguma confusão na correta determinação deste termo e , apesar de todos os termos de densidade de força darem resultados semelhantes no que toca aos parâmetros dos propulsores, por uma questão de consistência física e computacional, aconselha-se o uso do termo de força com a densidade de carga do espaço.

Numa segunda parte do nosso estudo, analisamos a influencia de parâmetros de descarga como a variação da resistência de balastro, da tensão aplicada e do coeficiente de emissão de eletrões secundários, γ_i. Com isto reportamos que com o aumento da corrente de descarga, também a força de propulsão aumentava, seguindo uma tendência linear. Pelo contrário, reparamos que, ao aumentar o coeficiente de emissão de eletrões secundários, a propulsão diminuía, facto corroborado pela literatura disponível. Usando os coeficientes experimentais medidos para superfícies de cobre, obtivemos um impulso de 2.75 μN com uma eficiência de 259mN/kW no caso do Ar e um impulso de 3.80 μN e eficiência de 434mN/kW no caso do Xe.

No que diz respeito à geometria, e usando um cátodo cilindrico, começamos por alterar os valores do raio do cátodo. Aquando da utilização do Árgon, verificamos que este valor já se encontrava otimizado em 12mm, valor resultante de um estudo anterior da equipa, uma vez que qualquer variação, para maior ou menor, a força de propulsão diminuía bem como a eficiência do propulsor. No entanto, quando usamos o Xénon, conseguimos concluir que o raio de cátodo ótimo era de 20mm, sendo este o valor que produzia melhores impulso de saída e eficiência.

De seguida verificamos a influencia da altura do cilindro nos parâmetros finais do propulsor. A 20kV, aferimos que, para o Ar, a altura do cilindro devia ser reduzida para metade do proposto na literatura, ou seja para cerca de 10,5mm, enquanto que, para o Xe, deveria ser reduzida em cerca de 30%, para 14,7mm, comparado o usado po Granados (2018).

Finalmente investigamos um propulsor de dois estágios. Começamos por explorar o efeito de deslize do plasma numa superfície dielétrica, introduzindo um componente dielétrico em forma de chaminé por baixo do nosso cátodo. Para este estudo foi utilizado o Árgon como gás propulsor. Com o aumento do ângulo da abertura deste cone, tanto a morfologia do potencial elétrico como as linhas de campo dentro do cátodo alteraram-se, notando-se também a variação da distribuição das diferentes espécies iónicas. Nestas circunstancias deu-se então um aumento da propulsão. Observamos que a 9kV, o impulso de saída é superior, com 500nN (com um cátodo de 10,5mm), dá-se um aumento de cerca de 2 vezes em relação ao propulsor EHD simples. Para finalizar esta parte do estudo modulamos dois conjuntos distintos de geometrias dos elétrodos.

Palavras-chave

propulsão eléctrica, propulsores eletrohidrodinâmicos, descarga de plasmas, modelaçáo de fluídos, efeito de deslize, propulsores de dois estágios.

Contents

List of Figures

List of Tables

List of Abbreviations

Ar	neutral argon atom
EHD	electrohydrodynamic
EP	electric propulsion
FEM	finite-element method
$f_M(\epsilon)$	Maxwellian distribution function
GEO	geostationary-equatorial orbit
LEO	low-earth orbit
$\sigma_j(\epsilon)$	cross-section data
Xe	neutral xenon atom

α	ionization per unit length coefficient
C_b	blocking capacitor, F
dm_g	expelled mass gas, kg
dt	infinitesimal interval of time, s
η	gas dynamic viscosity, Pa · s
ε	plasma permittivity, F · m^{-1}
ε_0	vacuum permittivity, F · m^{-1}
ε_r	relative permittivity
γ_i	secondary electron emission coefficient
I_d	discharge current, A
I_{sp}	specific impulse s
k_B	Boltzmann constant, J · K^{-1}
k_j	rate coefficient, m^{-3} · s^{-1}

l_c	cathode's length, m
m	instantaneous rocket mass, kg
m_0	system initial mass, kg
m_f	final burnout mass, kg
m_p	consumed mass, kg
n_e	electron density, m^{-3}
n_ε	electron energy density, e · V · m^{-3}
n_i	ion density, m^{-3}
n_j	ion density for j-species, m^{-3}
ω_c	electron cyclotron frequency, rad · s^{-1}
ω_k	mass fraction of k-species
ω_{rf}	electric field frequency, rad · s^{-1}
p	absolute pressure, Pa
P	power, W
P_{plasma}	power spent on plasma, W
R_b	ballast resistor, Ω
ρ_c	space charge density, C · m^{-3}
ρ_f	main gas mass density, kg · m^{-3}
ρ_i	ion charge density, C · m^{-3}
r_i	inner radius, m
t	instant time, s
T	thrust, N
T_e	electron temperature, e · V
T_{gas}	gas temperature, K
T_i	ion temperature, K
$T/Pratio$	thrust-to-power ratio (TPR), N/W
V_B	breakdown voltage, V
V_{in}	input voltage, V
Z_j	ion charge number

$\mathbf{B}$	Magnetic flux density vector, T.
$\Delta\mathbf{v}$	increment velocity, $\mathrm{m \cdot s^{-1}}$
$d\mathbf{P}$	variation of linear momentum, $\mathrm{kg \cdot m \cdot s^{-1}}$
$d\mathbf{v}$	infinitesimal velocity, $\mathrm{m \cdot s^{-1}}$
$\mathbf{E}$	Electric field vector, $\mathrm{V \cdot m^{-1}}$
$\mathbf{f}$	Density force, $\mathrm{N \cdot m^{-3}}$
$\mathbf{f}_c$	Coulomb density force $\mathrm{N \cdot m^{-3}}$
$\mathbf{F}_{ext}$	external forces, N
$\mathbf{f}_i$	Ion space charge density force, $\mathrm{N \cdot m^{-3}}$
$\mathbf{f}_\nabla$	density gradients force, $\mathrm{N \cdot m^{-3}}$
$\mathbf{\Gamma}_e$	Electron flux
$\mathbf{\Gamma}_\varepsilon$	Electron energy flux vector
$\mathbf{\Gamma}_i$	Ion density flux
$\mathbf{\Gamma}_k$	Diffusive flux vector
$\mathbf{J}$	Total current density vector, $\mathrm{A \cdot m^{-3}}$
$\mathbf{J}_e$	Electron current density vector, $\mathrm{A \cdot m^{-3}}$
$\mathbf{J}_i$	Ion current density vector, $\mathrm{A \cdot m^{-3}}$
$\mathbf{n}$	normal vector of a surface
$\mathbf{P}_f$	final linear momentum, $\mathrm{kg \cdot m \cdot s^{-1}}$
$\mathbf{P}_i$	initial linear momentum, $\mathrm{kg \cdot m \cdot s^{-1}}$
$\mathbf{r}$	position vector, m
$\mathbf{v}$	instantaneous rocket velocity regarding Earth referential, $\mathrm{m \cdot s^{-1}}$
$\mathbf{v}_{ex}$	exhaust velocity regarding Earth referential, $\mathrm{m \cdot s^{-1}}$
$\mathbf{v}_f$	final velocity, $\mathrm{m \cdot s^{-1}}$
$\mathbf{v}_g$	exhaust velocity regarding rocket referential, $\mathrm{m \cdot s^{-1}}$
$\mathbf{v}_i$	initial velocity, $\mathrm{m \cdot s^{-1}}$
$\mathbf{u}$	Main fluid velocity, $\mathrm{m \cdot s^{-1}}$
$\mathbf{u}_e$	electron mean velocity, $\mathrm{m \cdot s^{-1}}$
$\mathbf{u}_i$	ion mean velocity, $\mathrm{m \cdot s^{-1}}$

$\mathbf{D}_e$	electron diffusivity tensor, $\mathrm{m^2 \cdot s^{-1}}$
$\mathbf{D}_\varepsilon$	electron energy diffusivity tensor, $\mathrm{m^2 \cdot s^{-1}}$
$\mathbf{I}$	identity rank two tensor
$\widetilde{\boldsymbol{\mu}}_e$	electron mobility tensor, $\mathrm{m^2 \cdot V^{-1} \cdot s^{-1}}$
$\widetilde{\boldsymbol{\mu}}_\varepsilon$	electron energy mobility tensor, $\mathrm{m^2 \cdot V^{-1} \cdot s^{-1}}$
$\mathbb{T}$	electrostatic pressure rank two tensor

Chapter 1.

Introduction

1.1 MOTIVATION

Electric Propulsion (EP) is an alternative type of rocket propulsion since it is more efficient at long operation manoeuvring in comparison to the old and conventional chemical propulsion. It has become a well-established technology for moving small satellites, such as CubeSats and spacecrafts in space (Levchenko et al. (2018)). Electrically powered spacecraft propulsion systems make use of electrical energy to accelerate a propellant by different electrical and/or magnetic means. Plasma thrusters are usually classified into three main categories, according to their thrust generation processes: electrothermal, electrostatic, and electromagnetic. These three groups, along with the associated plasma discharge and energy transfer mechanisms, include long-standing technologies such as arc-jet thrusters, magnetohydrodynamics thrusters, and ion engines, as well as Hall thrusters and variants thereof (Keidar et al. (2014)).

The underlying theory of Electrohydrodynamic (EHD) phenomena relies on the fact that charged species drift due to an applied electric field, and as a consequence of a voltage drop between and anode and a cathode, and the resulting momentum transfer through collisions with the surrounding neutral species. Thus, a force, called the thrust, is exerted on the space vehicle through the ejection of, usually, a working gas (air, xenon, argon, nitrogen, or others) generally containing high kinetic energy. This force was first observed and studied by Thomas Townsend Brown and by Paul Alfred Biefeld when they observed, in 1929, the appearance of a net mechanical force in a Coolidge X-Ray tube when its asymmetrical electrodes were applied to an high-voltage source, becoming known as the Biefeld-Brown effect (Fylladitakis et al. (2014)). An electrical engine, such an EHD thruster, with a partially ionized plasma as the working gas, is fuel-efficient but at the expense of electrical power to sustain the plasma formation and ensuing gas acceleration.

Usually, the design of a thruster is a little bit challenging, since its fundamental physics is very complex due to the combination of fluid mechanics, plasma physics, and chemistry. So to produce a EHD thruster it is necessary to predict the flow pattern from the electrode geometry and the electric field profile but it is important to have in mind that the discharge regime and structure are also closely connected to the electric field and to the shape of the electrodes.

In a previously study, developed under a PhD program in our team, a numerical model was used to investigate the performance (e.g., thrust, thrust-to-power ratio, fluid velocity) of a single-stage EHD device with a needle-shaped anode and different cathode geometries. Using this model, the behaviour of various EHD thrusters under different conditions (pressure, temperature, electrode geometry, working gas, etc.) were investigated by Granados (2018). The set of equations and processes assumed in the model were numerically solved with a finite-element method, creating a mesh of points in the domain of simulation where differential equations are solved, while considering the appropriate boundary conditions for the problem. The simulations are done by the COMSOL Multiphysics@ software with a time-dependent solver in order to achieve steady-state solutions for each case study.

1.2 OBJECTIVES

The first goal of the present project is to improve the knowledge and optimize the behaviour of argon (Ar) propellant EHD thrusters by studying the external force term in the fluid model equation and the influence of cathode geometry, (dimensions of the cylindrical cathode), or increase of the ballast resistor, using gas pressure, gas temperature and secondary emission coefficient as in the model of Granados et al. (2017). It will also be point of study, the influence of adding a dielectric chimney at the entry of cylindrical cathode which by theory will modify the morphology of equipotential lines, which can increase the local electric field.

The second goal of the present project is to study the effect of xenon gas in EHD thrusters, by analysing the effects of several key conditions on the performance of an EHD propeller in order to optimize their construction and their adequate operation conditions. As with argon the key to access the behaviour this working gas, is a research of the efficiency of several parameters (thrust, thrust to power ratio, discharge current, peak velocity, spatial velocity profile, electron and ion densities, among others). The working gas considered will be mainly Xe, the commonly used propellant, and the results will be displayed due to the variation of gas pressure and temperature. We will study the influence of secondary electron emission from the cathode and the distance between the electrodes on performance parameters over a wide range of values. It will also be interesting and will be done latter on this work, to compare the behaviour of Xe propellers with those using Ar.

The third and final goal of the project is to widen the scope investigation to dual-stage electrode acceleration, using now the argon as the working gas. The design of the two-stage thruster shall allow separate control of ionization and acceleration, thereby controlling thrust force and specific thrust.

1.3 CONTRIBUTIONS TO THE FIELD OF WORK

With this work, we developed several contributions regarding the electrohydrodynamic thrusters. For instance, we verify the size of the thruster geometry, we verify the plasma-sliding effect using a dielectric slab, we explore two propellant gases. Also we present some enlightenment, regarding the external force term that should be used when modulating and simulating electrohydrodynamic processes.

Throughout the dissertation period, the author presented and will present several communications, both at national and international level, through oral and poster sections in the following conferences:

1. *"A contribution to a better understanding of EHD thrusters in order to optimize their construction and adequate operation conditions"* in 13^{th} Meeting of Young Researchers of University of Porto, IJUP-2020 (University of Porto), Porto, Portugal, Jan. 2020.

2. *"A contribution to a better understanding of EHD thrusters: study of the external force term"* in XXV Europhysics Conference on Atomic and Molecular Physics of Ionized Gases,

ESCAMPIG-2020 (European Physical Society), Paris, France, July 15-18, 2020

3. *"Optimizing the parameters of an electrohydrodynamic thruster plasma model"* in 9^{th} International Workshop & Summer School on Plasma Physics, IWSSPP-2020, Kitten, Bulgaria (data postponed).

4. *"Modelling the argon plasma-sliding EHD thruster at low pressure"* in 22^{nd} National Conference of Physics, SPF-2020 (Portuguese Physical Society), Lisbon, Portugal, Set. 2-5, 2020.

5. *"Optimizing an EHD cylindrical plasma thruster"* in 73^{rd} Annual Gaseous Electronics Conference, GEC-2020 (American Physical Society), San Diego, USA, Oct. 5-9, 2020.

6. *"Modulation of an argon propellant dual stage cylindrical electrohydrodynamic thruster at low pressure"* in 2020 Annual Conference UT-Austin, Matosinhos, Portugal, Oct. 8, 2020.

7. *"Modelling and optimizing an electrohydrodynamic thruster at low pressure"* in 7^{th} Space Propulsion Conference, SPC-2020 (Association Aéronautique et Astronautique de France & European Space Agency), Estoril, Portugal, Feb 8-12, 2021.

During the research period, the author was awarded financial support from three different entities. Through a national pool to Portuguese Master and PhD students, the author won a sponsorship from the partnership Massachusetts Institute of Technology - Portugal (MIT Portugal) to attend MIT Space Week 2020 at the MIT campus in Boston, USA. From the European Fusion Education Network (Fusenet), the author received financial support to participate in the IWSSPP in Kitten, Bulgaria, and through the Portuguese research group, Transport Phenomena Research Center (CEFT), the author could attend the other conferences.

Currently, the author expects to publish the research results in at least three scientific articles on peer-reviewed journals dedicated to the field of plasma physics and electric propulsion.

1.4 STRUCTURE OF THE PRESENT THESIS

The research was developed essentially between October 2019 and June 2020 and has concluded with the writing of this dissertation, which is divided into seven chapters, including the present one, and one appendix.

The second chapter explains how a space propulsion system works. It starts from a brief physical explanation and a mathematical description for the rocket motion, then it is presented a definition of the main variables and figures of merit. Posteriorly, it is introduced a description of several types of spacecraft missions and orbital maneuvering, where the electric thrusters are frequently used. Finally, are reviewed and classified the several electric propulsion systems, as well as a comparison between all of them.

The third chapter presents the physical model used in these simulations and optimizations of the EHD thruster. It starts to present all the differential equations used in the computation and then it presents how the thruster was designed, that is, the geometry chosen, the boundary conditions and the two-dimensional model grid. Lastly it shows how the thruster parameters are developed and computed throughout the model.

The dissertation results are presented in the three following chapters, from chapter four to six. In the fourth chapter, a theoretical discussion is presented. Since there is no scientific consensus when writing the external density force, this chapter exploits all the density force terms, through a computational point of view and concludes with which force density term should be used.

The fifth chapter shows all the argon propellant thrusters studied at a pressure of 10Torr. It firstly presents the several optimization studies on the cylindrical single stage thruster, such as the influence of the discharge current, the geometry of the ground cathode and the influence of the secondary electron emission coefficient. Then it presents the first and new conceptual model of a plasma-sliding thruster, in which we used a dielectric sheath beneath the cathode to improve the main thruster's parameters, by taking advantage of the sliding effect of the charged particles in contact with dielectric surfaces. Finally, it is presented several forms of argon dual stage EHD thruster and their respective thruster parameters.

The sixth chapter compares xenon single stage EHD thruster and the argon single stage EHD thruster in terms of the respective cathode's intrinsic geometry and the secondary electron emission coefficient. Then, it presents a brief study of the cathode's cone angle and a potentially new geometry concept in a dual stage xenon thruster.

The seventh chapter sets the conclusions reached from this work and presents the future work paths for the development of electric propulsion technologies.

The appendix shows the physical theories underling the electrohydrodynamic processes. Such as the electron Boltzmann equation and transport coefficients, theory of the electrohydrodynamic density force and the theory behind the calculation of the output thrust in the developed model.

Chapter 2.

Space propulsion

To understand how a simple space propulsion system works, it is necessary to know its physical behavior. For a rocket thruster, the physics behind it, were first described by Tsiolkovsky in 1903, who took Newton law of motion for an accelerated rocket vehicle and changed the constant mass term into continuously decreasing the mass term due to the exhaust propellant (Turner (2009)).

2.1 FUNDAMENTALS OF ROCKET PROPULSION

This section will be a simple presentation of the rocket propulsion background necessary to understand the motion of a simple rocket, in a conservation of linear momentum approach.

Take a rocket, with an instantaneous mass of m, that is moving and at an instant of time $t = t$, its instantaneous velocity measured relatively to the an Earth referential system is $\mathbf{v}$. We considered only the rocket and fuel system. In this conditions, the linear momentum of the system is

$$\mathbf{P}_i = m\mathbf{v} \tag{2.1}$$

As the rocket burns its fuel at a constant rate, the velocity of the expelled gases is constant and after an interval of time dt, an amount of mass of gas dm_g was expelled from the rocket with an exhaust velocity of $\mathbf{v}_g$. However, this velocity is measured on the rocket referential and must be measured regarding an Earth referential system by converting it, that is $\mathbf{v}_g = \mathbf{v}_{ex} + \mathbf{v}$, where $\mathbf{v}_{ex}$ is the propellant gas exhaust velocity.

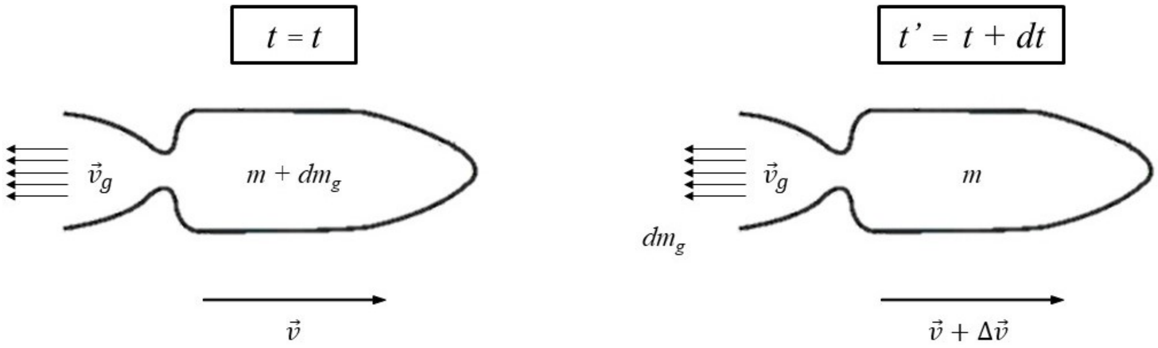

Figure 2.1: Schematic of simple rocket propulsion at $t = t$ and $t'= t + dt$ (adapted from El-Sayed (2016)).

Then the rocket's mass decreased by the same amount of mass gas that was expelled whereas its velocity increased by an infinitesimal amount of $d\mathbf{v}$. So the linear momentum at an instant of time $t' = t + dt$ is the sum of the rocket's linear momentum and the momentum of the exhaust gas, that is $\mathbf{P}_f = \mathbf{P}_{rocket} + \mathbf{P}_{gas}$. This can be written as

$$\mathbf{P}_f = (m - dm_g)(\mathbf{v} + d\mathbf{v}) + dm_g\mathbf{v}_g \tag{2.2}$$

$$\mathbf{P}_f = (m - dm_g)(\mathbf{v} + d\mathbf{v}) + dm_g(\mathbf{v}_{ex} + \mathbf{v}) \tag{2.3}$$

The total variation of linear momentum $d\mathbf{P}$ is simple $\mathbf{P}_f - \mathbf{P}_i$, and then by expanding all the physical quantities we get the following expression:

$$d\mathbf{P} = m\mathbf{v} + md\mathbf{v} - dm_g\mathbf{v} - dm_g d\mathbf{v} + dm_g\mathbf{v}_{ex} + dm\mathbf{v} - m\mathbf{v} \tag{2.4}$$

since the term $dm_g d\mathbf{v}$ is a second order term and is much smaller then the other terms, we can simple neglect it. Rearranging the expression we get

$$d\mathbf{P} = md\mathbf{v} + dm_g\mathbf{v}_{ex} \tag{2.5}$$

In the meantime we can substitute $dm_g = -dm$ since the mass of gas expelled corresponds to a reduction into the the rocket mass. Yet we can also divide by dt to obtain the rate of change of linear momentum

$$\frac{d\mathbf{P}}{dt} = m\frac{d\mathbf{v}}{dt} - \frac{dm}{dt}\mathbf{v}_{ex} \tag{2.6}$$

Since a variation of a linear momentum results in a force, we get

$$\mathbf{F}_{ext} = m\frac{d\mathbf{v}}{dt} - \frac{dm}{dt}\mathbf{v}_{ex} \tag{2.7}$$

In the absence of external forces in our system we simply get

$$m\frac{d\mathbf{v}}{dt} = \frac{dm}{dt}\mathbf{v}_{ex} \tag{2.8}$$

Considering that v_{ex} is time independent (is a quantity dependent on the construction of the propellant), rearranging the equation and integrating it, we finally get

$$\mathbf{v}_f - \mathbf{v}_i = \Delta\mathbf{v} = -\mathbf{v}_{ex}\ln\left(\frac{m_0}{m_f}\right) \tag{2.9}$$

where m_0 is the initial mass of the system who corresponds to the sum of propellant mass consumed, m_p, and the final burnout mass, m_f. Since all velocities terms point in the same direction, the above equation can also be written as

$$\Delta v = v_{ex}\ln\left(\frac{m_0}{m_f}\right) = v_{ex}\ln\left(1 + \frac{m_p}{m_f}\right) \tag{2.10}$$

which corresponds to the *Tsiolkovsky's rocket equation*.

Equation (2.10) shows that there are two methods to achieve a larger Δv: the first one is to burn a considerable amount of propellant $(m_p \approx m_0)$ the other is the use of a high exhaust speed thruster v_{ex}. Meanwhile we can observe these two methodologies in figure (2.2), where the left side of the dot lines, corresponds to all chemical propulsion systems and the right side to the electric propulsion (EP) systems. For a given increment velocity Δv, the propellant mass ratio m_p/m_0 depends on the exhaust velocity speed according to the expression:

$$m_p = m_0\left[1 - e^{-\Delta v/v_{ex}}\right] \tag{2.11}$$

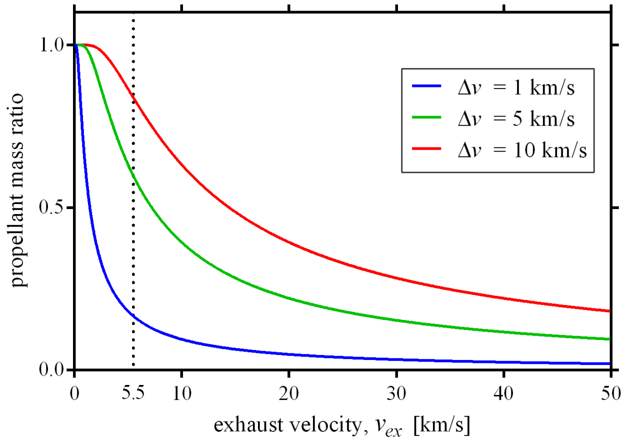

Figure 2.2: Variation of the propellant mass ratio m_p/m_0 as function of the exhaust velocity, v_{ex} for each increment velocity, Δv, both in units of $\mathrm{km\,s^{-1}}$ (adapted from Mazouffre (2016)).

2.2 ROCKET FIGURES OF MERIT

In the field of rocket propulsion, there are a lot of parameters that describe their physical properties. Nevertheless, in this section the only parameters that are being described are the ones that are directly related to electric propulsion since the chemical propulsion parameters are not needed.

In a simple formulation, Charles (2009) defined **thrust**, T, as the force supplied by the engine to the thruster. Since the thruster suffers a change in its total mass due to the difference in the propellant mass, this force is given by the time rate of change of momentum:

$$T = \frac{d(m_p v_{ex})}{dt} = v_{ex}\frac{d(m_p)}{dt} = v_{ex}\dot{m}_p \tag{2.12}$$

where $\dot{m}_p$ is the **propellant flow rate** expressed in $\mathrm{kg\ s^{-1}}$, which represents how fast is the propellant burning, during its mission.

Integrating this last equation over a complete space mission, we found the quantity called **total impulse**, I.

$$I = \int_{t_0}^{t_f} T dt = m_p v_{ex} \tag{2.13}$$

where I is expressed in $\mathrm{N \cdot s}$. This quantity measures the change in momentum that a thruster transmits to the spacecraft.

Another important parameter is the **mass ratio**, defined as the ratio between the total mass and the final mass of the thruster after all the fuel has been expelled. This ratio can be found in equation (2.10) and its the ratio m_0/m_f.

One way to measure the thruster efficiency is the ratio between the thrust and the rate of propellant weight consumption at sea-level. This ratio is called the **specific impulse**, I_{sp}.

$$I_{sp} = \frac{T}{\dot{m}_p g} = \frac{v_{ex}}{g} \tag{2.14}$$

where g is the gravitational acceleration and I_{sp} has SI units of s. The direct relation between this two quantities, (v_{ex}) and g, is very important since EP systems can achieve high exhaust velocities $(v_{ex} \geq 10\ \mathrm{ms}^{-1})$, features that are a key element for spacecraft missions, such as orbital maneuvers or interplanetary travels (Conde et al. (2017)).

Meanwhile, another efficiency quantity is the **thrust-to-wheight ratio** (TWR). This physical term defines the relation between the output thrust produced by the thruster, and its original weight, mathematically it's described as:

$$TWR = \frac{T}{mg} \tag{2.15}$$

where m is the thruster mass at a given time and TWR is an adimentional quantity.

Yet an important efficiency quantity in the field of EP systems is the **thrust-to-power ratio** (TPR or T/P ratio). This efficiency measures the amount of output thrust produced by one spacecraft considering the amount of power spent in the electric propulsion system,

$$\text{T/P ratio} = \frac{T}{P_e} \tag{2.16}$$

where P_e is the electric power spent by the thruster and T/P ratio is defined having units of $\mathrm{N\ W}^{-1}$. This type of thruster efficiency is important to characterize the geometry and the optimization of the developed electric thrusters.

2.3 SPACECRAFT MISSIONS AND ORBITAL MANOEUVRING

As it was said earlier, an high exhaust velocity reduces the propellant mass ratio, allowing us to reduce the total cost of the space mission. This property can be achieved only by EP systems since the conventional chemical thrusters, whether liquid or solid, are constrained by the ratio of energy per unit of mass stored in the propellant, thus limiting their exhaust velocity, which cannot exceed $v_{ex} \leq 5.5\ [\mathrm{km\ s^{-1}}]$ (Mazouffre (2016)).

Despite of having better performance, the implementation of EP has been a more conservative and gradual. According to Kluever (2015), it begin on a small-stage, as orbit manoeuvrers to keep satellites in the geostationary-equatorial orbit (GEO). For the large-Δv thrusters, they were forbidden to perform transitions from low-earth orbit (LEO) to GEO due to the high onboard power requirements and long transit times. Fact that recently are being change since the new commercial GEO satellites show an high power-to-mass ratios that may favour the EP systems for these orbital transfers.

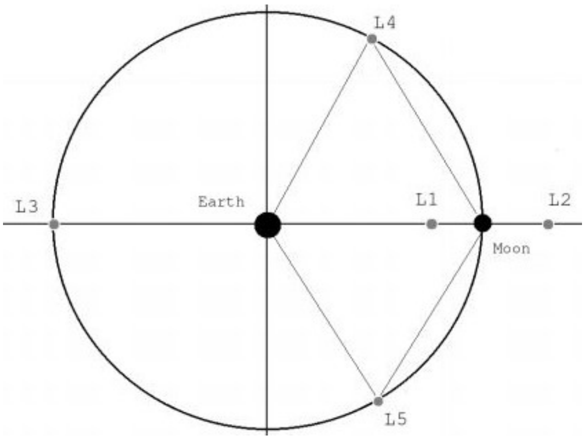

Figure 2.3: Representation of *Lagrange points* (L_1 to L_2) in an Earth-Moon system (adapted from Henninger (2015)).

As an example, on Earth-Moon transitions, there are key elements for the efficiency and cost of the missions, one was previously told and the other is the *Lagrange points*. These points mark the five positions in an orbital configuration where a body of comparatively negligible mass and affected only by the force of gravity, can theoretically be part of a stationary model together with two massive objects since at these points, the confined gravitational force of the two body masses provides precisely the centrifugal force required for the body to orbit with these two objects. They came from a stationary solution of a three body problems and they are labelled from L_1 to L_5. The L_1 and L_2 are points of interest in the area of orbital transfer and space missions because they are between Earth and Moon (Henninger (2015)).

A brief discussion about orbit transitions will be presented in order to consolidate the use of electric thruster. In the study of orbital manoeuvrers, there is one case study that is the basics for all space missions and that is the **Hohmann transfer**. This orbital change was first describe by a German engineer when he demonstrate the existence of a minimal energy level (energy-efficiency) in orbital exchange (Bettinger and Black (2014)).

In his work, Curtis (2019) exploits this topic in chapter 6, and it will be based on his sayings that the next presentation will be based. The *Hohmann* transfer consists in an elliptical orbital transfer which is tangent to two coplanar circles on its apse line. In turn, the elliptical periapsis and apoapsis are the radii of the inner and outer circles, respectively.

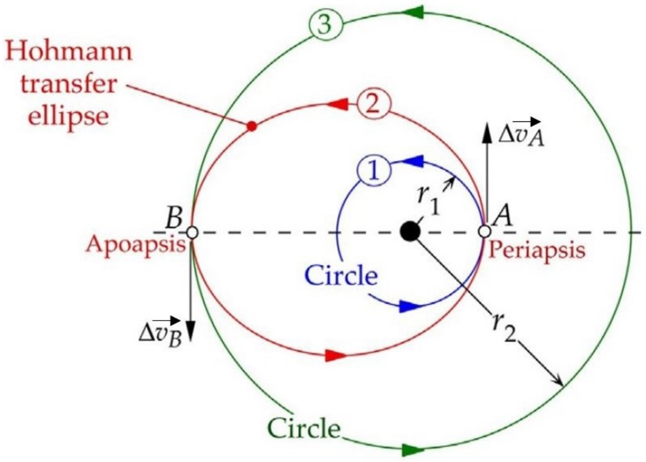

Figure 2.4: Hohmann transfer ellipse (Curtis (2019)).

Consider a spacecraft or a small satellite in a circular orbit with radius r_1, as illustrated in figure (2.4). To travel to an higher energy orbit, the vehicle will require a boost or an increment velocity, $\Delta\vec{v}_A$, to get onto a higher energy elliptical trajectory. After the transition from A to B, it will be needed an extra increment velocity $\Delta\vec{v}_B$ to place the vehicle in the outer circular energy orbit. Without this additionally increment velocity, the spacecraft would remain on the *Hohmann* transfer ellipse. Overall the total speed change is given by $|\Delta\vec{v}_A| + |\Delta\vec{v}_B|$ and the total energy change is proportional to $(|\Delta\vec{v}_A| + |\Delta\vec{v}_B|)^2$.

For the inverse transfer, form B to A, the same incremental speed, Δv, is required yet since the vehicle is moving to lower energy orbits, the applied thrust must be in the opposite direction to the vehicle's, so it can act as a motion brake.

In summary, the different increment speeds for each distinct space mission can be observed

Table 2.1: Typical increment velocities, Δv, for various orbital transfers and space missions (adapted from Mazouffre (2016)).

Orbit Transfer	Δv $[\mathrm{km\,s^{-1}}]$
LEO-GEO	4.3
LEO- Moon	5.9
LEO-L_1	3.7
LEO-L_2	3.4
LEO-Mars	4.3
Interplanetary journeys	Δv $[\mathrm{km\,s^{-1}}]$
nearby planets	5-8
far-off planets	10-15

in table (2.1). From this table, it is possible to deduce that the choice of electric propulsion over conventional chemical propulsion is a more efficient one.

2.4 ELECTRIC PROPULSION

To achieve exhaust velocities above 6 $[\mathrm{km\,s^{-1}}]$, desirable for interplanetary missions, is evident that the processes dependent on the simple heating of the propellant stream in chemical reactions or solid element heat transfer, are not enough. So to employ a propulsion system that can obtain these higher exhaust velocities, body forces must be directly applied to the propellant stream. There are two different processes that could lead to this phenomena, the high enthalpy heating of an insulated gas stream and the direct acceleration by applied forces. These processes are easily accomplished by electrical means which led to the main definition of electric propulsion (Jahn (2006)):

> *The acceleration of propellant gases for propulsion by electrical heating and/or electric and magnetic body forces.*

By achieving greater exhaust velocities, EP systems suffer a reduction in the amount of propellant gas required for a given space mission, which leads to significantly decrease the launch mass of a spacecraft or satellite. In monetary upkeep, this reduction also leads to lower costs from the use of smaller launch vehicles to deliver a desired mass into a given orbit or to a deep-space target (Goebel and Katz (2008)).

In terms of design, there are a large number of different types of EP systems where some are in a conceptual stage, others already achieved a very high technological maturity level, and only a few are already in use in space. Regardless, EP systems can be characterized into three main types: electrothermal , electrostatic and electromagnetic (Holste et al. (2020)).

Electrothermal Propulsion

The principle behind electrothermal thrusters is the conversion of electric or electromagnetic energy into a thermal energy on the propellant gas. Then, this energy is transformed into thrust by expanding the heated propellant through a *de Laval* nozzle structure (converging-diverging). There are several ways to produce this input energy, they could be in the form of a resistivity heating, by direct electric arc heating of the propellant or by electromagnetic radiation (Power (1992)).

In a resistojet thruster, a propellant passes through a heat exchanger in which the temperature of the medium increases rapidly due to heat delivered by an element based on Ohmic heating, increasing also the exhaust velocity (Kindracki et al. (2019)).

An arcjet thruster consists of an anode nozzle and a coaxial cathode mounted upstream of the anode. Both electrodes are, usually built by tungsten alloys and are isolated from each other by a high temperature insulator, typically boron nitride or aluminum oxide. Tungsten is always chosen to serve as electrodes because of its high melting temperatures and low work function due to the doping additives. To control the arc regime and the constrictor wall cooling, the propellant gas chosen is usually a low molecular weight, such as hydrogen or chemical compounds of it. The gas stream is injected tangentially to the arc chamber so it produces a cold gas swirl (Wollenhaupt et al. (2018)).

However the endurance of the heater and wall materials, when submitted to high temperatures, and the cathode erosion from the constant ion bombardment repose a major efficiency and life limiting problems. Consequently, new type of electrothermal thrusters are being developed based on electromagnetic radiation such as the Microwave Electrothermal Thruster. This thruster employs free floating plasma at atmospheric pressure and since it doesn't have any resistant heater or arc system, it eliminates their respective inherent conceptual problems (Yildiz and Celik (2017)). This type of thruster can mitigate space debris, by taking advantage of residual helium gas that gets trapped in the chemical propellant feed system and will be unused at end of life. This is achieved by accelerating propellant gas by heat. The additional propellant resources extends satellite lifetimes and transfer geostationary orbit space assets to ultra safe disposal orbits (Walker et al. (2012)).

Electrostatic Propulsion

The most common electrostatic devices are the gridded ion thrusters (GIT) since they are based on a simple physical principle, the electrostatic acceleration of charged particles. The propellant is injected in the chamber where a DC discharge occurs. The gas is accelerated by acceleration grids and it is neutralized by secondary electron emission from a hollow cathode (Rafalskyi and Aanesland (2019)).

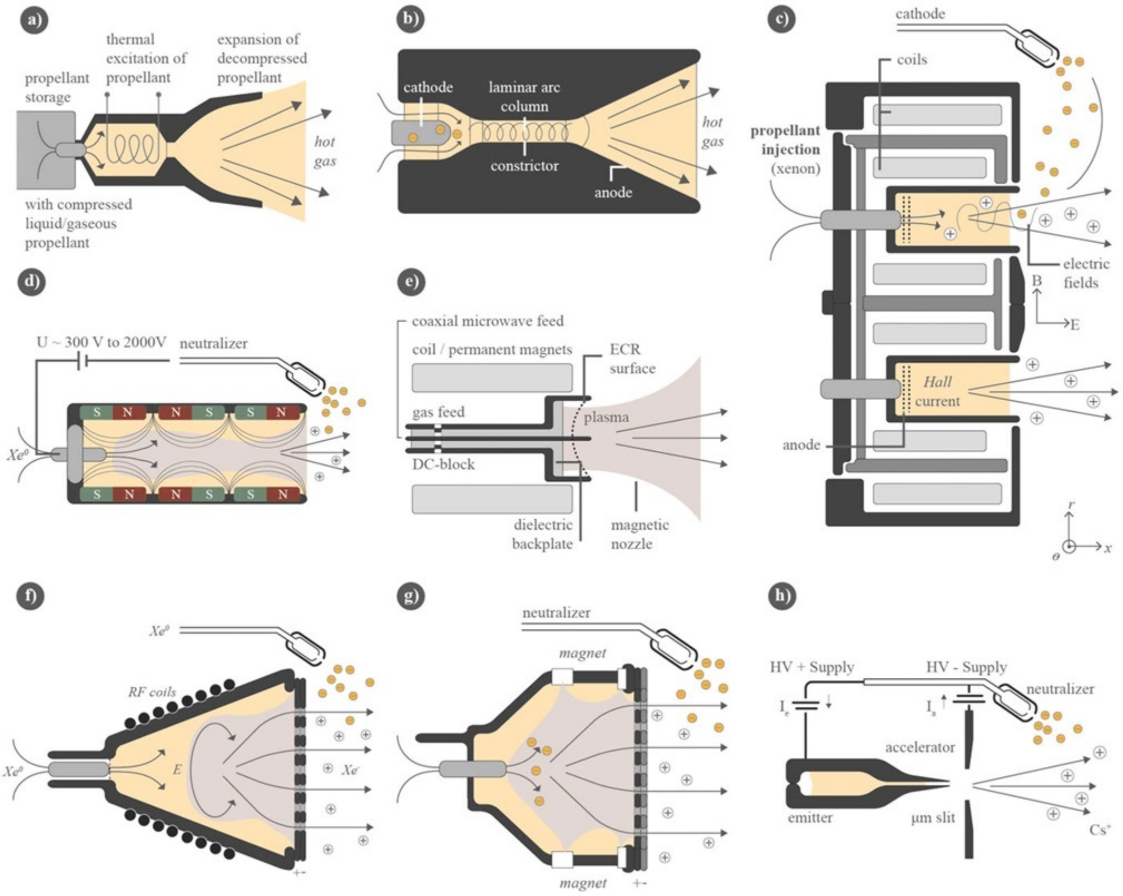

Figure 2.5: Schematic drawings of the main electric propulsion systems: (a) resistojet, (b) arcjet, (c) Hall thruster, (d) high efficiency multistage plasma thruster, (e) electron cyclotron resonance thruster, (f) radio frequency ion thruster, (g) electron bombardment thruster, and (h) field-emission electric propulsion (taken from Holste et al. (2020)).

The electrohydrodynamic thrusters (EHD) are devices that used two or more electrodes that ionize the ambient fluid, the ionized particles gain momentum under an electric field, which accelerate them. Then these charged particles undergo momentum-transfer collisions with neutral molecules in a phenomenon termed an ionic wind (Masuyama and Barrett (2013)). Meanwhile this process can be applied into another areas such as EHD Fluid Pumps and Flow and Heat Transfer Enhancement (Fylladitakis et al. (2014)).

Hall effect thruster (HET) is a propulsion system based on a plasma discharge with magnetized electrons. By using a magnetic barrier and a low pressure dc discharge between the high voltage anode and ground cathode, a crossed electric and magnetic field discharge is created (Mazouffre and Grimaud (2018)). To the accelerated ionized gas by the electric field, a $\mathbf{E} \times \mathbf{B}$ drift is added, where the magnetic field is design so the electrons be trapped in their field lines, while ions were not Boeuf (2017). A thermionic cathode is placed outside the discharge chamber, where it will emit a large number of secondary electrons, thus neutralizing the propellant gas.

To develop a high efficiency multistage plasma thruster (HEMPT), it is necessary that the plasma inside the discharge chamber be confined by several permanent periodic magnets of opposite magnetization directions. Normally, the geometry of this thruster consists on three to six times larger channel length in comparison to the channel radius, depending the amount of magnets used. To stabilize the plasma flow, the magnets are covered with a dielectric layer, usually the material chosen is one with a high sputtering threshold energy, in order to ensure a long lifetime (Kahnfeld et al. (2019)).

Electromagnetic Propulsion

The attraction of ablative pulsed plasma thrusters (PPT) is their ability to provide small, controlled impulse bits in a self-contained package with indefinitely storable solid propellant and a simple spacecraft interface. With these attributes, PPTs have been used for altitude control, constellation maintenance, and precision station keeping Hoskins et al. (2013).

The magnetoplasmadynamic thruster (MPDT) consists of a central cathode and a concentric anode, where the propellant gas is ionized and accelerated by an arc discharge between the electrodes. The interaction between the magnetic field and the electric current produces two distinct forces: axial force and azymuthal force, this is due to the fact that the radial current is the predominant term in comparison with the axial and azimuthal components. The axial force is originated by the interaction of this radial current and the induced azimuthal magnetic field, created by the discharge current, whereas, the azymuthal force comes from interaction of the radial current with the axial applied magnetic field, produced by the electromagnetic coils around the cathode (Zhang et al. (2019)).

By absorption of microwave power through electron cyclotron resonance, the electron cyclotron resonance thruster (ECRT) was created. When the electric field frequency ω_{rf} coincides with the cyclotron frequency of electrons ω_c in the presence of an applied magnetic field, a resonant absorption occurs. At this situation, the electrons perceive the electric field as stationary and will continuously heat. If a magnetic diverging field is introduced, the plasma will suffer expansion in the magnetic nozzle, resulting into an ambipolar electric field which accelerates the propellant gas (Cannat et al. (2015)).

Comparison between EP systems

Since there are many parameters to consider when designing a rocket, a simple quantification and evaluation becomes a difficult task. As it was said in the previous sections, every single mission has its own characteristics, being the main reason for the proliferation of different plasma thrusters. To summarize some of plasma thrusters, table (2.2) presents several key parameters such as thrust, specif impulse or thrust-to-power ratio and even operation flight time. In the end, it is also shown the benefices and disadvantages of each plasma propulsion system.

2.5 ADVANCED PROPULSION TECHNOLOGIES

Solar sail propulsion

One type of propulsion utilizes a constant resource in space, radiation from the Sun. By reflecting solar photons from a large sail made of a lightweight and highly reflective material, solar sail propels vehicles throughout space. More specifically, this propulsion uses the radiation pressure exerted by the momentum transfer of reflected light. However for this effect to be useful, it is required a large number of photons to generate a considerable amount of momentum, therefore, it is necessary a large sail (Johnson et al. (2011)).

Tether propulsion

By employing a thin long wire or tether in a orbiting satellite or vehicle, the movement of the wire will produce an electric current, which will interact with the planet magnetic field. The force exerted on the wire by the planet magnetic field can be applied to raise or lower the satellite, according to the current direction (Salgado et al. (2018)).

Fusion propulsion

A system based on nuclear fusion propulsion has the potential to allow for fast interplanetary missions and transportation. For a engine of this sort to be operated, a magnetic nozzle should be implemented in order to contain and direct the nuclear by-products originated from the pulsed fusion propulsion. This nozzle has to be robust to withstand extremely harsh conditions (Miernik et al. (2011)).

Laser propulsion

According to Jamil et al. (2013), laser propulsion is a form of beam powered propulsion in which a pulsed laser ablates a target material thus producing and output thrust. The applications can be transposed to a groundbreaking system, which can generate enough thrust for the re-orbiting of very low altitude satellites. The laser beam source can be one of two systems, one ground station or a chosen satellite. The laser hits the target satellite’s surface, vaporizes and produces ablation of the material, producing a net thrust (Felicetti and Santoni (2013)).

Solar electric propulsion

According to Chang Díaz et al. (2019), solar electric propulsion uses solar power to supply the electric circuit that ionizes and accelerate heavy propellants on an electric propulsion system. It is widely treated as the choice for cargo transportation into interplanetary journeys such as Mars.

Table 2.2: Characteristics of main electric propulsion thruster types (taken from Holste et al. (2020)).

	Resistojet	**Arcjet**	**GIE**	**HET/HEMPT**	**PPT**	**MPDT/ECRT**
Type	electrothermal	electrothermal	electrostatic	electrostatic	electromagnetic	electromagnetic
Achievable thrust [mN]	0.5-6000	50-6800	0.01-750	0.01-2000	0.05-10	0.001-2000
I_{sp} [s]	150-850	130-2200	1500-10000	600-3000	1400-2700	200-3200
T/P ratio [mN/kW]	450-700	150-600	20-250	150-300	50-200	150-500
Time of operation	Month	Month	Years	Month	Years	Weeks
Propellants	NH_3, hydrazine, H_2, Xe, and N_2	H_2, N_2, hydrazine and NH_3	Xe, Kr, Ar Bi, I_2, and H_2O	Xe, Kr, Ar and I_2	PTFE	Ar, Xe, H_2 and Li
Benefit	Low level of complexity	High thrust	High Isp and high efficiency	High T/P ratio	Simple device and solid propellant	High I_{sp} and high thrust density
Drawback	Very low I_{sp}	Low efficiency	Low thrust density and complex PPU	High beam divergence and channel erosion	Low efficiency	Low lifetime and high power requirement

Chapter 3.

Physical model of electrohydrodynamic thruster

In order to developed the study of electrodynamics thruster, we proposed a numerical model which comprises the coupling of several different modules. This model is very complex due to the underlying physics involved which combines fluid mechanics, plasma physics and chemistry. Normally, to develop and optimize this type of thruster, the programmer must predict the flow pattern inside its geometry, from the anode to the cathode, and the electric field profile. Yet it is also important to redesign the discharge regime, which could lead to unwanted results, or even to errors during the simulation.

To combine all of these physical environments, it was used a finite-element method (FEM), sub-dividing the computational domain into a mesh of points where the differential equations were solved locally, taking into account the appropriate boundary conditions. The software utilized was the COMSOL *Multiphysics*® which provides the coupling of all of this modules and solves all of the differential equations with a time-dependent solver and it can lead to a steady-state solutions for each case study.

3.1 MODELLING EHD THRUSTER

Electrohydrodynamic physics intertwines fluid dynamics, physics of ionized gases, self-consistent accelerating electric field, described by *Poisson*s equation, and migration of charged particles in an electric field in the drift-diffusion approximation. To module all of these processes, Granados (2018), divides its model into three main modules that are coupled: kinetic, plasma and laminar flow module.

The kinetic module uses all species reactions, either gas chemistry or electron impact reactions. From the electron collision reactions it computes electron transport coefficients and electron collision rate coefficients through a Maxwellian electron energy distribution function (Maxwellian EEDF). Along with the chemical gas reactions it then compute the source terms R_e and R_ε. The plasma model is described by their conventional transport equation4jj, the *Boltzmann* equation. The fist momentum equation corresponds to the transport of electrons and ion, the second is described to the momentum transfer in the drift-diffusion approximation, and the electron energy density, the third momentum equation. In this module, the electric field, and the gas discharge equations are also included, depicting the migration of charged particles in an electric field. The laminar flow module takes into account the fluid behaviour of a low ionized gas and uses the *Navier-Stokes* equation.

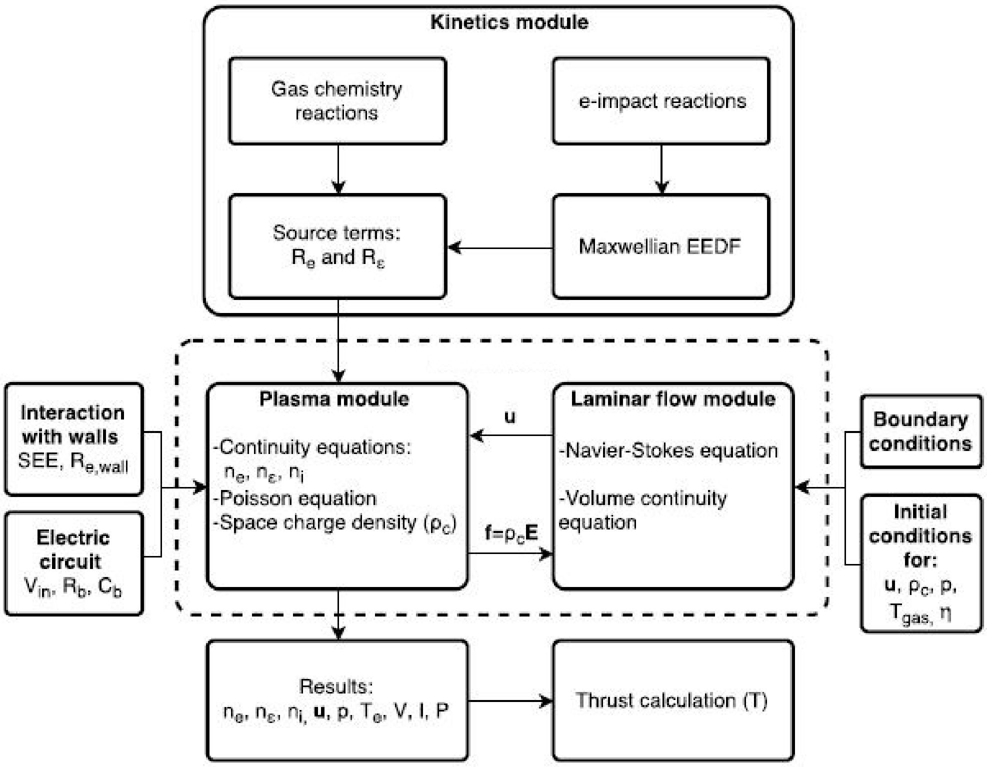

Figure 3.1: Schematic of a pseudo-flow chart who comprises and connect all modules and entry parameters used in the EHD thruster module (adapted from Granados (2018)).

As it depicted in figure (3.1), SEE is the secondary electron coefficient and R$_{e,wall}$ is the contribution to the electron source term due to electron interactions with the walls. V_{in}, R_b, C_b are the input voltage, the ballast resistor and the blocking capacitor, respectively. n_e, n_ε, n_i and ρ_c are the electron density, electron energy density , ion density and space charge density. **f** and **u** are the force density and main fluid velocity. T_{gas} is the gas temperature and T_e is the electron temperature, η is the gas dynamic viscosity. Finally, the results variables V, I, P, T are the voltage, current, power and thrust, respectively.

Electrostatic model for electric field and potential distribution

In this model, the electric potential distribution, V, under the presence of a space-charge distribution $\rho_c(\mathbf{r})$, is computed by solving the Poisson equation

$$\nabla^2 V = -\frac{\rho_c}{\epsilon} \tag{3.1}$$

where ϵ is the plasma permittivity $(\epsilon = \epsilon_0 \epsilon_r)$. Consistently in the same time step, the space-charge density is computed taking into account the plasma chemistry and the species charged densities by

$$\rho_c = q_e \left(\sum_{j=1}^{N} Z_j n_j - n_e \right) \tag{3.2}$$

where Z_j is the ion charge number, $n_j(\mathbf{r})$ the ion density for species j and $n_e(\mathbf{r})$ the electron number density. Finally the calculation of the electric field, **E** is done under the relation between this physical quantity and the electric potential distribution

$$\mathbf{E} = -\nabla V \tag{3.3}$$

Plasma model for species spatial distributions

To simulate the plasma behavior under EHD body forces, we must consider the migration of all the particles species involved, such as the electrons, ions and neutrals, since they are fundamental to the calculation of the space charge density.

The set of equations that are responsible for the evolution of each specie are the continuity equation for the electron density, n_e; the continuity equation for the electron energy density n_ε

and the continuity equation for the gas particles, which are calculated, using the mass fraction of the kth species, ω_k, and following the COMSOL Multiphysics manual (*Plasma Module Users Guide* (n.d.)),

$$\frac{\partial}{\partial t}n_e + (\mathbf{u}\cdot\nabla)n_e = -\nabla\cdot\mathbf{\Gamma}_e + R_e \tag{3.4}$$

$$\frac{\partial}{\partial t}n_\varepsilon + (\mathbf{u}\cdot\nabla)n_\varepsilon = -\nabla\cdot\mathbf{\Gamma}_\varepsilon - \mathbf{E}\cdot\mathbf{\Gamma}_\varepsilon + R_\varepsilon \tag{3.5}$$

$$\rho_f\frac{\partial}{\partial t}\omega_k + \rho_f(\mathbf{u}\cdot\nabla)\omega_k = \nabla\cdot\mathbf{\Gamma}_k + R_k \tag{3.6}$$

where $\mathbf{u}$ is the main fluid velocity; ρ_f is the main gas mass density; $\mathbf{\Gamma}_e$ is the electron flux, $\mathbf{\Gamma}_\varepsilon$ is the electron energy flux, $\mathbf{\Gamma}_k$ is the diffusive flux vector; finally R_e,R_ε and R_k are the electron density, electron energy density and the kth specie density sources respectively. The second term in left side of these set equations appear from the fact that COMSOL presents a generalized model for various plasma simulations. So when modelling fusion plasmas, that drift-diffusion approximation is not suited, since they required that the plasma must also be collisional which means that the mean free path between electrons and the breakgound gas must be inferior to the characteristics of the system. More information on this subject can be found in *Plasma Module: User's Guide*. Under the drift-diffusion approximation, the flux vector of any species can be approximated to the product of the species' number density with the species' drift velocity, such as $\mathbf{\Gamma} = n\mathbf{v}$, which leads to

$$\mathbf{\Gamma}_e = (\widetilde{\boldsymbol{\mu}}_e\cdot\mathbf{E})n_e - \nabla(\mathbf{D}_e n_e) \tag{3.7}$$

$$\mathbf{\Gamma}_\varepsilon = (\widetilde{\boldsymbol{\mu}}_\varepsilon \cdot \mathbf{E})n_\varepsilon - \nabla(\mathbf{D}_\varepsilon n_\varepsilon) \tag{3.8}$$

where the $\widetilde{\boldsymbol{\mu}}_\varepsilon$ represents the electron mobility tensor, $\widetilde{\boldsymbol{\mu}}_e$ is the electron energy mobility tensor; $\mathbf{D}_e$ and $\mathbf{D}_\varepsilon$ are the tensors for the electron diffusivity and electron energy diffusivity. These two physical quantities are related, $\mathbf{D}_e = \boldsymbol{\mu}_e T_e$ and $\mathbf{D}_\varepsilon = \boldsymbol{\mu}_\varepsilon T_e$, where T_e is the electron temperature, if they are derived from the *Maxwellian* electron energy distribution function (EEDF), using the Einstein's relation.

Meanwhile, the diffusive flux vector of k-species is computing from the expression

$$\mathbf{\Gamma}_k = \rho_k \omega_k \mathbf{v}_k \tag{3.9}$$

where ρ_k is the mass density of $k-$species and $\mathbf{v}_k$ is the diffusive velocity vector which depends on the k-species diffusivity and mobility tensors.

To determine the R_e,R_ε and R_k source terms, it is necessary to know the chemical reactions that are generated inside the discharge reactor to determine their rate coefficients k_j. Since we assumed that each gas owns several heavy species, the rate coefficients of their collision processes, such as inelastic collisions (excitation and ionization) or elastic collisions are needed. To get the rate coefficients from these processes, we can compute the collision processes for electron collisions using a set of the respective cross section data and the *Maxwellian* distribution function $f_M(\varepsilon)$, for electron energy, through

$$k_j = \left(\frac{2e}{m_e}\right)^{1/2} \int_0^\infty \varepsilon \sigma_j(\varepsilon) f_M(\varepsilon) d\varepsilon \tag{3.10}$$

where ε is the electron energy in (eV); and $\sigma_j(\varepsilon)$ represents the cross-section data for the considered reaction. In table (3.1), it is possible to observe how these coefficients were calculated. Note that for electron-impact collisions who have rate coefficients designed as $f(\sigma)$, their rate coefficients are computed from the available cross-section data. To reduce the computational time and increase efficiency in our simulation, the higher excited states of energy were assumed to decay instantly into the representative states of Ar^* and Xe^* as it was assumed by Almeida and Benilov (2013) in their work with dc glow discharges.

Table 3.1: Electron-impact and chemical reactions with rate coefficients for argon and xenon discharges.

Reaction	Rate coefficient	References
Argon		
$e^- + Ar \rightarrow e^- + Ar$	$f(\sigma)$	Morgan (2015)
$e^- + Ar \rightarrow e^- + Ar^*$	$f(\sigma)$	Morgan (2015)
$e^- + Ar \rightarrow 2e^- + Ar^+$	$f(\sigma)$	Morgan (2015)
$e^- + Ar^* \rightarrow 2e^- + Ar^+$	$f(\sigma)$	Morgan (2015)
$e^- + Ar_2^+ \rightarrow Ar^* + Ar^+$	$5.06 \times 10^{-15} (T_e)^{-0.67}$	O'Malley et al. (1972)
$Ar^* + Ar^* \rightarrow e^- Ar + Ar^+$	6.2×10^{-16}	Bogaerts and Gijbels (1995)
$Ar^* + Ar \rightarrow e^- Ar + Ar$	3.0×10^{-21}	Bogaerts and Gijbels (1995)
$Ar^+ + 2Ar \rightarrow Ar_2^+ + Ar$	2.25×10^{-43}	Fitzwilson and Chanin (1973)
Xenon		
$e^- + Xe \rightarrow e^- + Xe$	$f(\sigma)$	Biagi (2019)
$e^- + Xe \rightarrow e^- + Xe^*$	$f(\sigma)$	Biagi (2019)
$e^- + Xe^* \rightarrow e^- + Xe$	$f(\sigma)$	Biagi (2019)
$e^- + Xe \rightarrow 2e^- + Xe^+$	$f(\sigma)$	Biagi (2019)
$e^- + Xe^* \rightarrow 2e^- + Xe^+$	$f(\sigma)$	Biagi (2019)
$Xe^+ + Xe \rightarrow Xe + Xe^+$	3.6×10^{-10}	Johnson et al. (1989)
$Xe^* \rightarrow Xe$	3.96×10^{6}	Johnson et al. (1989)
$Xe^* + Xe^* \rightarrow e^- + Xe + Xe^+$	5.0×10^{-16}	Johnson et al. (1989)

Rate coefficients have units of [m^{3}s^{-1}] or [m^{6}s^{-1}] or [s^{-1}].

Rate coefficients characterized by $f(\sigma)$ are computed through the cross-section data.

Fluid model and coupling with electric field

To describe the main fluid motion of the EHD thruster, we must consider few assumptions. The first one is that the fluid is incompressible and the viscous flow will have, in a first approximation, a laminar behaviour, which can be described by a the *Navier-Stokes* fluid equation. Under an external force density term, this equation can be written in the form of

$$\rho_f \frac{\partial \mathbf{u}}{\partial t} + \rho_f (\mathbf{u} \cdot \nabla)\mathbf{u} = -\nabla p \mathbf{I} + \nabla \cdot \left[\eta \left(\nabla \mathbf{u} + (\nabla \mathbf{u})^T\right)\right] + \mathbf{f} \tag{3.11}$$

where ρ_f is the fluid density, $\mathbf{u}$ is the main fluid velocity, p is the absolute pressure and $\mathbf{I}$ is the identity of a symmetric rank two tensor; η is the dynamic viscosity, which are a specific property of the fluid, and finally **f** is the external force term. Table (3.2) shows the value of dynamic viscosity of each noble gas for different ambient temperatures.

Table 3.2: Dynamic viscosity coefficients, η, for the ideal gases at several temperatures (adapted from Smirnov (2008)).

	$\eta\ 10^{-5}\text{Pa}\cdot\text{s}$				
Temperature $[\circ\text{C}]$	He	Ne	Ar	Kr	Xe
25	1.98	3.17	2.23	2.53	2.31
100	2.31	3.71	2.73	3.12	2.88
200	2.73	4.34	3.28	3.80	3.59
300	3.12	4.94	3.78	4.42	4.23
400	3.50	5.50	4.23	4.99	4.83
500	3.86	6.02	4.66	5.53	5.38
600	4.21	6.51	5.05	6.03	5.87
700	4.56	6.98	5.45	6.52	6.37

The second approach is that the external force term can be written as the electrostatic force density, $\mathbf{f} = \rho_c\mathbf{E}$. A more extensive theoretical explanation is presented in the appendices with two different deductions. We also study this force experimentally, in order to find the correct force term that should be used when modelling an electrohydrodynamic system.

Furthermore, since we are assumed that all gases in our study are incompressible, the volume continuity equation is given as

$$\nabla \cdot \mathbf{u} = 0 \tag{3.12}$$

Modelling electric discharge

When modelling a plasma, usually space charge and electric effects intervene with atomic and molecular collisions, making the collisional cross sections, rate coefficients and swarm transport data do not to need to be very accurate. On the other hand, gas breakdown is the point where these inaccuracies are amplified and the conditions for the breakdown are at the same time the conditions for control the main plasma (Marić et al. (2014)).

Gas breakdown is studied for more then a century and for a DC discharge is manly described by the *Townsend*s discharge theory (Townsend (1910)). In this theory, the electric breakdown in a gas occurs by two phenomena, i) the availability of initiatory electrons and ii) compensation of diffusion loss of ions and electrons. The last is compensated by the mechanism of ionization that produce amplification to the electrons or ions (Mathew et al. (2019)). In its bulk, the breakdown of a gas is a threshold process, meaning that this disruption only sets in if the external electric field exceeds a characterizing value of specific set of conditions. This threshold is defined by the relation between the creation and removal of electrons if the electric field is maintained for a enough amount of time which as to be adequate of the production of a numerous generations of electrons (Raizer et al. (2011)).

In order to describe these processes, *Townsend* defined two coefficients. The α coefficient which is the ionization per unit length or how it is known as first Townsend's ionization coefficient, which is a function of the electric field strength, pressure and intrinsic properties of the gas. The γ_i coefficient is the secondary electron emission coefficient and represents the quantity of electrons that are emitted from the cathode per incident particle and also depend of the electric field magnitude an pressure, as it is observed in table (3.3). For a self-sustained discharge to occur, *Townsend* concluded that these two coefficients should satisfy the following expression:

$$\gamma_i \left(e^{\alpha d} - 1 \right) = 1 \tag{3.13}$$

where d is the distance between the two electrodes, anode and cathode. The breakdown voltage is computed from *Paschen*'s law and is a function of the product of the pressure, p, in Torr and the distance d in cm$(LoureiroandAmorim\ (2016))$:

$$V_B = \frac{Bpd}{ln\left(Apd\right) - ln\left[ln\left(1 + \frac{1}{\gamma_i}\right)\right]} \tag{3.14}$$

here A is saturation ionization in the gas in units of Torr^{-1} · cm^{-1} and B is a constant related with the excitation and ionization energies in units of V · Torr^{-1} · cm^{-1}. Both constants depend of the nature of the used gas (Torres et al. (2012)).

Equation (3.14) gives the necessary voltage that should apply in a gas to start a electric discharge between two electrodes and by introducing each gas coefficients. For instance in the data presented by Raizer et al. (2011), we can observe that breakdown voltage firstly decreases up to a minimum as the pd values are reduced and then it gradually increases again, see figure (3.2).

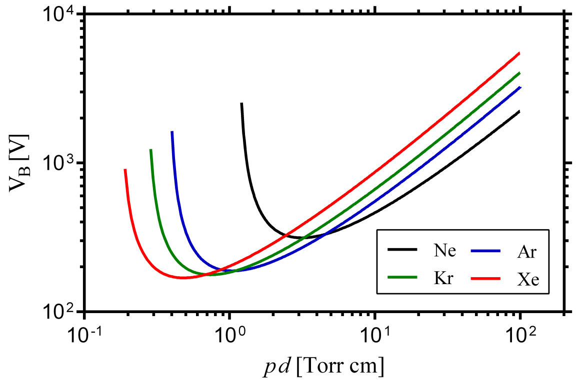

Figure 3.2: Breakdown voltages, or *Paschen*'s law, for inert gases over a with range of pd values (computed from Raizer et al. (2011)).

The minimum in the curve appears due for the different behaviour of the mean free path of the gas molecules. At low pressures, this property is large, so the number of collisions is low, so the number of ionizing collisions being also reduced. Yet for higher pressures, the mean free path is reduced and so the number of collisions in the gas is high, such as either momentum transfer, excitation collisions and other. Collisions like the ionization collisions turn small and only few electrons acquire enough energy over a mean free path to ionize. So to have enough ionization, breakdown voltage must increase (Loureiro and Amorim (2016)).

To produce the plasma out of the propellant gas, it is necessary to induce a discharge strong enough, so that the neutral particles near the anode can be ionized but not strong enough that could produce an arc between the two electrodes. The EHD thruster operates in a low regime, with discharge currents below 10^{-4}A, and the asymmetric electrodes will produce a non-uniform discharge non-equilibrium low-ionized plasma, which are the properties of a corona discharge. In this model, we consider that discharge current, I_d, and current flowing from the electrodes are the same and they are computed from the ion and electron current density vectors as

$$I_d = -\int (\mathbf{n} \cdot \mathbf{J}_i + \mathbf{n} \cdot \mathbf{J}_e)\, dS \tag{3.15}$$

where $\mathbf{n} \cdot \mathbf{J}_i$ and $\mathbf{n} \cdot \mathbf{J}_e$ corresponds to the internal product of the normal surface of the electrodes with respective current density vectors. The negative signal is a correction factor, making the normal components of these current density vectors pointing outwards of the surface walls.

To control the nonuniform discharges within the plasma, we used an low-pass RC coupling circuit in series with the main direct high voltage source and thruster. This type of circuit eliminates the high-frequency voltages that can emerge from the source and in the plasma load, and can prevent unwanted effects from the unstable region between the two electrodes.The ballast resistor, R_b, is introduced to control the current between the electrodes, since we are dealing with extremely high voltages, a low resistance value means that the current could increase exponentially, leading to an arc discharge.

Table 3.3: Values of the secondary electron emission coefficient, γ_i, for various reduced field, E/p in units V $\cdot$ cm^{-1} $\cdot$ Torr^{-1} , for each noble gas (taken from Auday et al. (1998)).

Ne		Ar		Kr		Xe	
E/p	γ_i	E/p	γ_i	E/p	γ_i	E/p	γ_i
301	4.30×10^{-2}	1772	7.83×10^{-2}	1702	6.01×10^{-2}	1560	1.14×10^{-2}
240	3.05×10^{-2}	757	1.56×10^{-2}	774	5.16×10^{-3}	775	1.45×10^{-3}
178	2.74×10^{-2}	288	8.35×10^{-3}	488	2.98×10^{-3}	603	9.52×10^{-4}
70	5.00×10^{-2}	222	7.74×10^{-3}	354	2.41×10^{-3}	499	6.87×10^{-4}
39	7.38×10^{-2}	182	7.57×10^{-3}	280	2.04×10^{-3}	382	3.94×10^{-4}
18	1.73×10^{-2}	146	7.64×10^{-3}	189	1.46×10^{-3}	316	2.57×10^{-4}
9	6.03×10^{-2}	77	1.24×10^{-2}	147	1.15×10^{-3}	227	1.44×10^{-4}
		51	2.28×10^{-2}	102	1.17×10^{-3}	129	1.63×10^{-4}
		32	5.92×10^{-2}	70	1.40×10^{-3}	89	3.01×10^{-4}
				46	2.16×10^{-3}	58	1.06×10^{-3}

On the other hand, an high value would reduce the potential difference in the plasma, reducing the electric field strength. By applying a DC voltage in the blocking capacitor, C_b, current will not flow from it, since it has an insulating medium between the two metal connectors. These property is very useful in controlling a plasma discharge since it will stabilize the current that flows within the plasma and will also avoid voltage peaks between the electrodes in the thruster.

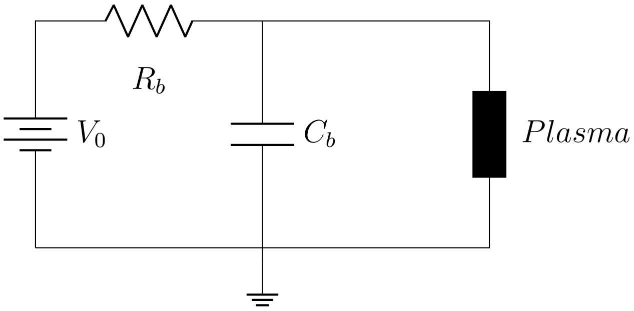

Figure 3.3: External low-pass RC coupling circuit that control the plasma discharge under the EHD thruster.

The relation of the DC voltage source, V_0, and the electric potential difference between the two electrodes, V_p, are computed by solving the *Kirchhoff*'s second law on the RC coupling circuit. This relation can be written as

$$V_p = V_0 - I_d R_b - R_b C_b \frac{dV_p}{dt} \tag{3.16}$$

To evaluate this model, we determined the energy spent in the creation of the plasma and the energy spent to sustain it by the calculated the power spent, P_{plasma} in the RC coupling circuit and the time interval during in which the propellant is active. The power spent is given by

$$P_{plasma} = V_p \times I_d \tag{3.17}$$

3.2 DESIGN THE EHD THRUSTER

We present a module based on a corona discharge to describe the behaviour of several key parameters in electrohydrodynamic (EHD) propellers for space applications in near space regions. In these environments, the altitudes can reach from 20km to 100km, pressure ranges from roughly 40Torr to 0.25Torr, and the ambient temperature from 190K to 270K. So, the design of the electric propulsion system must be able to operate within these variations.

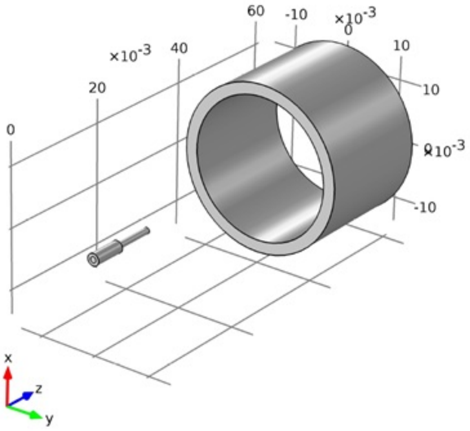

Figure 3.4: Three-dimensional geometry for the EHD thruster: needle-shape anode and cylindrical cathode.

The thruster geometry we used was first proposed by Granados et al. (2016), when he study the influence of three different types of geometries in their respective thrust and efficiency output. We introduced a needle-type anode with a height of 12mm and a hollow cylindrical cathode with a thickness of 1.2mm, an inner radius of 12mm and a height of 21mm. The electrodes were set to be 28mm apart of each other as it can be observed in figure (3.4).

The physics at the walls were divided into three segments, the fluid boundary conditions, the wall boundaries and the surface reactions. The first one describes what will be the fluid behaviour when it contacts with the computational external walls, being a complement of the plasma fluid model. The wall boundaries report the electric behaviour of each component in the domain, such as the anode and the cathode. The last one describes what type of reactions will occur when particles contact the surface walls.

Design the Inlet and Outlet fluid conditions

We choose the boundaries in the inlet wall in a way that the normal stress can be approximately equal to the fluid pressure. In the considered study, the absolute pressure is set to be $p_0 = 10$Torr, simulating then the space environment that the thruster will operate. To prevent that the main fluid back-flows from the boundary to exterior, we adjust the local pressure in the wall, $\hat{p}_{in}$, to be equal or greater then the chosen pressure, creating a pressure gradient in the flow wanted direction. To control this fluid flow we impose that the fluid velocity tangential components to the surface boundary are null. Overall the inlet boundary conditions for the fluid plasma are the following

$$\hat{p}_{in} \geq p_0 \tag{3.18}$$

$$\mathbf{u} \cdot \mathbf{t} = 0 \tag{3.19}$$

$$\mathbf{n}^T \left[-p\mathbf{I} + \mu \left(\nabla \mathbf{u} + (\nabla \mathbf{u})^T \right) \right] \mathbf{n} = -\hat{p}_{in} \tag{3.20}$$

where in the set of equations 3.19-3.20, the vectors **t** and **n** are the tangential and normal vectors of the surface boundary wall. For the outlet wall, the boundary conditions are chosen to also suppress back-flow movement. For this property to happen, the gradient pressure must be the same direction so the outlet pressure at the wall, $\hat{p}_{out}$, must be inferior or equal to the fluid's pressure, the opposite of the inlet boundary. Overall the outlet boundary conditions can be written as

$$\hat{p}_{out} \leq p_0 \tag{3.21}$$

$$\left[-p\mathbf{I} + \mu\left(\nabla\mathbf{u} + (\nabla\mathbf{u})^T\right)\right]\mathbf{n} = -\hat{p}_{out}\mathbf{n} \tag{3.22}$$

where in equation 3.22, the vector **n** is the normal vector to the outlet surface wall.

Design the wall boundaries

All wall boundaries in the fluid model are suppose to be a non slipping walls. That is, the fluid velocity relative to the wall velocity is zero. Since these walls are stationary and fixed, this means the the fluid velocity at the wall is $\mathbf{u} = 0$. However the electrostatic model, the wall boundaries are divided in three different topics, the metal contact, the dielectric contact and the ground. The **ground** implements a zero potential voltage as a boundary condition in the cylindrical cathode. Meanwhile the **metal contact** implements the plasma voltage, that is imposed to the needle type anode. Finally we use the **dielectric contact** boundary wall in the thruster to simulate the response of an external surface charge accumulation, that exists in the quartz tube wall. The set of equations that we used for the anode and cathode boundaries are

$$V_{cathode} = 0 \tag{3.23}$$

$$V_{anode} = V_p \tag{3.24}$$

And to compute the exterior wall we implement the following equation

$$-\mathbf{n}\cdot\mathbf{D} = \sigma_s \tag{3.25}$$

where **D** is the electric displacement field, computed from the electric field and σ_s is the electric charge at the surface that comes form the solution of the differential equation on the boundary

$$\frac{d\sigma_s}{dt} = \mathbf{n} \cdot \mathbf{J}_i + \mathbf{n} \cdot \mathbf{J}_e \tag{3.26}$$

Design the surface reactions

This module assumes that when an excited neutral or an ion interacts with the cathode surface, one electron from the electrode could be emitted, secondary electron emission coefficient, γ_i, with a specific mean energy, ε_i. Since the γ_i is also a discharge parameter, then a study of the influence of this coefficient will be presented in the following chapters in order to have a better understanding of the impact on thruster performance. Nevertheless, to simulate this interaction, the considered module uses a balance of incident fluxes, both for electron density and electron energy density:

$$\mathbf{n} \cdot \mathbf{\Gamma}_e = \left(\frac{1}{2} v_{e,th} n_e\right) - \sum \gamma_i \left(\mathbf{\Gamma}_i \cdot \mathbf{n}\right) \tag{3.27}$$

$$\mathbf{n} \cdot \mathbf{\Gamma}_\varepsilon = \left(\frac{5}{6} v_{e,th} n_\varepsilon\right) - \sum \gamma_i \varepsilon_i \left(\mathbf{\Gamma}_i \cdot \mathbf{n}\right) \tag{3.28}$$

In the set of equations (3.27) and (3.28) the vectors **n**, $\mathbf{\Gamma}_e$ and $\mathbf{\Gamma}_\varepsilon$ represent the normal vector of the surface, the electron flux and electron energy flux respectively. The quantity $v_{e,th}$ is the electron thermal speed. Physically, the first term of the right side is explained by the loss of electrons in the wall due to random motion within a few mean free paths, whereas the second term is the secondary emission flux.

The incident mass flux for species k on a reacting surface is given by (see *Plasma Module Users Guide* (n.d.)):

$$\mathbf{n} \cdot \mathbf{\Gamma}_k = M_k R_{s,k} + M_k c_k \mu_{m,k} z_k (\mathbf{n} \cdot \mathbf{E}) \left[(z_k \mathbf{n} \cdot \mathbf{E}) > 0 \right] \tag{3.29}$$

where the subscript k represents that the associate variable is for species k. The variable M_k, c_k, $\mu_{m,k}$ and z_k are the molecular weight, the molar concentration, the average mixture mobility and the charge number, respectively. The $R_{s,k}$ is the surface rate expression which comes from surface reaction rates and their stoichiometric coefficients. If the species has no electric charge, then the second term in equation is null, since this addition flux contribution come from the ion migration and ensures that when the normal electric field is directed to the wall, there is an out flux of ions due to migration.

Yet it is also important to explain how the surface reactions encompass this module. In order to do that, we configured it so the $\mathrm{R}_{e,wall}$ is computed, which is the contribution to the electron source term due to electron interactions with the walls, in terms of sticking coefficients, γ_f that is either 0 or 1, if the surface is non-reactive or reactive (cathode).

$$\mathrm{R}_{e,wall} = \left(\frac{\gamma_f}{1-\gamma_f/2}\right)\frac{1}{(\Gamma_{tot})^m}\frac{1}{4}\sqrt{\frac{8RT_S}{\pi M_n}}\prod_{k=1}^{Q} c_k \tag{3.30}$$

where γ_{Tot} is the total electron flux incident on the cathode. The exponent m is the reaction order minus 1, c_k represents the the molar concentration of species k, T_S is the surface temperature and, finally M_n and Q are the mean molecular weight of the gas and the total number of considered species, respectively.

In a corona discharge region, the electron density and density of excited species is relatively low, so stepwise ionization is not so important then it is for higher current discharges. When a metastable neutral atom interacts with a surface wall, it will revert to the ground state argon atom with some probability (the sticking coefficient).

Table (3.4) shows the respective γ_i and ε_i for each surface reaction, depending on each surface component. For the developed model, we assume that only the cathode surface emits secondary electrons, and that they are dependent of the external electric field an pressure, being responsible for the neutralization of the ionized particles. The respective energy that they emit is computed through the first ionization energy of the gas minus two times the cathode's work function.

Table 3.4: Surface reactions and respective secondary electron emission coefficient, γ_i, and mean energy of emitted secondary electrons, ε_i in eV.

	γ_i			ε_i [eV]		
Reaction	A	C	W	A	C	W
$Ar^* \rightarrow Ar$	0	0	0	0	0	0
$Ar^+ \rightarrow Ar$	0	$\gamma_i(E/p)$	0	0	$15 - 2\phi$	0
$Ar_2^+ \rightarrow 2Ar$	0	$\gamma_i(E/p)$	0	0	$2 \times (15 - 2\phi)$	0
$Xe^* \rightarrow Xe$	0	0	0	0	0	0
$Xe^+ \rightarrow Xe$	0	$\gamma_i(E/p)$	0	0	$12.7 - 2\phi$	0

A: Anode, C: cathode, W: boundary walls, ϕ: cathode's material work function.

Since the modulation process is very complex, the simulation time and the intensive memory must be optimize. It was chosen that the aim of our research should be the the speed of the numerical calculations, that is the reason that this model only has the most significant species. If we increase in the number of reactions, then the simulation would grow rapidly and the calculation times would become impractical (Gousset et al. (1991), Loureiro and Ferreira (1986)).

Design the computational grid

The non-linear differential equations that were adopted in the two-dimensional EHD model are solved through a finite-element method (FEM). These finite-elements are small triangular grids, where the equations are solved and tested on their vertices. The size of these geometrical components was chosen according to resolve all the equations but not fine enough that could capture small turbulence in the flow, that could lead, potentially to instabilities or even convergence problems within these simulations (Bedolla et al. (2017)).

In the simulation there are regions where it is known that some events occur with higher probability, so it is necessary to improve the mesh grid in this areas. For that to happen, the number of triangular finite elements must be higher then the rest of the space, that is the grid must be finer. Regions such as electrodes, were design with more boundary conditions so the region surrounding them has to contain the smallest elements in the domain, as it is observed in the end of this chapter in figures (3.5) and (3.6).

3.3 DEVELOPING THE THRUSTER PARAMETERS

It was chosen two thruster parameters for the characterization and qualification of the EHD model, the output thrust and the thruster efficiency. This section presents how they are computed in the simulation.

Compute the output thrust

The output thrust produced from the flux of gas expelled through the the EHD thruster is computed trough the exhaust velocity. In this model, the axial component of this gas velocity, is consider to be time invariant and space dependent on the radial component in cylindrical coordinates $v_{ex}(\mathbf{r}, t) = v_z(r)$. The time approximation is considered valid since the thruster studied in this work, reaches a steady-state within milliseconds after the electric discharge. The radial component of the exhaust velocity is also normal to the cathode's output cross sectional area, which allows to write the total trust as the integral over the hollow cathode, where R is the inner radius of the cylindrical cathode.

$$T = 2\pi\rho_f \int_0^R r v_z^2(r) dr \tag{3.31}$$

Calculate the thruster efficiency

In this model, it is chosen the electric efficiency would be a simple and effective way to qualify the EHD thruster, that is the thrust-to-power ratio. To computed it, the model simply divides the output thrust over the power spent on the plasma, as it described in the following expression:

$$\text{T/P ratio} = \frac{T}{P_{plasma}} = \frac{T}{V_p \times I_d} \tag{3.32}$$

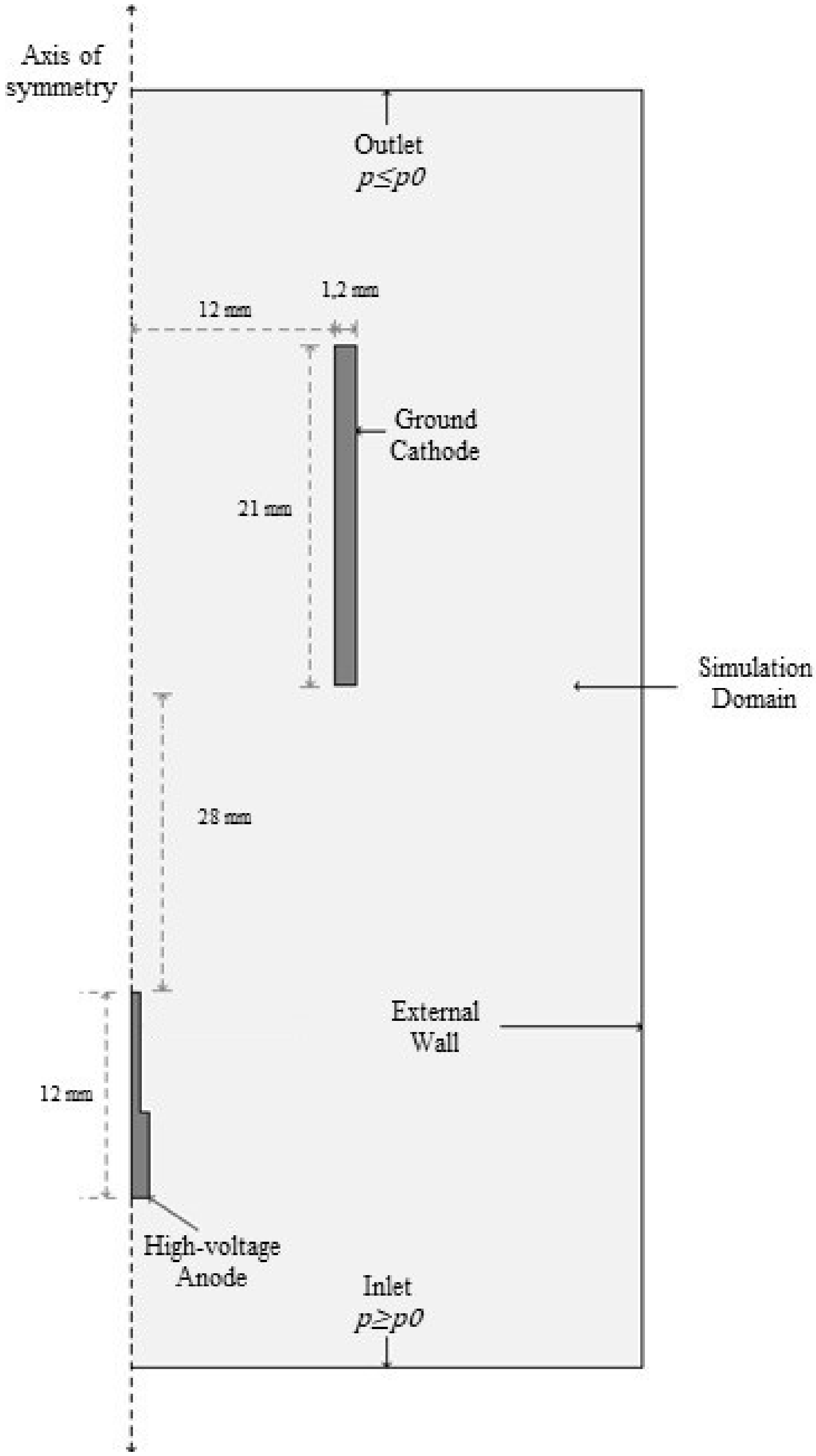

Figure 3.5: Two-dimensional geometry for the single stage cylindrical EHD thruster: needle-shape anode, cylindrical cathode and external walls.

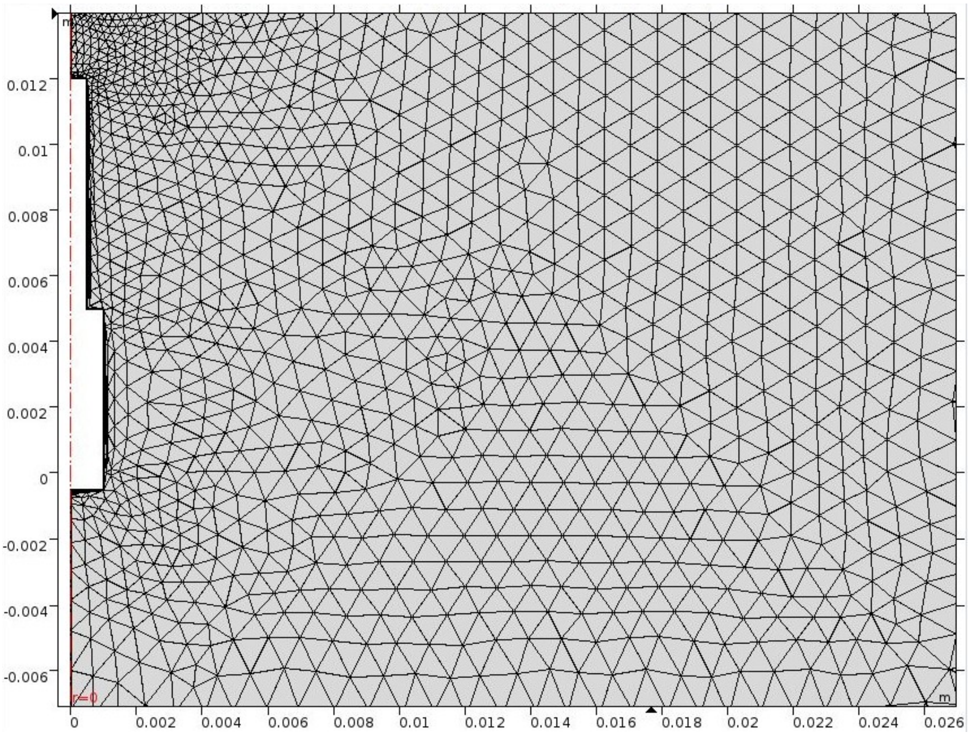

Figure 3.6: Computational grid of simulation around the anode and improve of the mesh density in this region.

Chapter 4.

Study of the electrohydrodynamic density force

The consistency of the appropriate volume force term, **f**, used on the Navier-Stokes equation in a plasma medium was investigated. In the current state-of-art there is some confusion in writing this term (Bedolla et al. (2017); Fylladitakis et al. (2014), Boeuf et al. (2007) and Mushyam et al. (2019)), but there are two main lines, both with their reason, which we will try to clarify by comparing them in this chapter. These two different approaches are treated, one with the space charge density term and the other with ion charge density. This chapter is first composed by a theoretical background and is followed by the experimental results that support it.

4.1 THEORY OF THE EHD DENSITY FORCE

The volume density force that acts on the neutral gas particles is equal to the momentum transfer per unit volume and per unit time of the electric charged particles to the neutral particles. Since the average velocity of the neutral particles are much smaller then the drift velocities of the charged particles, then it is possible to write the volume density forces of ions, according to Boeuf and Pitchford (2005).

$$\mathbf{f} = e(n_i - n_e)\mathbf{E} - k_B T_i \nabla n_i - k_B T_e \nabla n_e \tag{4.1}$$

where k_B is the *Boltzmann* constant and the variables T_i and T_e are respectively the ion and electron temperature, given in eV.

4.2 INFLUENCE OF EACH FORCE TERM

To study the relative importance of each force term we started by introducing the general expression for the electrohydrodynamic force, equation (A.22). The plasma model used in this work was the one similar to the described in table (5.3) on the next chapter of this dissertation,page (58), but the variation of the applied tension was run only in the range from $[0.9 - 20]$ kV, since using higher voltages would result in a saturation of the electric field.

Coulomb force

As it well known from the fundamentals of electrostatics, the first term in equation (A.22) is the electrostatic *Coulomb* interaction between charge particles and electric field can be written as the product of the space charge density with the electric field, that is:

$$\mathbf{f}_c = \rho_c \mathbf{E} \tag{4.2}$$

where $\rho_c = e(n_i - n_e)$.

Figure (4.1) indicates the effect of the applied voltage on the space charge density and it also presents the quasi-neutrality in the thruster's reactor chamber. The lowest charge densities have values below zero, -4.17×10^{-7}Cm^{-3} for 0.9kV and -6.02×10^{-6}C · m^{-3} for 9kV, presenting a higher electron local concentration. On the contrary, the highest charge densities indicates a local presence of a greater number of positive charged particles. These higher concentrations are located in regions were the interaction with the electric field is more intense.

The black arrows correspond in the first row to the electric field Vm^{-1} and in all two-dimensional plots it has a scaling factor, *s.f.*, of 1×10^{-7}. On the other hand, the black arrows in the second row correspond to the *Coulomb* force and they have a varying scaling factor according to the applied voltage. As it is shown, this force term is highly changeable and highly intensifies due to the magnitude of the electric field and the space charge density, as expected.

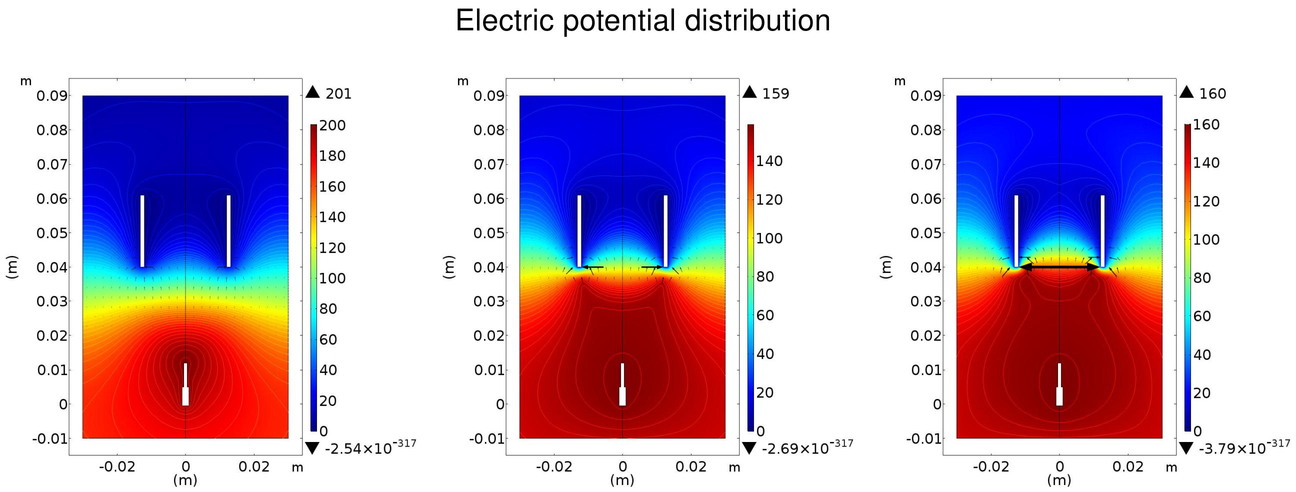
Electric potential distribution

(a) *s.f.* $= 1 \times 10^{-7}$. (b) *s.f.* $= 1 \times 10^{-7}$. (c) *s.f.* $= 1 \times 10^{-7}$.

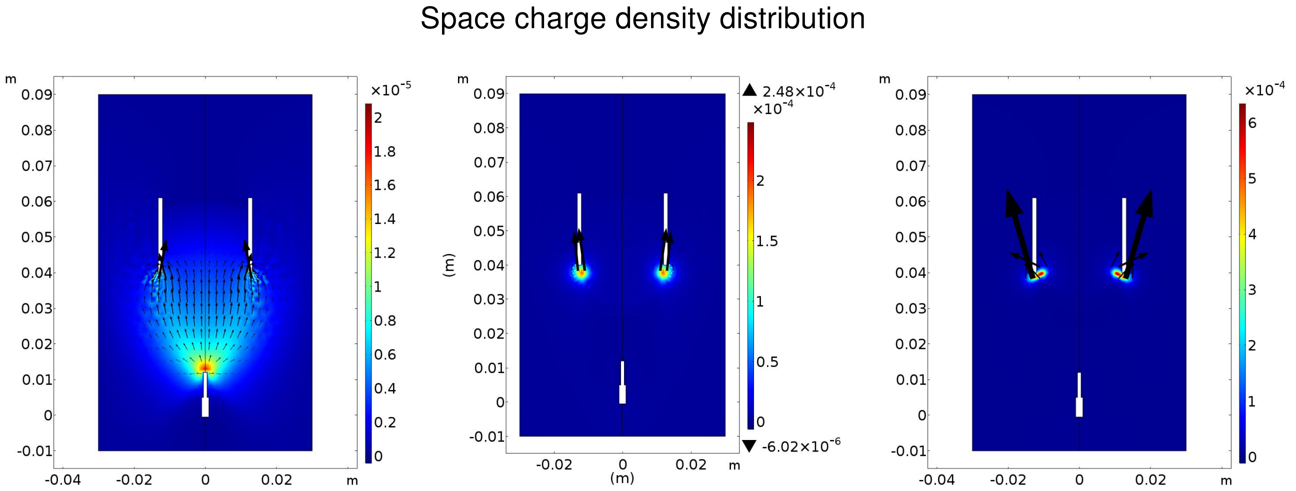
Space charge density distribution

(d) *s.f.* $= 0.01$. (e) *s.f.* $= 0.003$. (f) *s.f.* $= 0.003$.

Figure 4.1: Electric potential distribution V for an initial applied voltage difference of (a) 0.9kV, (b) 9kV, (c) 20kV. Space charge density term, ρ_c, in SI units C · m^{-3}, for an initial applied voltage difference of (d) 0.9kV, (e) 9kV, (f) 20kV. Black arrow represents the *Coulomb* force, $\rho_c \mathbf{E}$, in SI units N · m^{-3}.

Density Gradients

The second term in equation (A.22) is related to the gradients of the charged particles densities

$$\mathbf{f}_\nabla = -k_B T_i \nabla n_i - k_B T_e \nabla n_e \tag{4.3}$$

These terms can be perceived as the gradient of the charge particles energy density, since $k_B T_i n_i$ and $k_B T_e n_e$ are energy densities and the relation between force density and an energy density is that the first one is the negative of the gradient of the second, $\vec{F} = -\nabla U$, where U is an energy density.

Figure (4.2) presents the ion and electron energy distributed over the thruster and it is possible to observe that in regions were the energy is more concentrated, the density gradient increases as well, producing a higher volumic force. However, this force tends to diluted rapidly, pointing towards a highly localized phenomenon. In fact, the density gradient is small, the one observed needs a scaling factor above 1, for instance, for the ion density gradient, or approximately to the unit for the electron density gradient.

Ion energy density

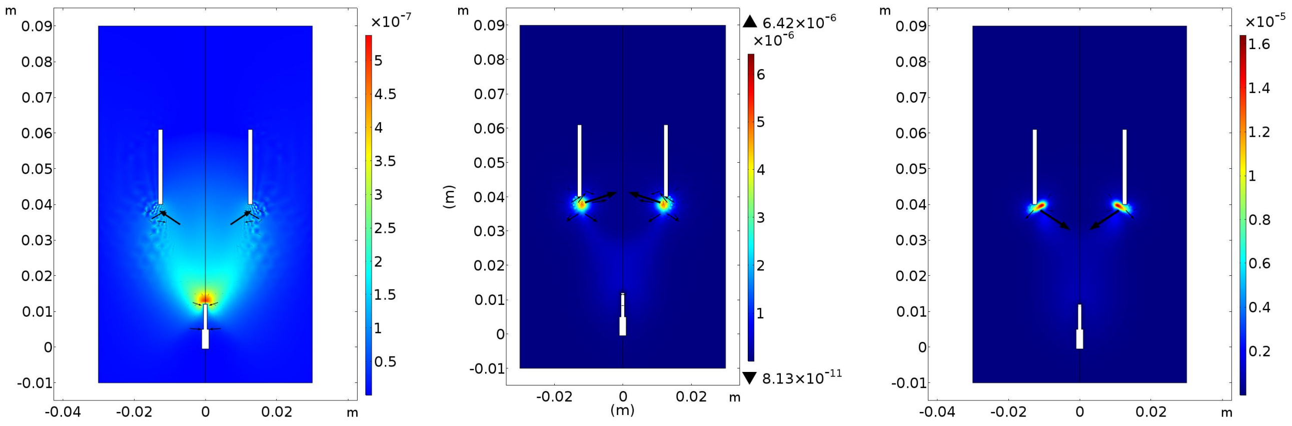

(a) *s.f.* $= 10.$ (b) *s.f.* $= 6.$ (c) *s.f.* $= 1.$

Electron energy density

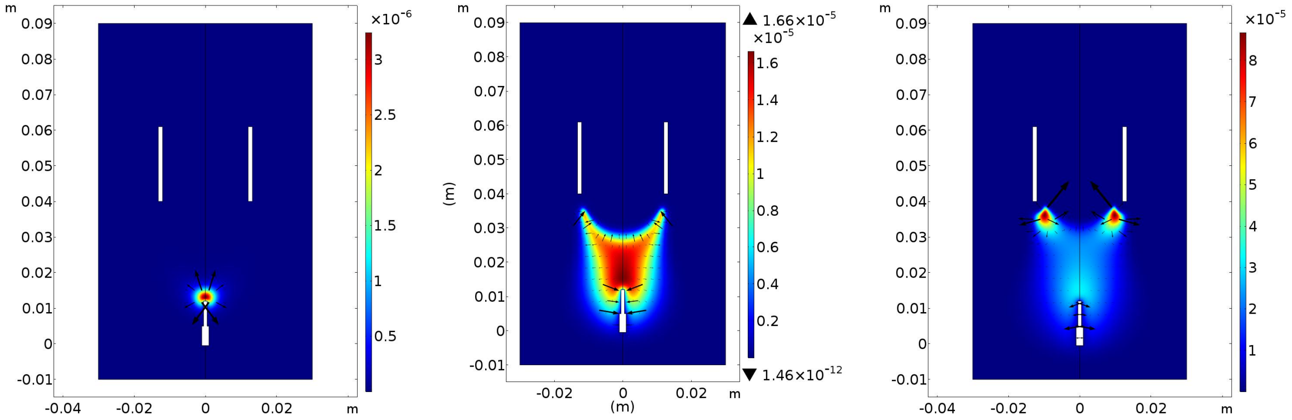

(d) *s.f.* $= 6.$ (e) *s.f.* $= 0.6.$ (f) *s.f.* $= 0.25.$

Figure 4.2: Ion density energy, $k_B T_i n_i$, in SI units J · m^{-3}., for an initial applied voltage difference of (a) 0.9kV, (b) 9kV, (c) 20kV. Black arrow represents the ion density gradient force, $-k_B T_i \nabla n_i$, in SI units N · m^{-3}. Electron density energy, $k_B T_e n_e$, in SI units J · m^{-3}., for an initial applied voltage difference of (c) 0.9kV, (d) 9kV, (e) 20kV. Black arrow represents the ion density gradient force, $-k_B T_e \nabla n_e$, in SI units N · m^{-3}.

Comparison between the two forces

After the observation of each force term in their respective physical ground, it was decided that a direct comparison should be also appropriate. So, to compare both forces, we plotted them in the same figures.

Overall, figure (4.3) shows the intensity of each force term, being the *Coulomb* force the most predominant force, reaching above two orders of magnitude over the density gradients although both increase with the increase of the applied voltage. This can be deduced by the scaling factors that are presented, the red colour corresponds to the gradient forces and the colour blue to the space charge density force.

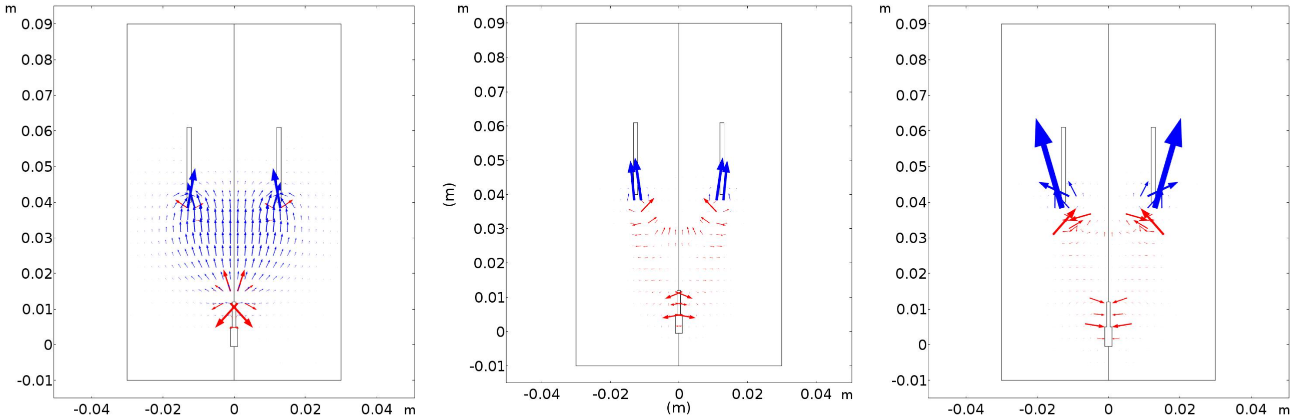

(a) *s.f.* $= 6$; *s.f.* $= 0.01$. (b) *s.f.* $= 0.6$; *s.f.* $= 0.003$. (c) *s.f.* $= 0.25$; *s.f.* $= 0.003$.

Figure 4.3: Comparison between the ions and electron density gradients, red arrows, and the *Coulomb* force, blue arrows, in SI units N $\cdot$ m^{-3} for for an initial applied voltage difference of (a) 0.9kV, (b) 9kV, (c) 20kV. The scaling factor, *s.f.*, indicates a predominance of the *Coulomb* force with values above two orders of magnitude.

4.3 INFLUENCE OF EACH CHARGE DENSITY

Setting the *Coulomb* force as the predominant force, it was decided to study the influence of each charge density. We decided first, introducing only the ion charge density and posteriorly study the influence of the space charge density.

Use of the ion charge density

The well-known quasi-neutrality of plasma indicates that the space charge density, $\rho_c = e(n_i - n_e)$, in a plasma is a small term, since electrons and positive ions have approximately equal densities. For a corona discharge, a non-equilibrium medium with a low ionization degree, exists two different regimes, the ionization and the drift. In the ionization zone, area immediately after the high voltage electrode, electrons tend to gain energy from the electric field and due to inelastic collisions with the neutral particles,whom they transmit this energy, creating electron-ion pairs, mainly responsible for the quasi-neutrality.

Nevertheless in the drift regime, the space charge density as a positive value and therefore $\rho_c = en_i$ because of the higher mobility of electrons in relation of the ionized particles (which is related to the vary different values of the respective masses) and due to the fact that in this area, the electric charged particles do not have enough energy to react with the neutral gas particles. Therefore negligible, once the electron mobility is much higher then the ion mobility, so electrohydrodynamic force in equation (4.2) is simply (Martins (2013)):

$$\mathbf{f} = \frac{\mathbf{J}_i}{\mu_i} = \rho_i \mathbf{E} = \mathbf{f}_i \tag{4.4}$$

Then we introduce the ion current density vector, $\mathbf{J}_i$, into continuity equation in the stationary regime equation and we get

$$\frac{\partial \rho_i}{\partial t} + \nabla \cdot (\mu_i \rho_i \mathbf{E}) = 0 \tag{4.5}$$

In this regime, the first term in the left side is zero. Using the mathematical expressions for the divergence, we get

$$\mu_i \rho_i (\nabla \cdot \mathbf{E}) + \mu_i (\nabla \rho_i \cdot \mathbf{E}) = 0 \tag{4.6}$$

However, it is necessary to take into account the divergence of the electric field, that relates the total charge density, through the local form of the *Gauss*'s law.

$$\nabla \cdot \mathbf{E} = \frac{\rho_c}{\varepsilon_0} \tag{4.7}$$

where ε_0 is the permittivity of free space. Then, by replacing equation(4.7) in the equation (4.6), we get

$$\rho_i \frac{\rho_c}{\varepsilon_0} + \nabla \rho_i \cdot \mathbf{E} = 0 \tag{4.8}$$

which is a different form of writing the continuity equation in the stationary regime. To simulate study the external force term, we simply change the force density term to ion space charge density force, $\mathbf{f}_i = \rho_i \mathbf{E}$ in the *Navier-Stokes* equation (NSE).

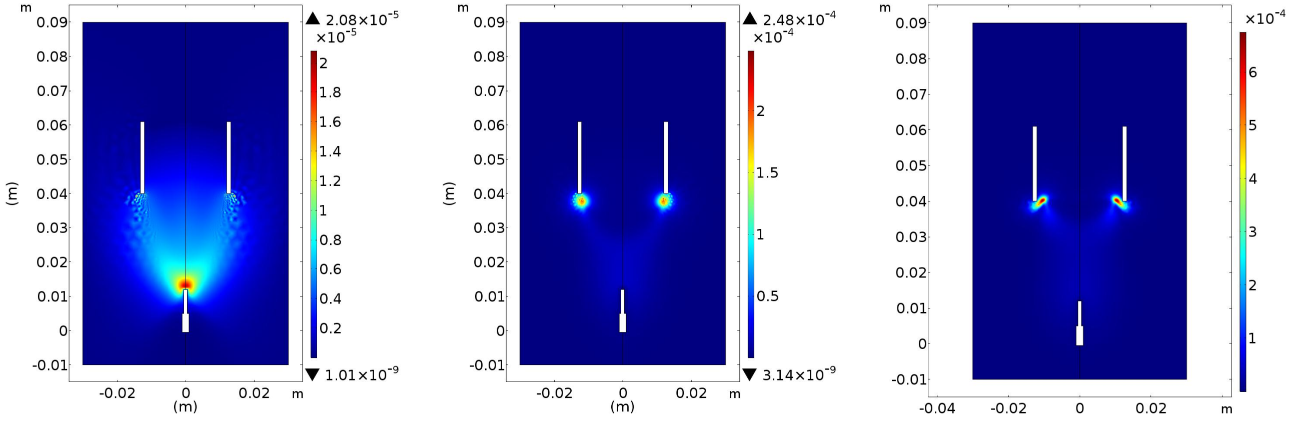

(a) (b) (c)

Figure 4.4: Ion Charge density term, ρ_i, in SI units C · m^{-3}, for an initial applied voltage difference of (a) 0.9kV, (b) 9kV, (c) 20kV.

In figure (4.4) it is possible to observe the effect of the applied voltage in the ion charge density. Overall we see the quasi-neutrality in the reactor chamber of the thruster, the lowest density is 1.01×10^{-9}C · m^{-3} for 0.9kV and the highest density it is found for the 20kV, with approximate value of 6.5×10^{-4}C · m^{-3}. Also, it is possible to notice that for a small values of voltage, the maximum value is found near the anode, effect previously noticed, that could indicate we are not in the thruster favourable regime and that contradicts the assumption of trajectories of the electric charge particles, negative charge particles flow to higher voltages and positive charge particles flow to lower voltages.

Use of the space charge density

Through the *Gauss*'s theorem, the *Coulomb* force can be written as the divergence of a electrostatic pressure tensor, as:

$$\mathbf{f}_c = \rho_c \mathbf{E} = \varepsilon_0 \mathbf{E}(\nabla \cdot \mathbf{E}) = \nabla \cdot \mathbb{T} \tag{4.9}$$

where $\varepsilon_0 \mathbf{E}(\nabla \cdot \mathbf{E})$ is the divergence of electrostatic pressure symmetric second-order rank tensor, $\mathbb{T}$. Physically, this tensor represents a stress acting on a surface and has units of force per unit area, where diagonal elements represent pressures and the non-diagonal elements are shears

(Griffiths (2013)). And by apply the divergence operator in the diagonal components in a pressure tensor gives a electrostatic pressure gradient. In this study we pretend to observe the pressure gradient inside the thruster.

Since the electrostatic pressure is proportional to the quadratic electric field, then the pressure gradient implies that in regions of higher electrostatic pressure, with high electric field, the plasma pressure will be lower if compared to neighbouring areas. This difference will cause an inflow from the particles in these regions of higher pressure (Roth (2001)). In other words, both charged and neutral particles will accelerate to higher electrostatic pressure regions.

These simulations were also run by using the same parameters that are described in table (5.3) and in order to observe the electrostatic pressure gradient, we simply change the term in the NSE to space charge density force, $\mathbf{f}_c = \rho_c \mathbf{E}$.

The gradient of the electrostatic pressure is observed also in figure (4.5) near the cathode, since for regions of higher electric field (black arrows in the electric potential distribution), we can observe a higher concentration of neutral argon particles, corresponding also to regions of higher ion charge densities.

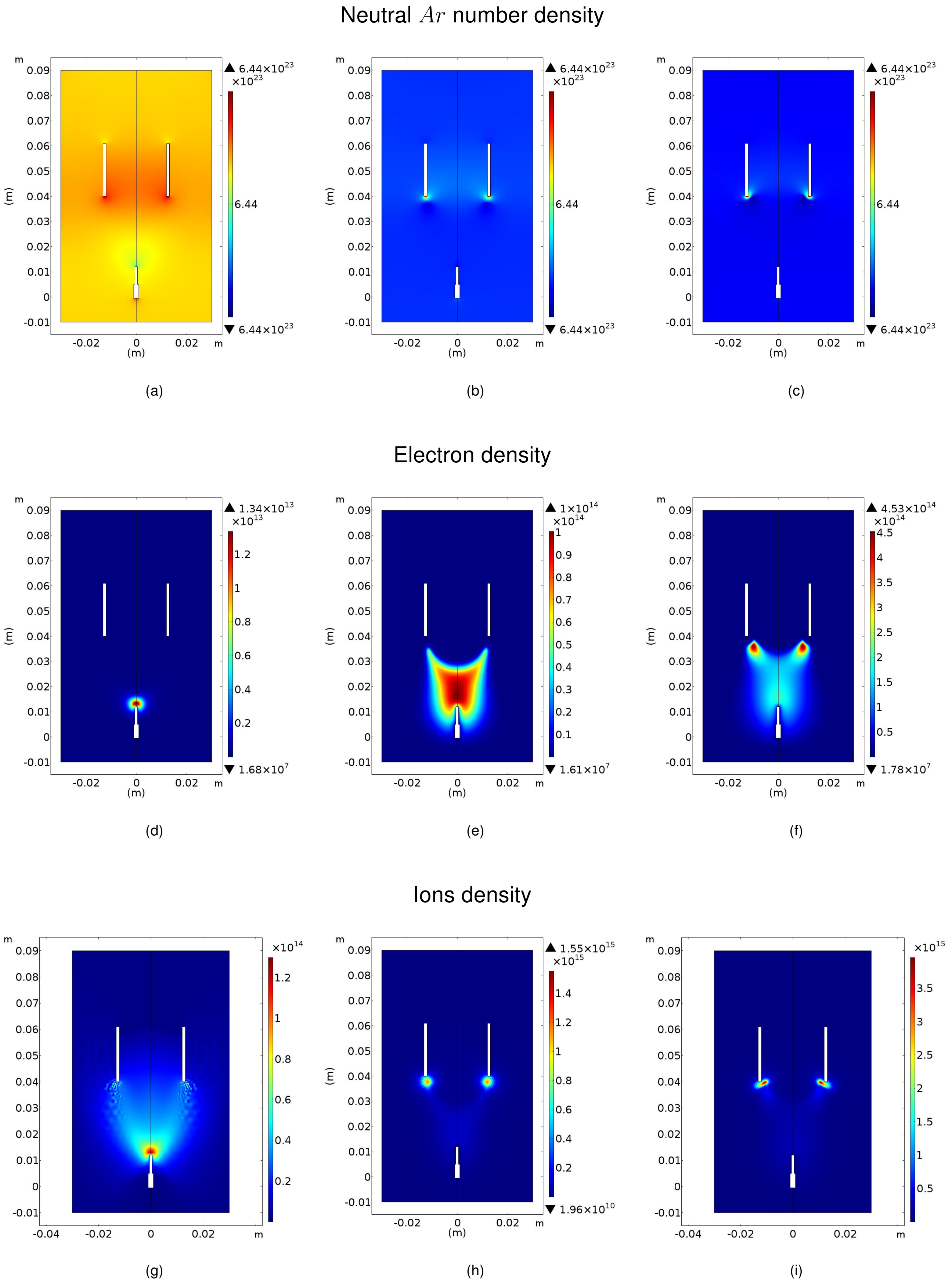

(a) (b) (c)

(d) (e) (f)

(g) (h) (i)

Figure 4.5: Particle densities, in SI units m^{-3}, for a varying applied voltage of (a,d,g) 0.9kV, (b,e,h) 9kV and (c,f,i) 20kV. In the first row are shown the Ar neutral number density, in the second row we presents the e^- number density and the third row shows the $Ar^+ + Ar_2^+$ ions number densities. The distribution of all species shows the influence of the electrostatic pressure.

Comparison between the charge densities

In order to have a proper way to compare the use of both terms, we resort to two different criteria: being the first one based on a direct comparison between the two previously discussed, and the second one being based on the fundamentals of plasma behaviour, the continuity equation in the stationary regime.

Ion current density vector, $\mathbf{J}_i$

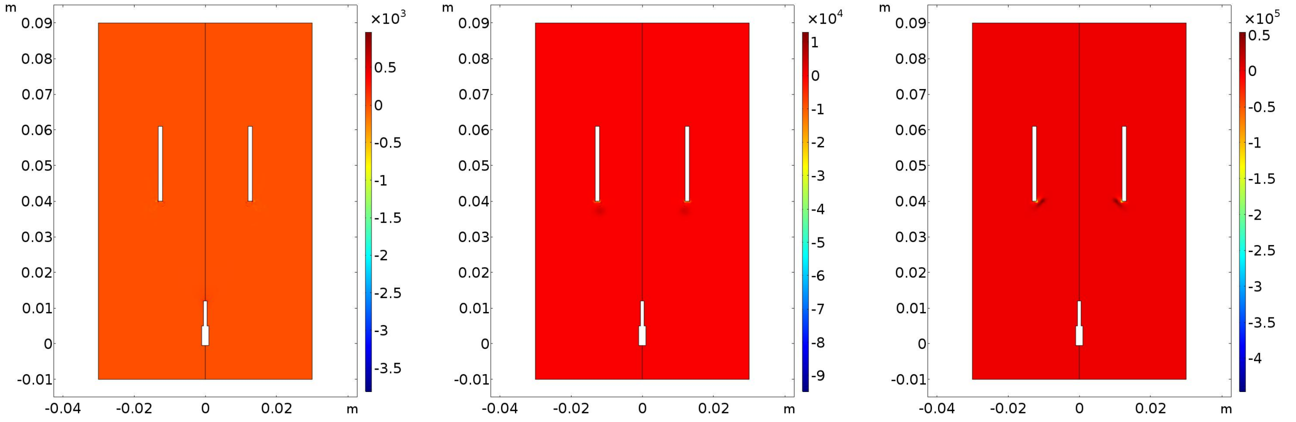

(a) (b) (c)

Total current density vector, $\mathbf{J}$

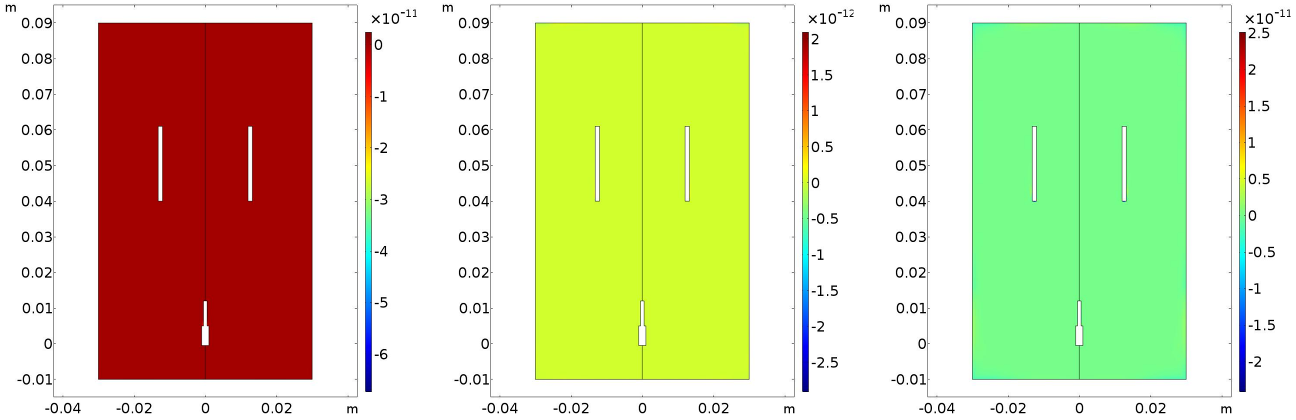

(d) (e) (f)

Figure 4.6: Continuity equation in the stationary regime, $(\nabla \cdot \mathbf{J} = 0)$ in A $\cdot$ m^{-3} SI units. Use of the ion current density vector $\mathbf{J}_i$ for an applied voltage of (a) 0.9kV, (b) 9kV, (c) 20kV. Use of the total current density vector, ions plus electrons current densities vectors $\mathbf{J} = \mathbf{J}_i + \mathbf{J}_e$ for an applied voltage of (d) 0.9kV, (e) 9kV, (f) 20kV.

The simulation results regarding both mathematical approaches to the continuity equation in the stationary regime, which is represent on figure (4.6), for our plasma show very very different results. When using only the ion current density vector, $\mathbf{J}_i$, to resolve this equation, or $\nabla \cdot \mathbf{J}_i = 0$, the observed that although is practically equal to zero throughout the working region, in some areas, this is not verified, pointing to the creation of positive and/or negative charges - the continuity equation, reaching values from $10^3 - 10^5$A · m^{-3}, depending on the applied voltage. On the other hand, when the total current density vector, **J**, is used in this calculation, the equation turns practically equal to zero throughout the thruster, since the main values reaches only in the range of $10^{-12} - 10^{11}$A · m^{-3}, depending on the applied voltage, which are essential by computational zeros.

4.4 THRUSTER PERFORMANCE DUE TO EACH FORCE

Our simulation present a very intriguing results. In terms of thruster performance we found out that both external force terms show the same output, regarding the applied voltage. Table (4.1) presents each thrust and thrust-to-power ratio produced by each force term. These results indicate that the predominant term in the calculation of these density force is the one with the ion charge density and that the gradient forces don't influence that much the force term, where the thrust only differs in the decimal places. In the final simulation, the thrust resulted in an difference of 15[nN] because to have convergence, the simulation mesh grid was reduced, reducing also the accuracy of the data.

Table 4.1: Simulation results for each density force, $\mathbf{f}_i$, $\mathbf{f}_c$ and $\mathbf{f}_c + \mathbf{f}_\nabla$ in the single stage argon EHD thruster by varying the applied voltage of for a fixed ballast resistor of $500\text{M}\Omega$.

Force [N · m^{-3}]	Voltage [kV]	Thrust [nN]	Power [mW]	T/P ratio [mN/kW]
$\mathbf{f}_i$	0.9	5.46	0.28	19.46
	9	108.84	2.81	38.73
	20	536.65	6.37	84.19
$\mathbf{f}_c$	0.9	5.45	0.28	19.44
	9	107.77	2.81	38.36
	20	534.93	6.35	84.25
$\mathbf{f}_c + \mathbf{f}_\nabla$	0.9	5.45	0.28	19.44
	9	107.81	2.81	38.38
	20*	521.90	6.37	81.90

* this simulation result was computed with a smaller mesh grid.

4.5 CONCLUSION

In conclusion it was shown experimentally using the computational simulation, that the electrohydrodynamic density force can be approximated only by/ the *Coulomb* force since the density gradients forces are highly localized and do not influence the output thruster performance.

On the other hand, the results show a higher pressure near the cathode, corresponding to a region with a higher electric field and a surrounding area with the lower pressure. Additionally, a higher concentration of ionic particles are observed in these higher-pressure areas, also leading to a higher concentration of neutral particles in these regions. From direct comparison and from the observed performance results, such as thrust output and thrust to power ratio, it was found that both spacial charge density and ion volume charge density give very similar results, given evidence that the last one is the predominant term in the calculation of ρ_c. However, this study has shown that the use of the ion current density in the continuity equation in stationary regime leads to the abnormal creation of both positive and negative charged particles, making the use of the ion charge density in the external force term misleading. In conclusion, to be consistent with the physical theory, the external force term to be used in the electrohydrodynamic propulsion model should be the one containing the space charge density since this is the most important term in the force density expression, that for it can be approximated by the *Coulomb* density force, $\mathbf{f} \approx \mathbf{f}_c = e(n_i - n_e)\mathbf{E}$.

Chapter 5.

Optimization of an argon propellant EHD thruster

The first phase of this experiment consisted in understanding the behaviour of electrohydrodynamic cylindrical plasma thrusters. This type of insight was first studied by Granados et al. (2017), where he presented a series of testes for the EHD thruster, using argon , nitrogen and oxygen as the propellants gases and different cathode geometries. He studied the influence of several parameters, such as discharge current, gas temperature, pressure and secondary emission coefficient, in the overall net thrust and efficiency. It's best results with argon in a cylindrical geoemtry delivered a thrust of 4.7nN (with a length of 21mm and an inner radius of 12mm). In this work, a similar study will be made but we will use the noble gas Argon, as the propellant gas, since it is less reactive.

5.1 ARGON SINGLE STAGE EHD THRUSTER

We started by observing the influence of the discharge current, first by reducing the ballast resistor and fixing the applied voltage, and then by fixing the resistance value and varying the applied voltage. Next we studied the influence of the cathode's intrinsic geometry, by varying the value of the cathode's inner radius and then the cathode's length so we could optimize these parameters. Finally we studied the influence of the secondary electron emission coefficient, since it has a great impact in the neutralization of the expelled gas.

In all of these simulations argon gas is assumed to be at a constant pressure of 10Torr and at a constant temperature, 300K, therefore simulating the environment where they will be used, orbit transfer or space manoeuvring.

Influence of the discharge current

The starting point for improving the argon cylindrical thruster was to change the degree of ionization, physical quantity that represents the proportion of charged particles in a neutral plasma, seeing that we had very low values in general, the highest being 2.4×10^{-9}. To increase the number of ionized particles, it is necessary to apply a stronger current between the electrodes. This is done by two methods, by reducing the ballast resistor or by increasing the applied voltage.

This current is controlled by the RC-coupling circuit and by varying the value of the series resistor, keeping the applied voltage at a constant value. In a perfect capacitor, no electric charge flows from one capacitor plate into another, in this model we assume that the RC circuit is composed by one of this capacitors, which in these simulations has a value of 1pF, and so we assume, in a first approximation, that the current discharge is simple computed by the direct application of *Ohm*'s law, $I_d = V_{in}/R_B$.

Variation of the ballast resistor

By maintaining the corona self-sustain discharge regime, we observed the influence of the ballast resistor in the argon single stage EHD thruster. The parameters used in this first set of simulations are described in table (5.1).

Table 5.1: Simulation parameters used to observe the influence of the discharge current in the single stage argon EHD thruster by varying the ballast resistor.

Parameter	Value
Applied Voltage	3kV
Ballast Resistor	$[500 - 2500]$ MΩ
γ_i	0.05
η	2.23×10^{-5}Pa.s

We found out that by decreasing the resistor value, we increased the number of charged particles, as we were expecting. In figure (5.1) this behaviour is well observed. For instance, in the first picture of the second and third rows, corresponding to a resistor value of $2500\text{M}\Omega$, the maximum concentration value of electrons was 4.49×10^{12}m^{-3} and 1.65×10^{14}m^{-3} for ions.

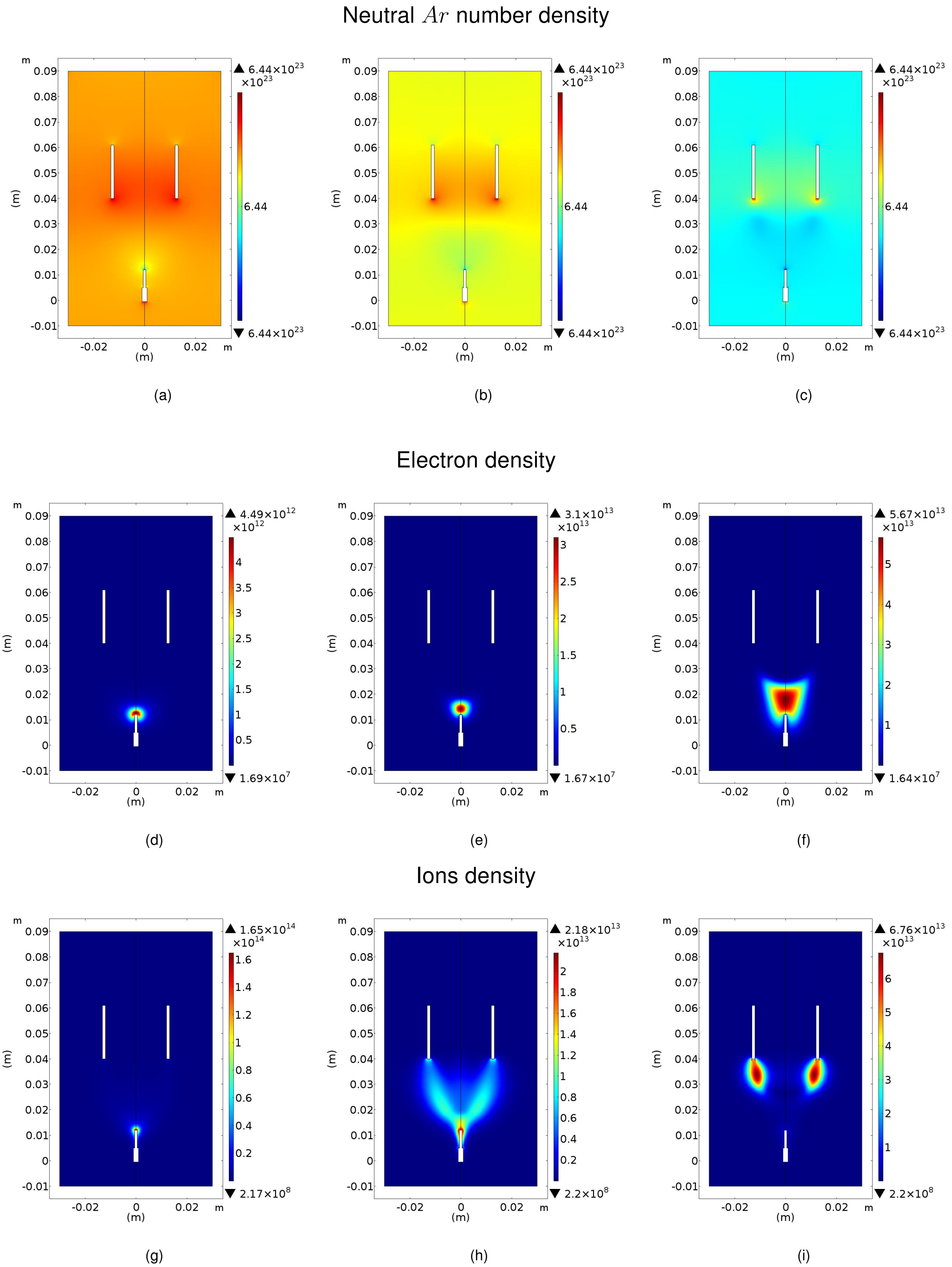

(a) (b) (c)

(d) (e) (f)

(g) (h) (i)

Figure 5.1: Particle densities, in SI units m^{-3}, for a varying ballast resistor of (a,d,g) $2500\text{M}\Omega$, (b,e,h) $1500\text{M}\Omega$ and (c,f,i) $500\text{M}\Omega$. First row are shows the Ar neutral density, the second row presents the e^{-} density and the third row shows the Ar^{+} ion density.

However, these values increase one order of magnitude when the resistor value was reduced by five times, to $500\mathrm{M}\Omega$ in the case of electrons, reaching values of 5.67×10^{13}m^{-3}. Nevertheless, the highest concentration value for the ions was reduced due to the fact that they migrate from the anode to the cathode, having a greater distribution with a density of 6.76×10^{14}m^{-3}.

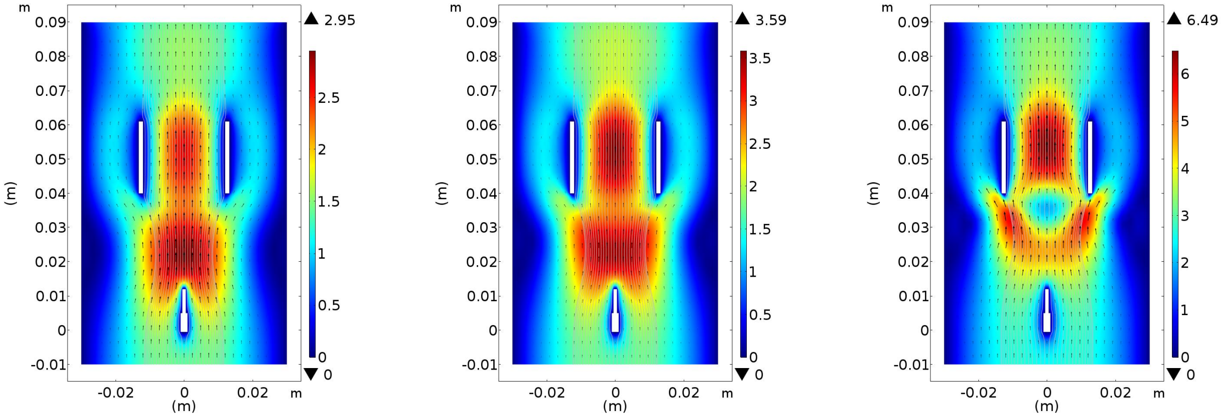

(a) (b) (c)

Figure 5.2: Two dimensional fluid velocity distribution, in SI units cm·s^{-1}, for a varying ballast resistor of (a) $2500\mathrm{M}\Omega$, (b) $1500\mathrm{M}\Omega$ and (c) $500\mathrm{M}\Omega$.

In figure (5.2) we observe the two dimensional profile of the plasma main velocity. From the decrease of the ballast resistor, this profile change considerable, reaching maximum values of 6cm $\cdot$ s^{-1}, a three times increase regarding the previous developed thruster.

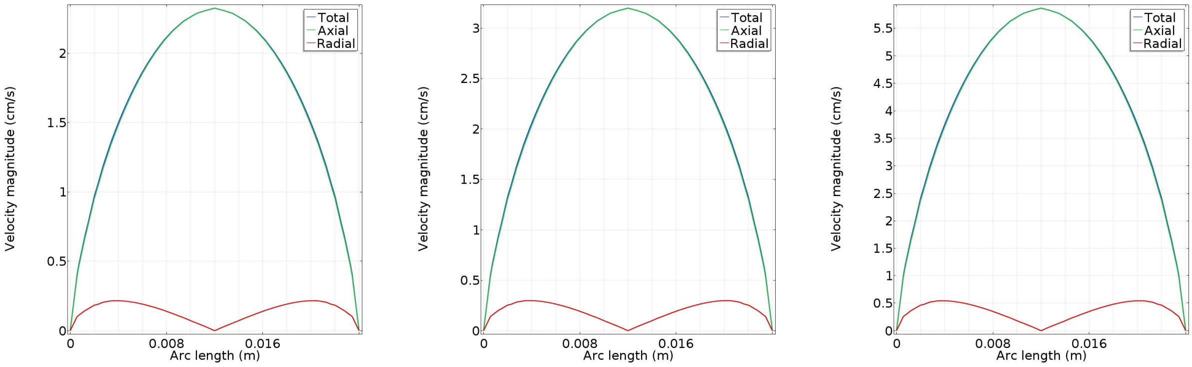

(a) (b) (c)

Figure 5.3: Fluid velocity components at cathode's exit, in SI units cm $\cdot$ s^{-1}, for a varying ballast resistor of (a) $2500\mathrm{M}\Omega$, (b) $1500\mathrm{M}\Omega$ and (c) $500\mathrm{M}\Omega$.

As it is shown in figure (5.3), the radial component is practically negligible when compared the the axial component. From the implemented boundary conditions, the magnitude of the fluid velocity is zero at the cathode's wall due to laminar fluid behaviour. As it is expected the decrease of the ballast resistor produces a higher cathode's exit velocity, reaching values near the 6cm$\cdot$s^{-1} with $500\mathrm{M}\Omega$. These results show that by reducing the resistor value, the plasma was accelerated for a two times grater speed.

Table 5.2: Simulation results for the study of the influence of discharge current in the single stage argon EHD thruster by varying the ballast resistor for a fixed applied voltage of 3kV.

Resistor $[\mathrm{M}\Omega]$	Current $[\mu\mathrm{A}]$	Thrust [nN]	T/P ratio [mN/kW]
2500^*	1.2	4.11	17.97
2000	1.5	5.46	19.44
1500	2.0	7.75	21.24
1000	3.0	12.27	23.31
750	4.0	16.75	24.55
500	6.0	25.86	26.27

Posteriorly, the thruster was evaluated in terms of its intrinsic parameters. Both thrust and thrust-to-power ratio were computed directly on the software and are displayed in table (5.2). As it can be observed, by changing the discharge current from 1μA to 6μA, the propellant force increases more then five times, from 4nN to around 26nN. Even though there was an increase on the current spent, and consequently an increase on the power spent on the plasma, the efficiency ratio did not decrease but increased as well, stressing the fact that there was a significant improve in the work regime of the thruster.

Variation of the applied voltage

Setting the most favourable value of the ballast resistor in $500\mathrm{M}\Omega$, we decided that we should study the influence of the applied voltage in the considered thruster. At this point we were expecting that by increasing the voltage, the discharge current would increase, producing a higher output thrust. We modulated the plasma gas to work in the range of low potential differences of 900V between electrodes, to a higher applied voltage of 40kV The set of conditions used in this simulation is collected in table (5.3).

One way that the applied voltage influences the operation of the EHD thruster is the effect that it has on the electric potential distribution, which is an essential factor since the electric field is the most important role in the conversion of electric to mechanical energy. In figure (5.4) it is possible to observe the direct influence that a higher applied voltage has in the electric field lines. Although the maximum value of the electric potential distribution is higher at low voltages, at 20kV, the horse shoe profile intensifies. Consequently the voltage drop increases leading to a higher potential gradient near the cathode.

Table 5.3: Simulation parameters used to observed the influence of the discharge current in the single stage argon EHD thruster by varying the applied voltage.

Parameter	Value
Applied Voltage	$[0.9-40]$ kV
Ballast Resistor	$500\mathrm{M}\Omega$
γ_i	0.05
η	2.23×10^{-5}Pa.s

From *Gauss*'s law, we compute the magnitude of the electric field, represented as black arrows. From the results, we can assess that this geometry is not optimal because of the direction of the electric field. Although most of the vectors are aligned with a favourable direction (the azimuthal direction), the highest intensity vector has only a radial component, which accelerates the particle charges to this regions.

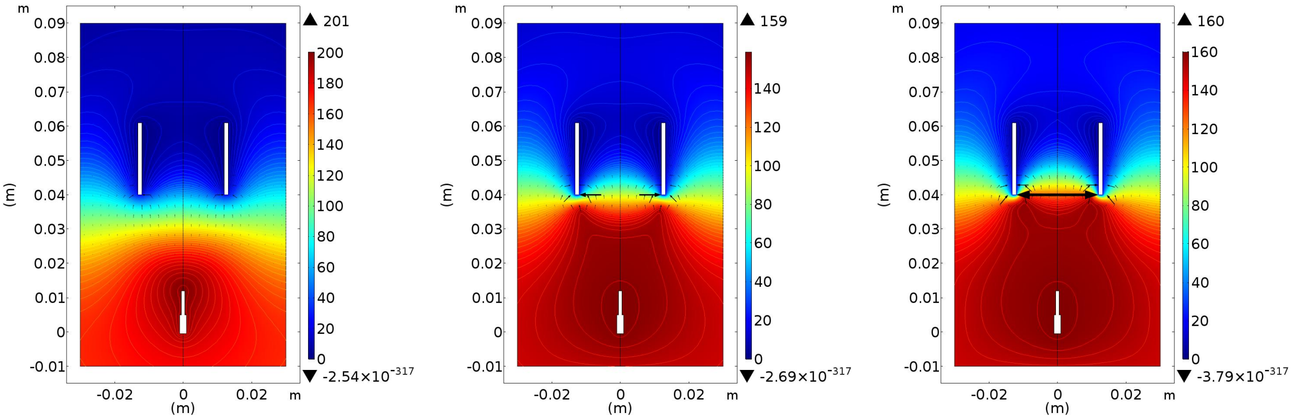

(a) (b) (c)

Figure 5.4: Electric potential distribution V for an initial applied voltage difference of (a) 0.9kV, (b) 9kV, (c) 20kV.

This phenomena is depicted in the set of pictured from figure (5.7), where at 9kV and 20kV, it was found out that highest values for both gas particles, either neutral atoms or ions, are more concentrated near the cathode. One interesting effect is that due to the horse shoe profile, the electrons scatter along this high potential plateau, reaching as well this near cathode region. On the opposite hand, at 900V, all concentrated charged particles migrate to near the anode, as we will see later, but this did not produce the optimal thrust results. Continuing at 20kV, we found out that the ions did not only reached the cathode but they also entered the cylindrical volume, producing the optimal thruster regime. From this point on it was assessed that to produce the best thruster, the ions should be concentrated in regions inside the cathode and not below or even near the anode.

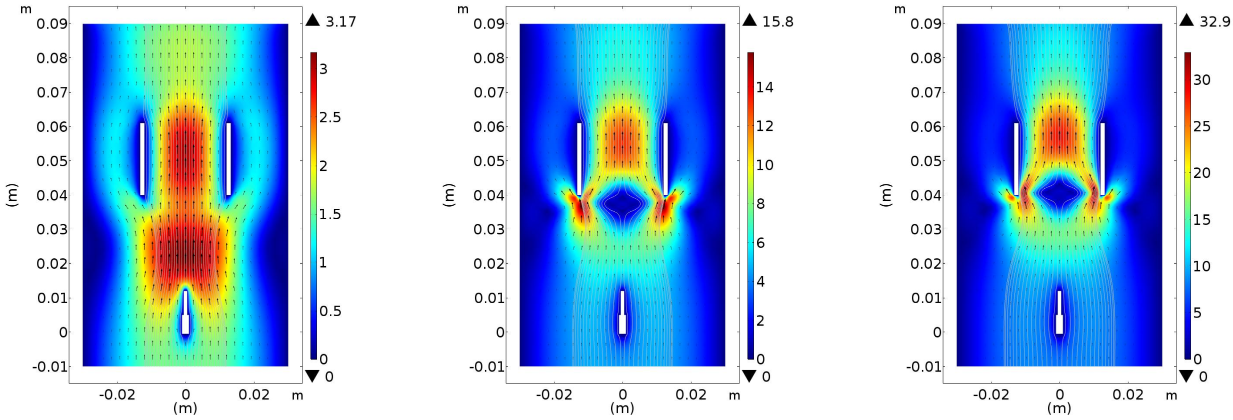

(a) (b) (c)

Figure 5.5: Two dimensional fluid velocity distribution, in SI units cm · s^{-1}, for a varying applied voltage difference of (a) 0.9kV, (b) 9kV, (c) 20kV.

Being the electric field so intense near the cathode, causes the ionized particles to collide against the neutrals with a greater impact, transferring them more momentum. This is why the main fluid gas is faster in this regions than the surrounding areas as it is shown in figure (5.5).

Meanwhile, another interesting phenomenon occurs in the middle cathode's entry point. The gas tends to slow down to a stationary level as the discharge current increases from 10^{-6}A to 10^{-5}A. This effect also appears when we change the ballast resistor to 500MΩ but it is accentuated when higher voltages are applied. At first we though that it could be one vortex, but after consulting the velocity results in this area, non of them were at the opposite direction of the flow which excluded the vortex formation hypothesis. Then, we deduced that this phenomenon happens mainly by neutral - ions collisions, by observing the potential electric distribution, the electric field in this region and knowing that the motion of neutral atoms occurs due to collision with accelerated ionized particles.

Overall, by increasing the applied voltage, the gas fluid velocity increase as well, as it was expected. From maximum values of 2.71cm · s^{-1} at 900V and 15.8cm · s^{-1} at 9kV, the fluid velocity reached speeds above the 32cm · s^{-1} when the applied voltage was 20kV. The same can be said of the fluid velocity at the cathode's exit. In this region the expelled velocity reached velocities of near 27cm·s^{-1} at high difference potential, reporting a 9 times increase in comparison to the previous developed argon cylindrical thruster. Figure (5.6) displays this increase for three different applied voltages. At 900V the expelled velocity, reaches values of near 2.6cm · s^{-1} and for 9kV this voltage increased to a maximum value of 12cm · s^{-1}. From the quadratic profile it is possible to observe the laminar behaviour of plasma fluid, due to the fact that in the border walls, the velocity is zero.

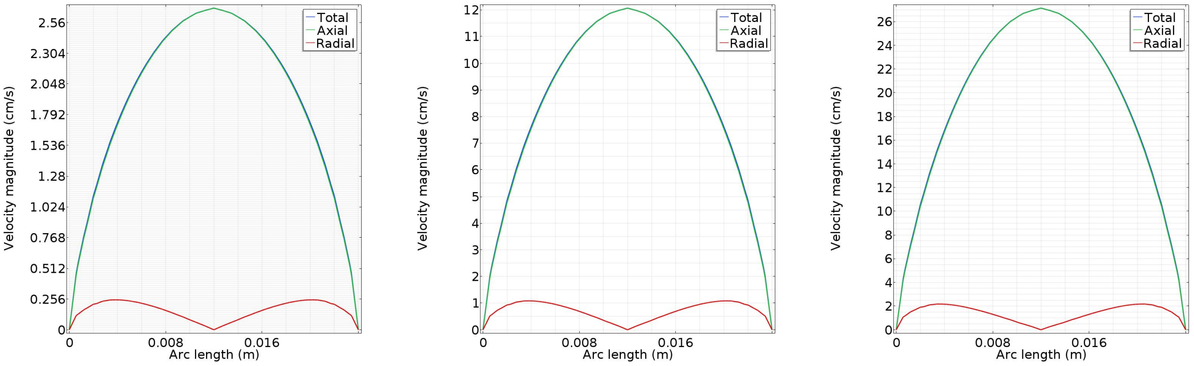

(a) (b) (c)

Figure 5.6: Fluid velocity components at cathode's exit, in SI units cm · s^{-1}, for a varying applied voltage difference of (a) 0.9kV, (b) 9kV, (c) 20kV.

By integrating the axial component of the velocity through the area surface of the cathode's exit, we compute the output thrust and then, by using the power we have to spent to stabilize and produce the plasma, we computed the thrust-to-power ratio. Table (5.4) shows how the thruster parameters change with the applied voltage and from them, we observe that the thrust reaches values of 550nN a 100 times increase from the previous developed thruster, reaching an efficiency of 86.24mN$/$kW, the highest so far. Yet we also found out that there was an optimal voltage,20kV, since higher voltages produced the same thrust and reduce the thruster efficiency. For instance at 30kV, the thrust decreases more then 10nN and at 40kV, the thruster efficiency was reduce in half.

Table 5.4: Simulation results for the study of the influence of discharge current in the single stage argon EHD thruster by varying the applied voltage for a fixed ballast resistor of 500MΩ.

Voltage kV	Current [μA]	Thrust [nN]	T/P ratio [mN/kW]
0.9	1.8	5.45	19.44
3	6.0	25.86	26.27
9	18.0	107.77	38.36
12	24.0	181.14	48.40
20	40.0	549.93	86.24
30	60.0	521.09	81.56
40	80.0	521.04	40.90

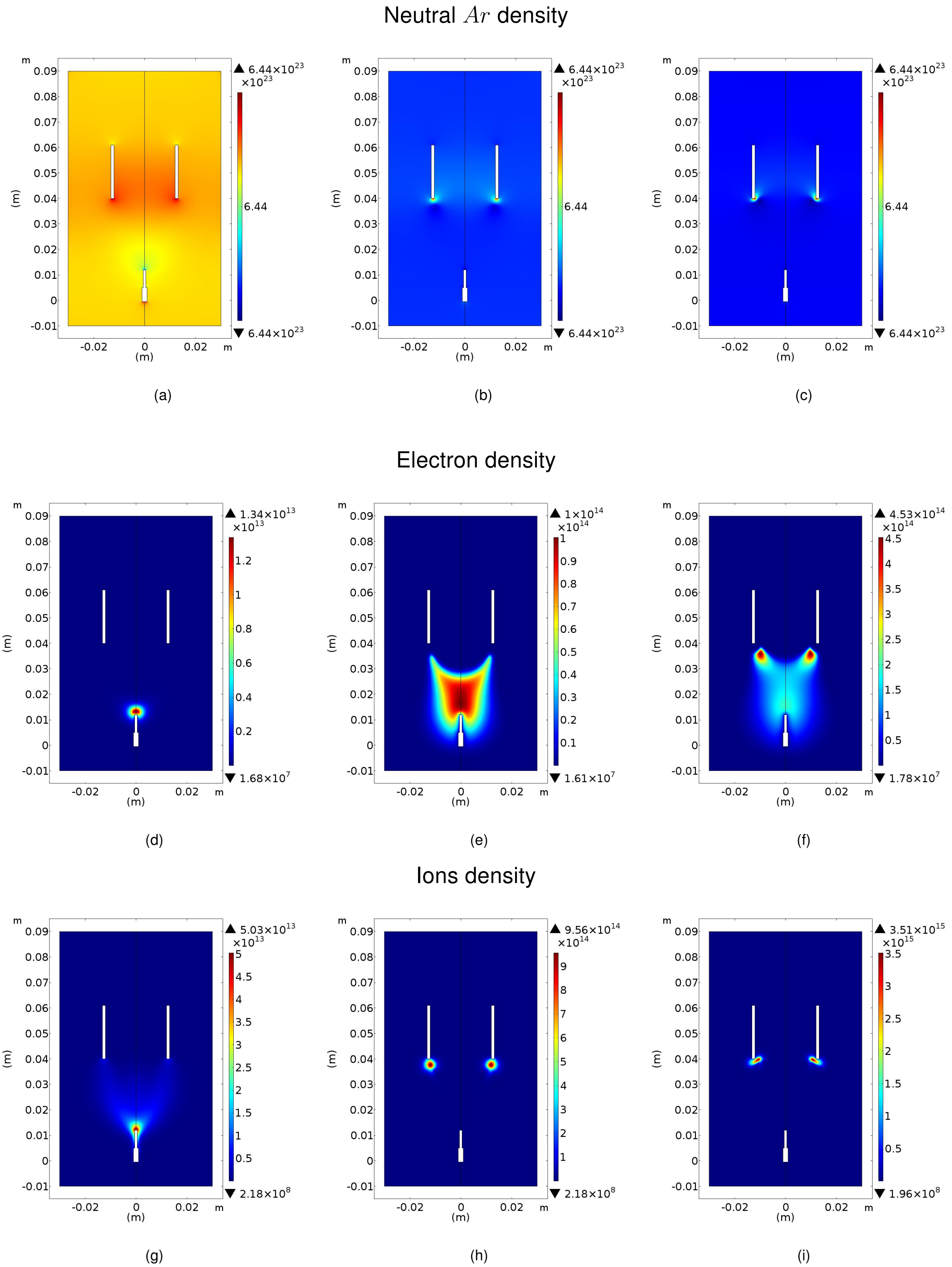
Neutral Ar density

(a) (b) (c)

Electron density

(d) (e) (f)

Ions density

(g) (h) (i)

Figure 5.7: Particle densities, in SI units m^{-3}, for a varying initial voltage of (a,d,g) 0.9kV, (b,e,h) 9kV and (c,f,i) 20kV. First row are shows the Ar neutral density, the second row presents the e^- density and the third row shows the Ar^+ ion density.

Influence of the cathode's geometry

After assessing that the geometry was not the best one, we decided to study the influence of the cathode's intrinsic geometry so we could optimize the cylindrical cathode. We started by changing the cathode's inner radius, r_i, but maintaining its thickness, 1.2mm, later we studied the influence of the cathode's length, l_c, in the thruster's behaviour.

Variation of the cathode's inner radius

To conduct the respective study we set both the applied voltage and the ballast resistor at constant values. Then, we varied the inner radius from $[10 - 16]$mm, as it can be observed in table (5.5).

Table 5.5: Simulation parameters used to observed the influence of the hollow cathode inner radius, r_i, in the single stage argon EHD thruster by varying the ballast resistor.

Parameter	Value
Applied Voltage	20kV
Ballast Resistor	500MΩ
Inner radius	$[10 - 16]$mm
γ_i	0.05
η	2.23×10^{-5}Pa.s

Figure (5.8) displays how the morphology of the electric potential distribution changes as the inner radius increases. When the inner radius is 10mm, the cathode is so narrow that the high potential plateau extends to regions outside the cathode. Simultaneously, inside the cathode, the electric potential has a poorer distribution when comparing to wider inner radius.

Although at 16mm, the electric potential distribution shows a great profile, since there is a more wide area in a two dimensional view, where the particles can be accelerated inside the cathode, it is at 12mm that the electric field is more intense. So it is possible to deduce that to deliver the best thruster profile, the geometry must be able to optimize both the electric potential distribution and the electric field.

As we expected, the variation of the inner radius has a great influence on both charged and neutral particles distributed along the simulation domain. In figure (5.10) we have a collection of pictures that show this influence. When the cathode is narrow, the electrons and ions have their respective maximum values near the cathode but a considerable proportion resides outside the cathode, which is not a favourable situation since we are losing particles that could be used in transferring momentum to neutral particles, leading to a increase of the fluid velocity.

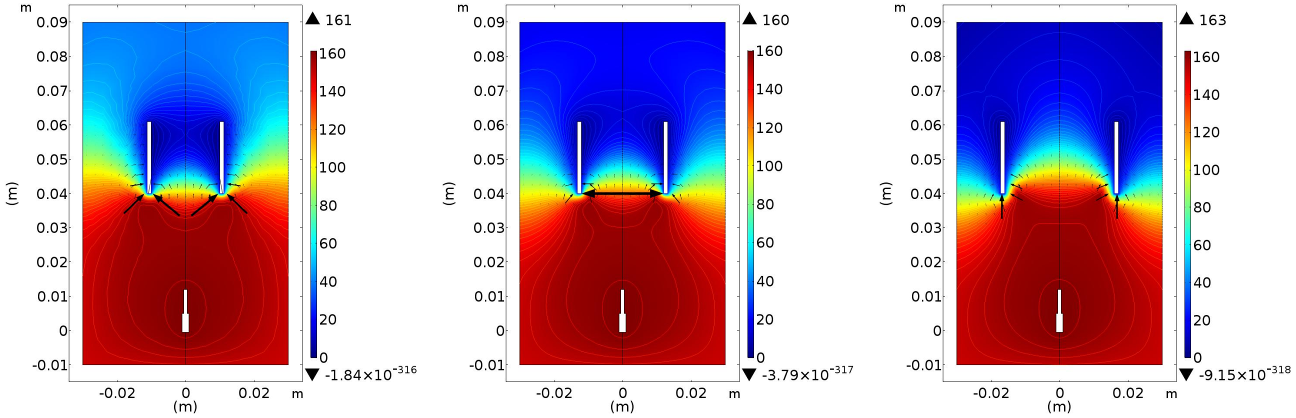

(a) (b) (c)

Figure 5.8: Electric potential distribution V for different inner radius. (a) 10mm, (b) 12mm, (c) 16mm.

We see an optimization on how the charged particles spatially scatter along the domain. Although wider ground electrodes distribute the charged particles in a more desirable profile, we found out that they decreased the maximum concentration value for both ions and electrons which is not favourable, as it was stated before.

From *Bernoulli*'s principle, an incompressible fluid flows as higher speeds when the cross-section area is small and lower speeds at higher cross-section areas Munson et al. (2005)). So in theory, narrow cathodes would produce higher velocity profiles. However larger cathodes allow more particles to flow inside them increasing the net thrust.

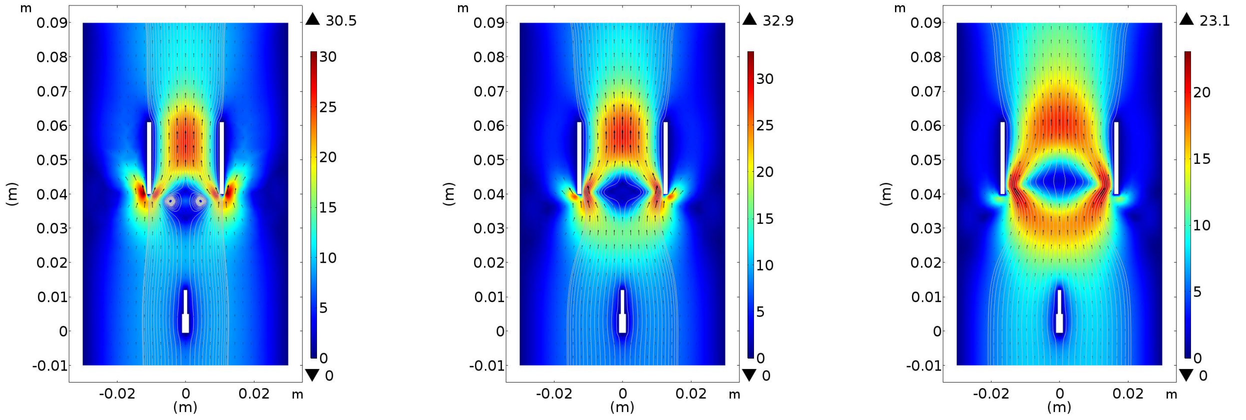

(a) (b) (c)

Figure 5.9: Two dimensional plasma fluid's velocity profile cm $\cdot$ s^{-1} for different inner radius. (a) 10mm, (b) 12mm, (c) 16mm.

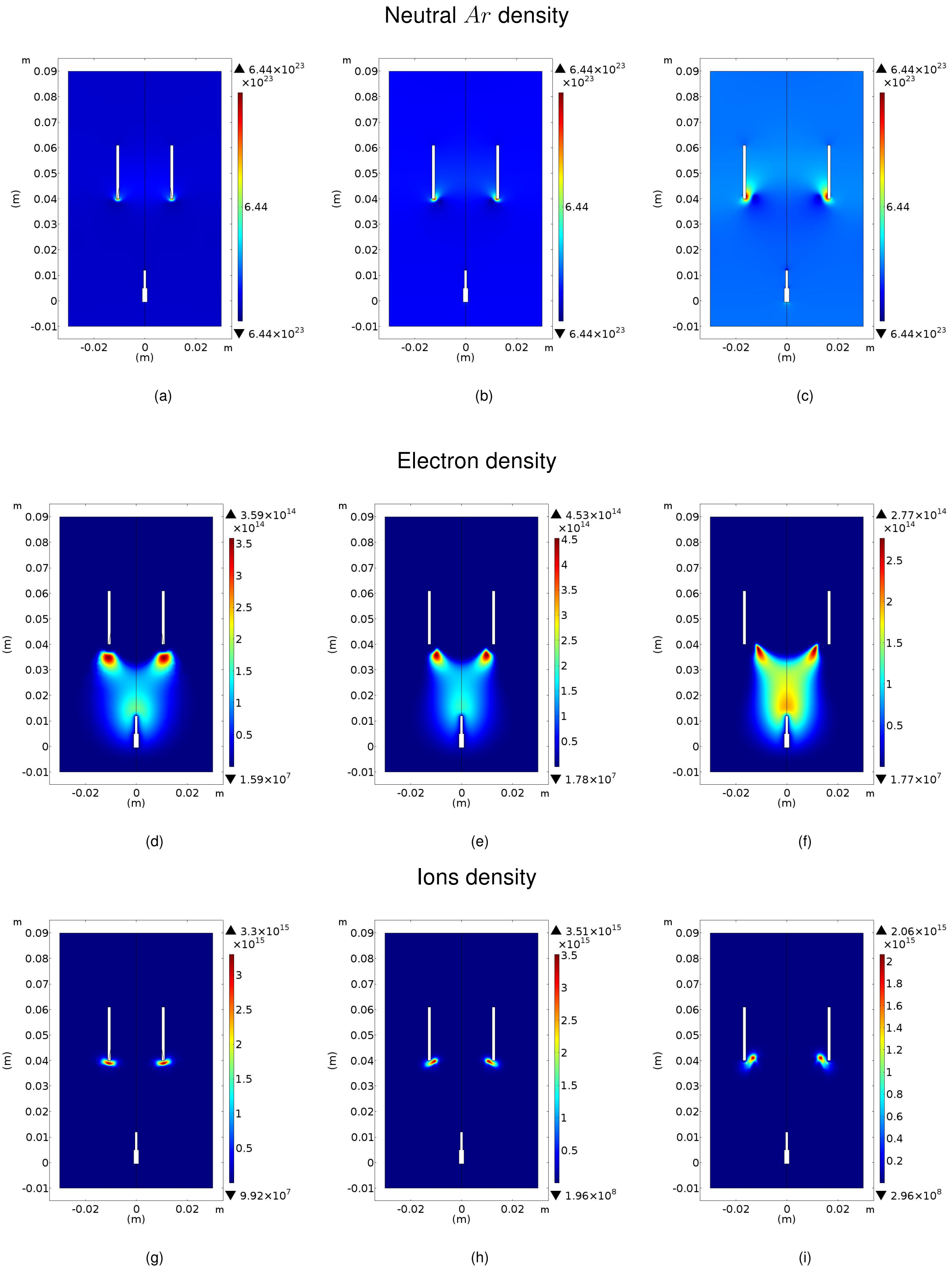

(a) (b) (c)

(d) (e) (f)

(g) (h) (i)

Figure 5.10: Particle densities, in SI units m^{-3}, for a varying cylindrical cathode's inner radius, r_i, of (a,d,g) 10mm, (b,e,h) 12mm and (c,f,i) 16mm. First row are shows the Ar neutral density, the second row presents the e^- density and the third row shows the Ar^+ ion density.

The incompressible fluid behaviour is observed in the results of the main velocity profile gas at two dimensions, depicted in figure (5.9). When the inner radius is 12mm or below, the plasma reaches speeds above the 30cm $\cdot$ s^{-1}, however we discovered that a narrower cathode would produce vortices in the stationary region. This dynamic phenomenon appears due to the simulation grid which amplifies numeric instabilities. At wider cathodes, the velocity decreases, reaching only 23cm $\cdot$ s^{-1} with an inner radius of 16mm. The optimal velocity is found with a radius of 12mm, with a maximum velocity of 33cm $\cdot$ s^{-1}.

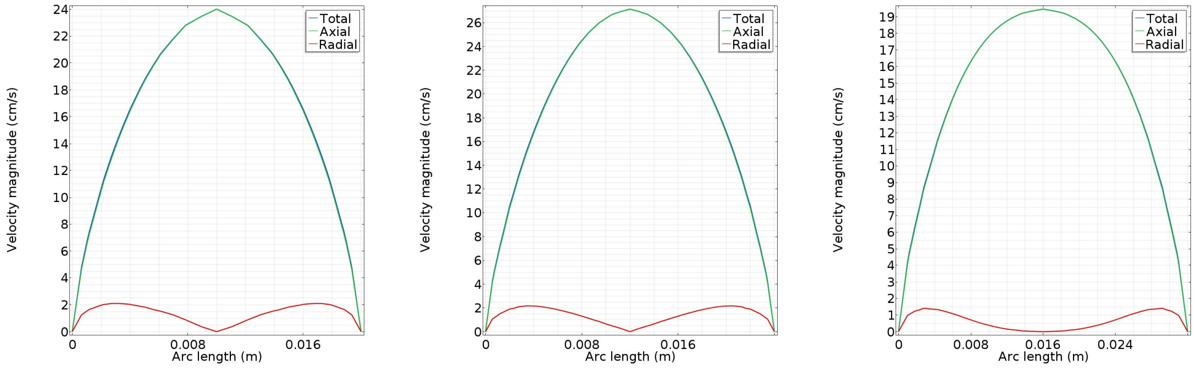

(a) (b) (c)

Figure 5.11: Expelled plasma fluid's velocity cm $\cdot$ s^{-1} for different inner radius at the exit of the cathode. (a) 10mm, (b) 12mm, (c) 16mm.

As it was expected the axial component of the fluid velocity at the cathode's exit points out that the narrower cathode is not a favourable situation, because the quadratic profile reaches a maximum below the 23cm $\cdot$ s^{-1} in contrast to velocity peak above the 27cm $\cdot$ s^{-1}, produced by the cathode with an inner radius of 12mm. For wider cathodes, the maximum velocity only reached 19cm $\cdot$ s^{-1}.

In terms of output thrust we found out that it remains approximately the same either when the inner radius is 12mm, 14mm and 16mm with values in the range of the 550nN. At $r_i = 10$mm, the thruster would only delivered 290nN, nearly half. The thrust-to-power ratio has a similar behaviour, since we are modulating the same plasma, the power spent to produce it is the same, reaching values of 86mN$/$kW. For the narrower cathode the value was 47mN$/$kW, a two times decreased.

Variation of the cathode's length

After observing the influence of the hollow cathode and its respective inner radius, we decided to study the influence of the cathode's length, not only regarding the thruster parameters but also regarding the applied voltage. The necessity to explore other voltages appeared during the investigation, when we came across different and interesting results. The parameters used in these studies are described in table (5.6).

Table 5.6: Simulation parameters used to observed the influence of hollow cathode length, l_c, in the single stage argon EHD thruster by varying the ballast resistor.

Parameter	Value
Applied Voltage	$[3-20]$kV
Ballast Resistor	$500\text{M}\Omega$
Cathode Length	$[8.4-21]$mm
γ_i	0.05
η	2.23×10^{-5}Pa.s

Due to the fact that we collected a great number of data and pictures, and since we study the influence of each applied voltage to each corresponding length, this thesis will only exploit the results referring to the case where the applied voltage was 20kV since it showed the best optimization.

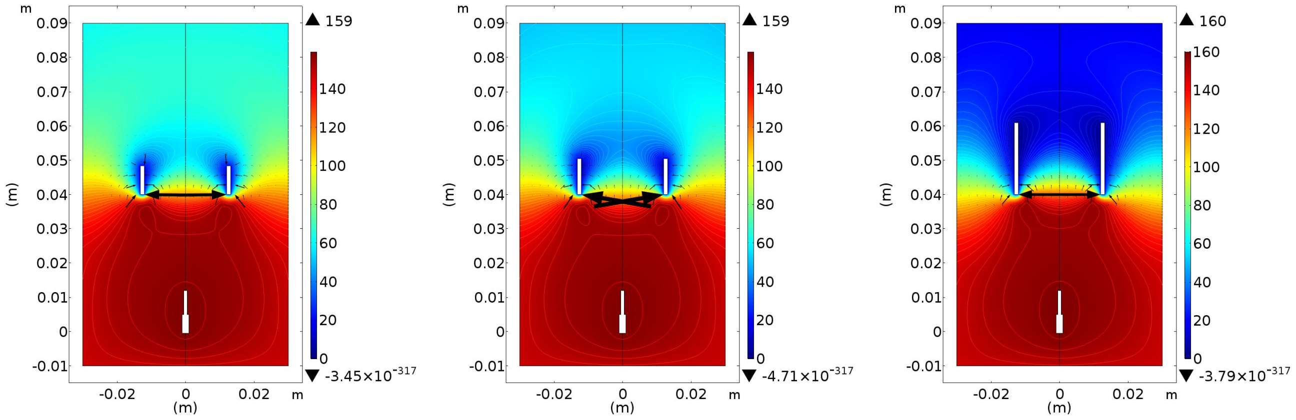

(a) (b) (c)

Figure 5.12: Electric potential distribution V for different cathode lengths, with an applied voltage of 20kV, (a) 8.4mm, (b) 10.5mm, (c) 21mm.

The electric potential distribution and its respective morphology is depicted in figure (5.12). There we observe an abrupt change in the electric potential distribution when the cathode's length is reduced. Inside the cathode and at lengths smaller then 11mm, we observed a predominance of axial components over the radial components of the electric field. The dimension of this acceleration matches the length of the cathode. We will see later that this phenomenon shows the best optimization results.

However these changes don't appear to affect how the charged or neutral particles scatter around the domain as it is demonstrated in figure (5.14). Second row displays the electron number distribution and for different cathode lengths it presents the same horse shoe profile, being the maximum values near the entry of the cathode. The same happens for ionized particles in the third row.

The plasma fluid's velocity shows, in general, a similar behaviour for all different lengths. At smaller cathode lengths, the middle entry region ceases to be stationary and the fluid gains some speed, with velocities reaching the 5cm $\cdot$ s^{-1}. Overall, the maximum speeds are found near the cathode's entry, with values from 33cm $\cdot$ s^{-1} when $l_c = 21$mm to 35cm $\cdot$ s^{-1} when $l_c = 8.4$mm, see figure (5.13).

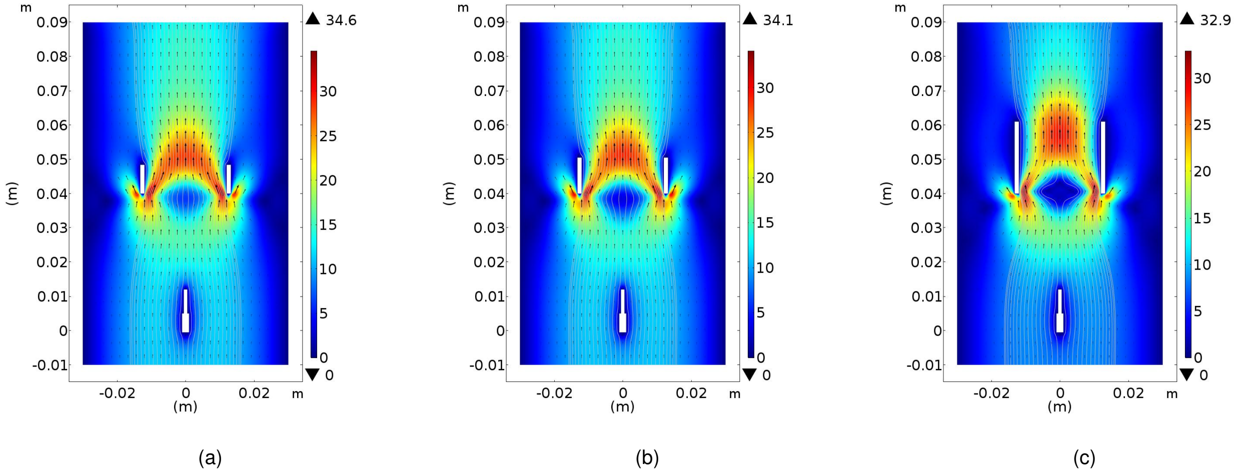

(a) (b) (c)

Figure 5.13: Two dimensional plasma fluid's velocity profile cm $\cdot$ s^{-1} for different cathode lengths with an applied voltage of 20kV. (a) 8.4mm, (b) 10.5mm, (c) 21mm.

As it as told before, the expelled velocity is computed at cathode's exit and since the cylindrical length was reduced, it is expected that this velocity will vary considerably. Figure (5.15) displays the velocity's value in which the plasma is expelled at the cathode according to the its length. We discovered that the quadratic profile changes its curvature, approximately keeping the same peak value under the 27cm $\cdot$ s^{-1} to 28cm $\cdot$ s^{-1}. Yet when the cathode was reduced to 40%, the radial components increased, reducing the total velocity, creating two peaks.

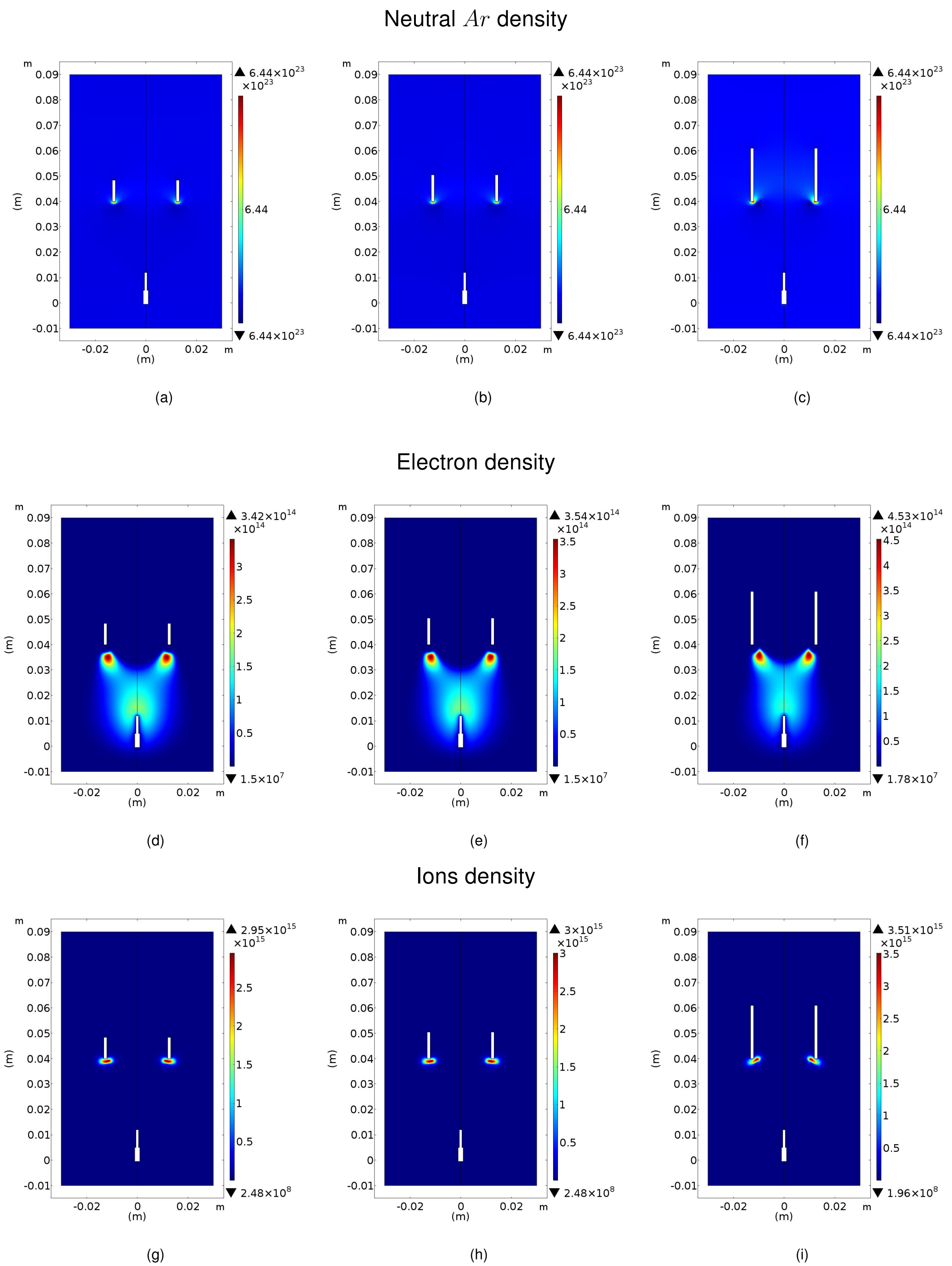

(a) (b) (c)

(d) (e) (f)

(g) (h) (i)

Figure 5.14: Particle densities, in SI units m^{-3}, for a varying cathode length, l_c, of (a,d,g) 8.4mm, (b,e,h) 10.5mm and (c,f,i) 21mm with an applied voltage of at 20kV. First row are shows the Ar neutral density, the second row presents the e^- density and the third row shows the Ar^+ ion density.

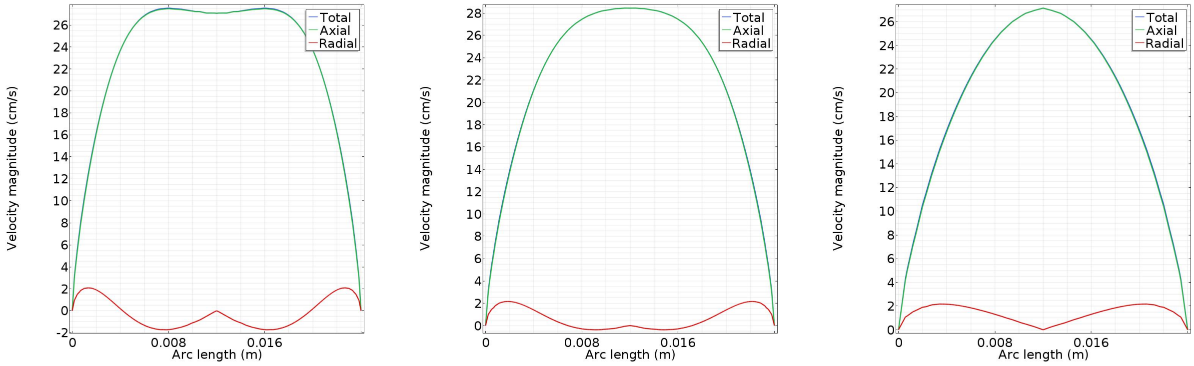

(a) (b) (c)

Figure 5.15: Expelled plasma fluid's velocity cm · s^{-1} for different cathode lengths with an applied voltage of 20kV. (a) 8.4mm, (b) 10.5mm, (c) 21mm.

This decrease in the cathode length traduces in a general increase of the output thrust, reaching values near the 1μN with an efficiency of 150mN$/$kW, the best value of T/P ratio so far. Comparing to the previous optimization, we improved the thruster parameters of the argon single stage EHD thruster around two hundred times in thrust and around 9 times in terms of its efficiency.

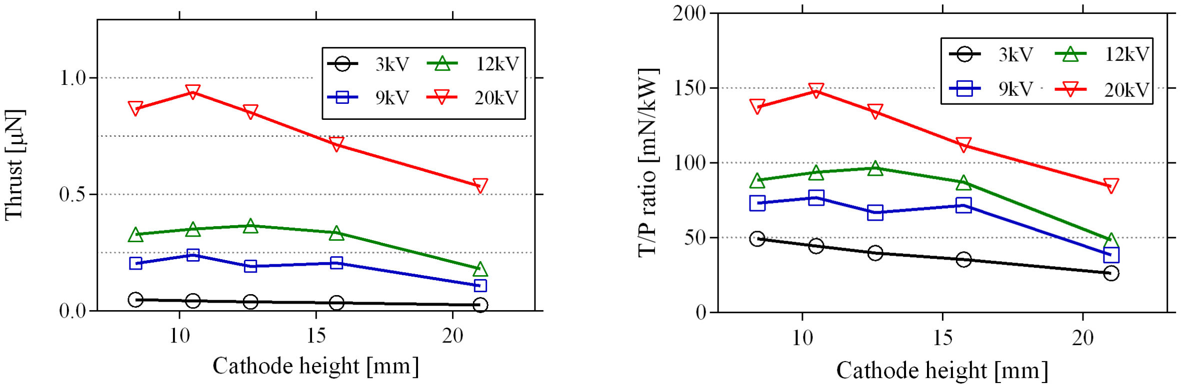

(a) (b)

Figure 5.16: Variation of thruster parameters according to cathode length to different applied voltages. (a) output thrust μN, (b) thrust-to-power ratio mN$/$kW.

We also discovered that the cathode's length is highly dependent of the applied voltage since we observed a distinct optimization profile for each potential difference. Take for instance the study at 12kV, the maximum thrust and thrust-to-power ratio are produced when at 60% of the initial geometry with values of 0.366μN and 97mN$/$kW, respectively. Meanwhile at lower voltages, the optimal length is found to be 50% for 9kV and 40% for 3kV.

Influence of the secondary electron emission coefficient

Another interesting parameter is the secondary electron emission coefficient or second *Towsend* discharge parameter,γ_i, which plays an important role in the geometry due to the electrodes not being parallel and having different sizes. The ionized particles are accelerate towards the cylindrical cathode and ions with enough energy collide with the material of this electrode, transferring the excess energy to the cathode's surface, which in return releases electrons. This phenomenon is usually called electron emission yield and as a great contribution in the total current density between the electrodes (Granados (2018)).

Table 5.7: Simulation parameters used to observed the influence of secondary electron emission coefficient, γ_i, in the single stage argon EHD thruster by varying applied voltage.

Parameter	Value
Applied Voltage	$[3-20]$kV
Ballast Resistor	$500\text{M}\Omega$
γ_i	$[10^{-4}-10^{-1}]$
η	2.23×10^{-5}Pa.s

Since, at this point, it was obvious that each initial voltage would affect considerably the plasma discharge, we decided to complete this study by simulating the thruster responses for each γ_i, according to each potential difference. The parameters used are described in table (5.7).

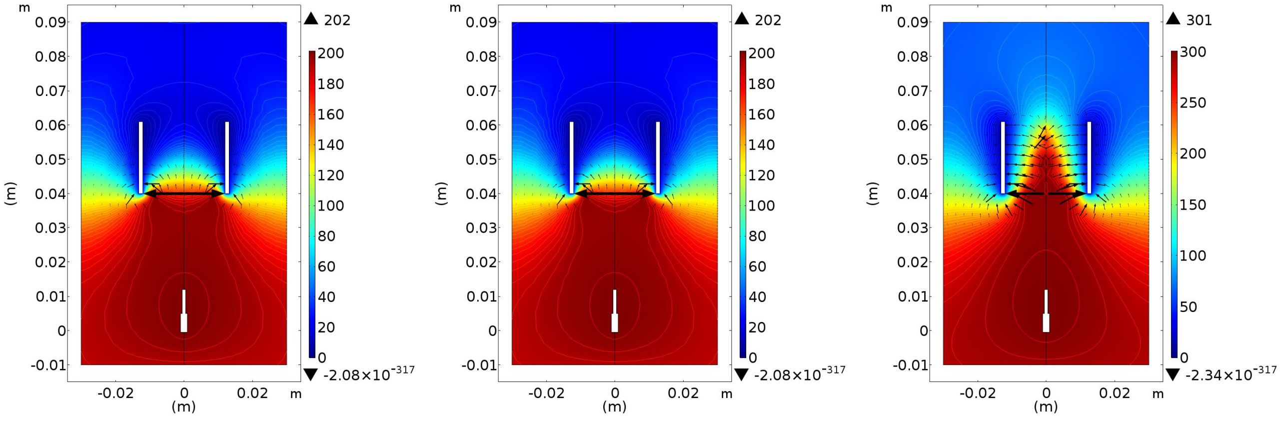

(a) (b) (c)

Figure 5.17: Electric potential distribution V, for different values of secondary electron emission coefficient, γ_i at an applied voltage of 20kV. (a) 0.02, (b) 0.01 and (c) 0.002.

We observed computationally that the secondary electrons play an important role in the modulation of a plasma. Figure (5.17) presents the behaviour of the electric potential distribution for various values of γ_i. For values under 10^{-2}, the previous horse shoe profile of the potential distribution changes drastically into a inverse cone profile, which changes also the morphology of the electric field lines. As it was said earlier, this profile is the one that produces the optimal results.

These changes traduced in different distributions of the particles involved inside the reactor chamber. For higher values, the plasma shows the same behaviour over the particles spatial distributions. Curiously, we discovered that at lower γ_i values, the electron density is highly concentrated near the cathode's exit, coincidentally in the region of lower electric potential, reaching values of 2.3×10^{20}m^{-3} whereas the positive ion particles reach concentrations of 4×10^{17}m^{-3} as we can observed in figure (5.21). This phenomena indicates that by reducing the secondary electron emission coefficient we increase locally the ionization degree to values near 10^{-6}, a two times increase.

As we were expecting, by increasing the ionization degree we reach fluid velocities far greater then we had before. Since a lower coefficient means less electrons being emitted from the cathode, then less electrons will participate in the charge neutralization within the plasma, allowing more ions to be accelerated to transfer more momentum into the neutral particles. This traduces in peak velocities in this region above 126cm $\cdot$ s^{-1}, that is velocities above 1m $\cdot$ s^{-1}.

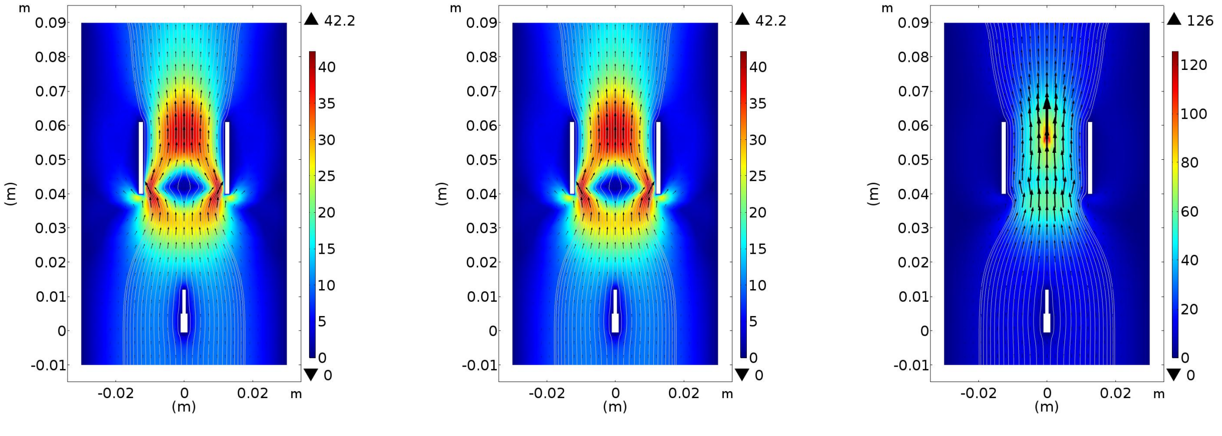

(a) (b) (c)

Figure 5.18: Two dimensional fluid velocity distribution, in SI units cm$\cdot$s^{-1}, for different values of secondary electron emission coefficient, γ_i at an applied voltage of 20kV. (a) 0.02, (b) 0.01 and (c) 0.002.

Figure (5.18) presents the main plasma velocity within the cathode chamber. As we can observe, the fluid shows a similar behaviour for higher values but when we reduce the γ_i coefficient, there is an increase in the minimum velocity, reaching the 40cm $\cdot$ s^{-1}. This value correspond to the highest velocity when we increase the secondary electron emission coefficients.

As the main gas velocity changes abruptly, so changes the exhaust velocity. We can observed that the quadratic profile we found for higher γ_i values is changed into a pyramidal profile, where peak exhaust velocities increased from 38cm $\cdot$ s^{-1} into near 76cm $\cdot$ s^{-1}.

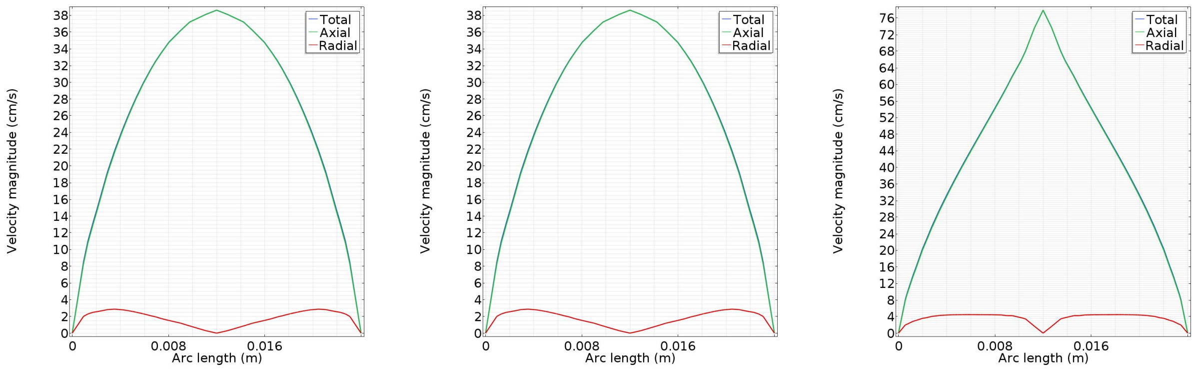

(a) (b) (c)

Figure 5.19: Fluid velocity components at cathode's exit, in SI units cm $\cdot$ s^{-1}, for different values of secondary electron emission coefficient, γ_i at an applied voltage of 20kV. (a) 0.02, (b) 0.01 and (c) 0.002.

To better comprehend the influence of this discharge parameter, we present the thruster parameters for each applied voltage. As it was expected, the plasma velocity changed drastically, mainly due to electric field strength, which means that there are less secondary electrons being emitted from the cathode. As it was stated earlier, less secondary electrons means that the neutralization of the gas occurs at a slower pace, allowing a better acceleration. The output thrust reaches values near the 2.5μN with an efficiency of near 200mN/kW for an applied voltage of 20kV. Yet for lower voltages, the thruster behaves very differently, for instance, at 3kV, we see an optimal value for the thruster efficiency, above 100mN/kW, when $\gamma_i = 0.001$.

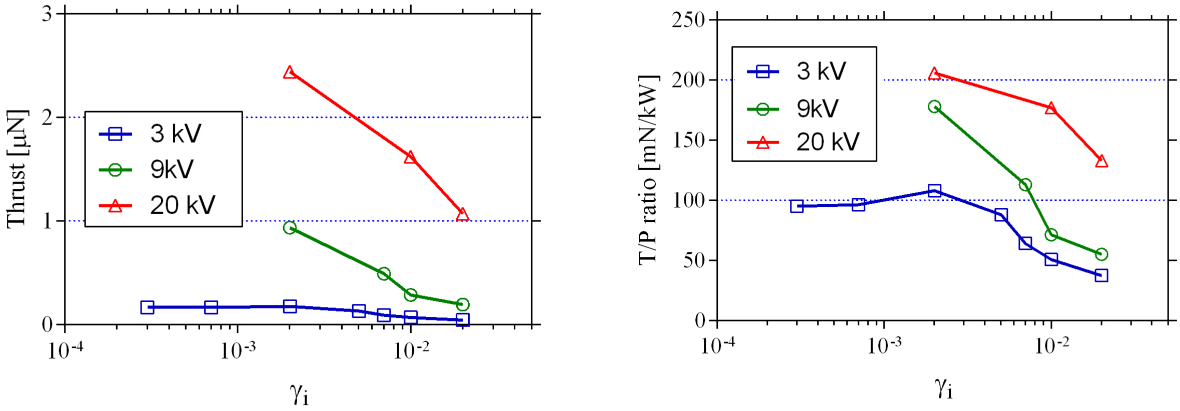

(a) (b)

Figure 5.20: Variation of thruster parameters for different values of secondary electron emission coefficient, γ_i at an applied voltage of 20kV. (a) output thrust μN, (b) thrust-to-power ratio mN/kW.

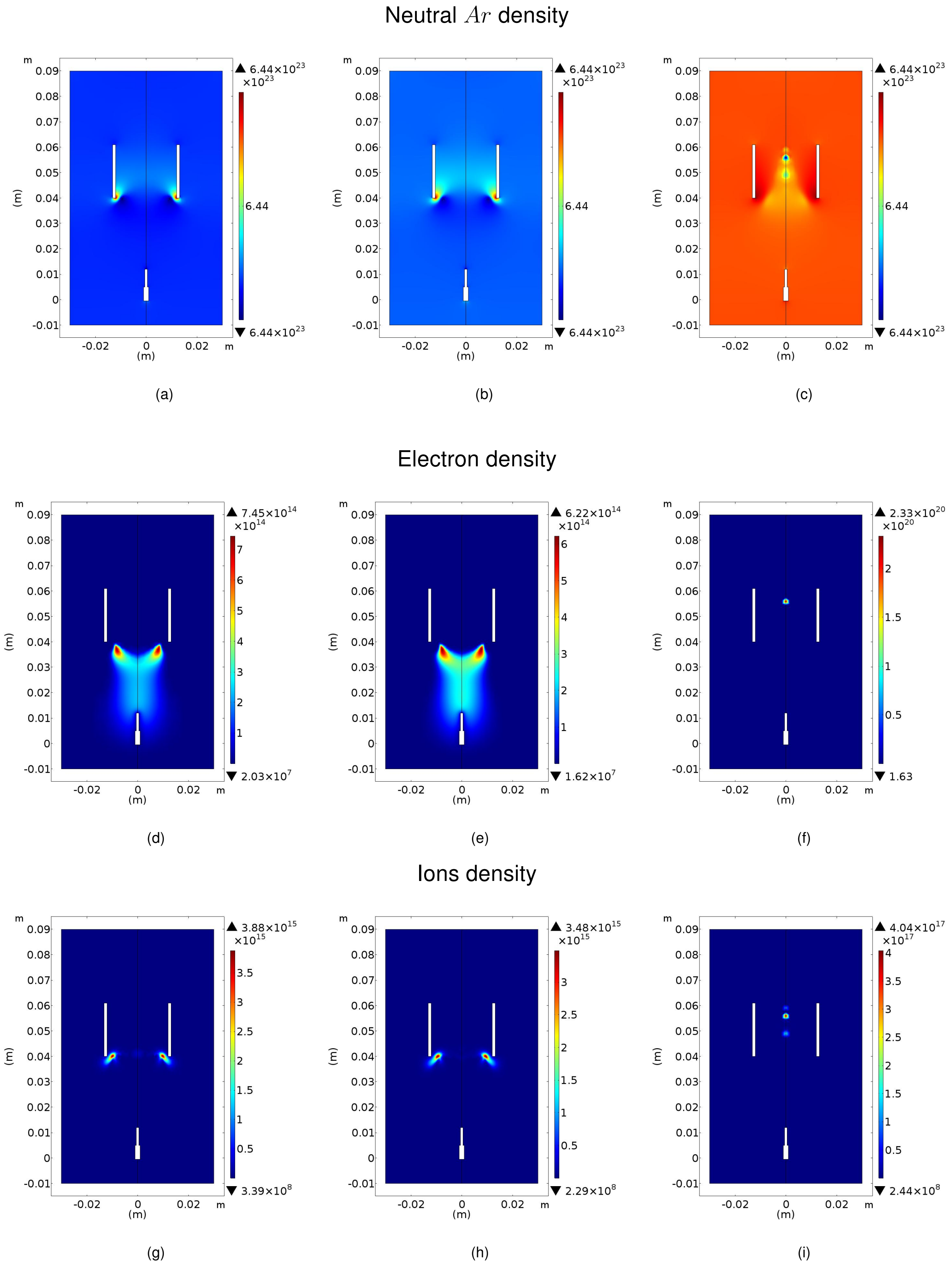

(a) (b) (c)

(d) (e) (f)

(g) (h) (i)

Figure 5.21: Particle densities, in SI units m^{-3}, at an applied voltage of 20kV for different values of secondary electron emission coefficient, γ_i. (a,d,g) 0.02, (b,e,h) 0.01 and (c,f,i) 0.002. First row are shows the Ar neutral density, the second row presents the e^- density and the third row shows the Ar^+ ion density.

After consulting the experimental value for the γ_i for a discharge with an initial voltage of 20kV, which is approximately 0.001, see table (3.3), we modulated the thruster in its optimized cathode length, that is, for a length of 10.5mm. The results show a great optimization since the argon propellant EHD thruster developed a thrust of 2.75μN and thrust-to-power ratio of 295mN/kW.

5.2 ARGON PLASMA-SLIDING THRUSTER

After establishing that the electric potential distribution plays an important role in the optimization of the EHD thruster, we decided to introduce a dielectric material slab underneath the hollow cathode, by taking into account the sliding effect of the electric field on a dielectric surface (Shvydky et al. (2004)). In this simulation, we used a quartz glass material with a refractive index of $n = 1.5$ with a length of 23.1mm and a thickness of 0.1mm. However, after several simulation attempts we found out that we should construct a dielectric ramp that connects both dielectric slab and the copper cathode.

Influence of the aperture angle

First we started by discovering the best aperture angle. In order to do that, we evaluated the thruster's parameters under several angles. The propellant gas utilized was argon and the applied voltage between the anode and the cathode was 3kV, the ballast resistor in $500\text{M}\Omega$, the blocking capacitor of 1pF and the secondary electron emission coefficient of 0.05. The size of the cathode was maintained at 21mm.

We found out that with an increase of the aperture angle the morphology of the electric field lines and the electrical potential inside the cathode change considerably, as we can see in figure (5.22). We also observed that for larger angles, the sliding effect of the electric field was accentuated, where we could see the electric field lines slip across the dielectric surface.

These considerable changes produce a great impact in how both charged and non-charged particles scatter around the simulation domain. In a first glance, we observed that just the presence of a dielectric slab created different particle distribution profiles (see figure (5.26)). Take for instance the electron density, with the increase of the aperture angle, electrons start to concentrate near the cathode, and the ion particles change from near cathode profile to get concentrated where the electrons are. In terms of concentration peaks, we also observed that the ionization degree also increases, from 10^{-9} to 10^{-7}. As will be seen later, this means that the thrust and efficiency also increased.

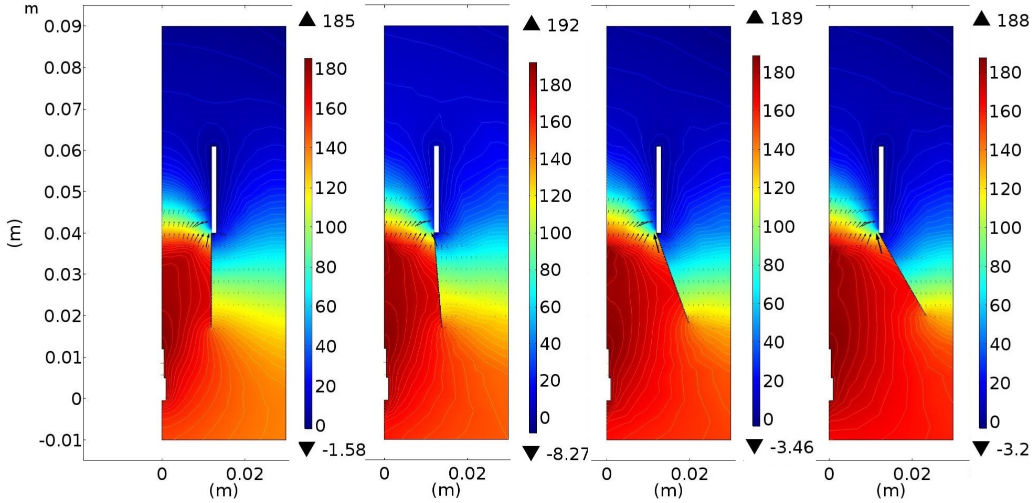

Figure 5.22: Electric potential distribution V, for different sliding slab's aperture angle, from the left to the right, $0°$, $10°$, $20°$ and $30°$.

The plasma's main velocity, as we were expecting, increased with the aperture angle as well. We can see in figure (5.23) for the same plasma conditions, discharge current and γ_i, not only the maximum fluid velocity increased up to 14cm $\cdot$ s^{-1} but also the stationary region at the cathode's entry ceases to exit, becoming an acceleration region, with a minimum velocity of 6cm $\cdot$ s^{-1}.

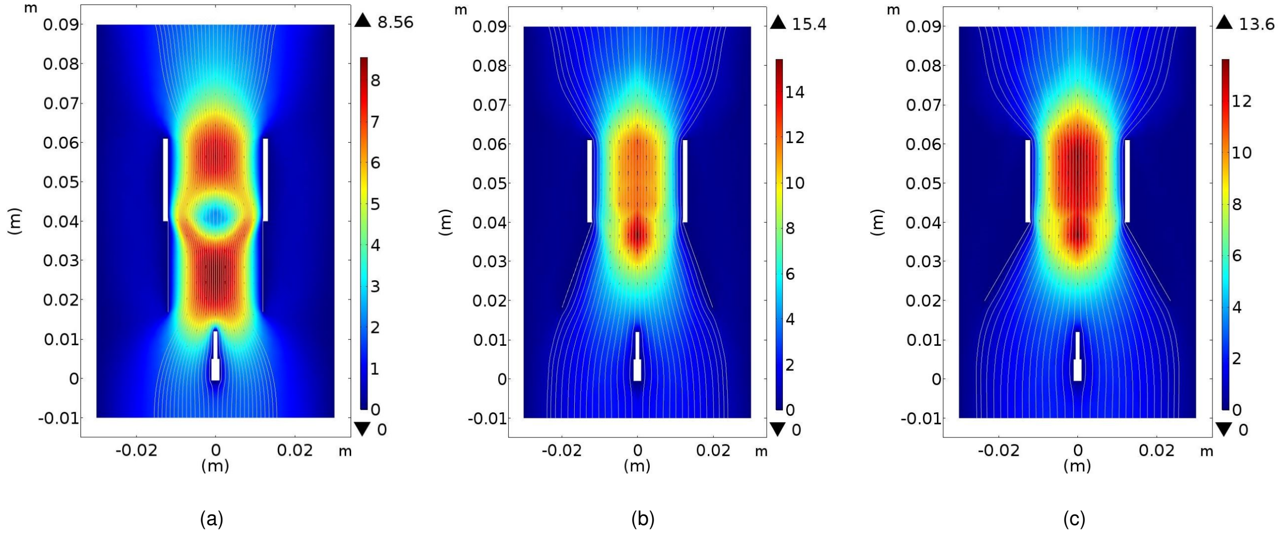

(a) (b) (c)

Figure 5.23: Two dimensional fluid velocity distribution, in SI units cm $\cdot$ s^{-1}, for different aperture angles. (a) $0°$, (b) $20°$ and (c) $30°$.

In comparison to the argon EHD thruster without the dielectric slab, the two dimensional fluid velocity profile is completely different since we do not see fluid flow from outside of the cathode as the dielectric slab helps confine and reduce the plasma's particles as we saw earlier. As for the expelled fluid, just the presence of the dielectric slab increases the expelled velocity from $6\text{cm}\cdot\text{s}^{-1}$ to up $8\text{cm}\cdot\text{s}^{-1}$. With the increase of the aperture angle, this variation changes up to $12\text{cm}\cdot\text{s}^{-1}$, practically a two times increase.

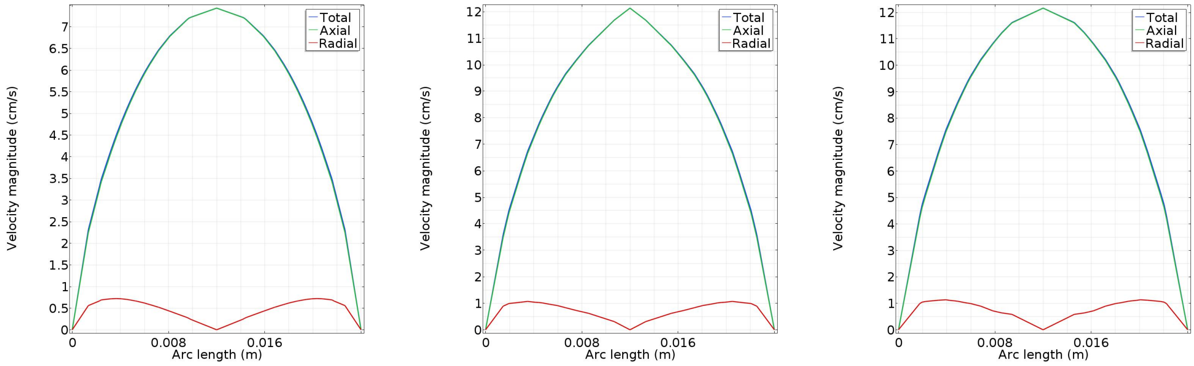

(a) (b) (c)

Figure 5.24: Fluid velocity components at cathode's exit, in SI units $\text{cm}\cdot\text{s}^{-1}$, for different aperture angles. (a) $0°$, (b) $20°$ and (c) $30°$.

In the meantime, the plasma sliding thruster produces better thruster parameters than the argon single stage thruster. Here we see that for $0°$ the thrust reaches almost 41.39nN, and a thrust-to-power ratio of 39.67mN/kW almost a 1.6 times increase with the same plasma without the dielectric slab ($T = 25.86$nN and T/P ratio $= 26.27$mN/kW). We see that when the angle increases, the thruster produces its best results, reaching an output thrust of 106.65nN and an efficiency of 101.11mN/kWfor $30°$ angle. In figure (5.25) we see the influence of these parameters due to each aperture angle, there is possible to observe that for higher degrees, the increase tendency tends to slow down, reaching an optimal angle.

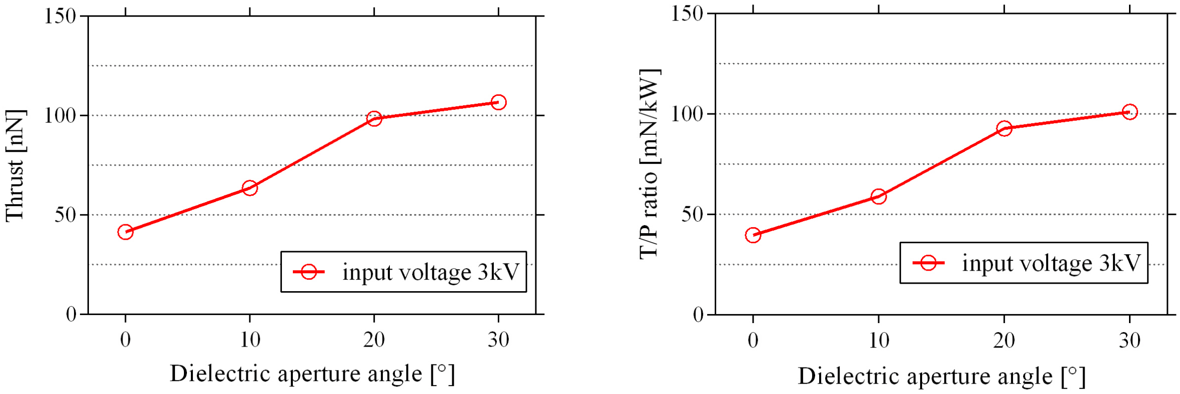

(a) (b)

Figure 5.25: Variation of thruster parameters for different dielectric slab's aperture angles with a constant applied voltage of 3kV. (a) output thrust μN, (b) thrust-to-power ratio mN/kW.

Neutral Ar density

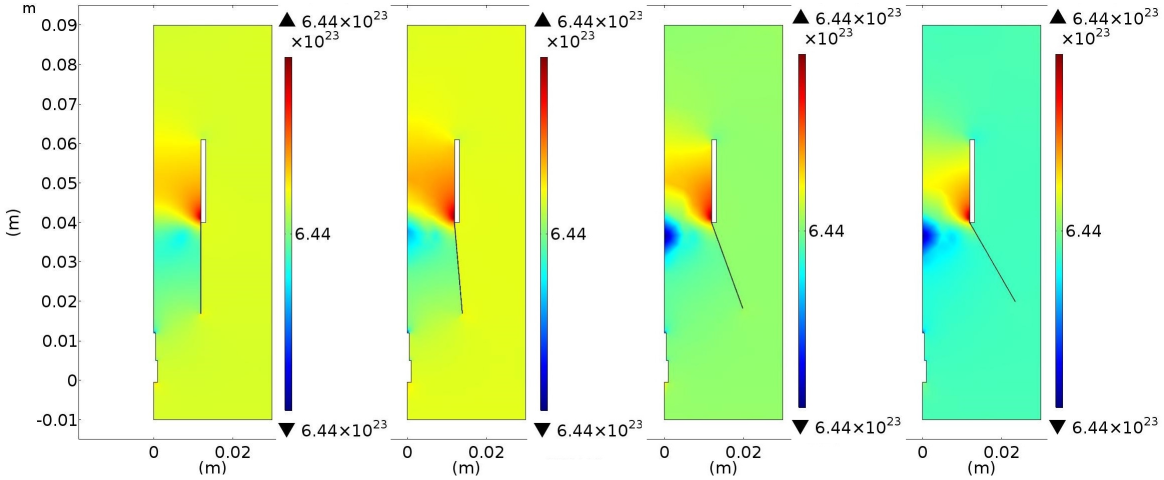

Electron density

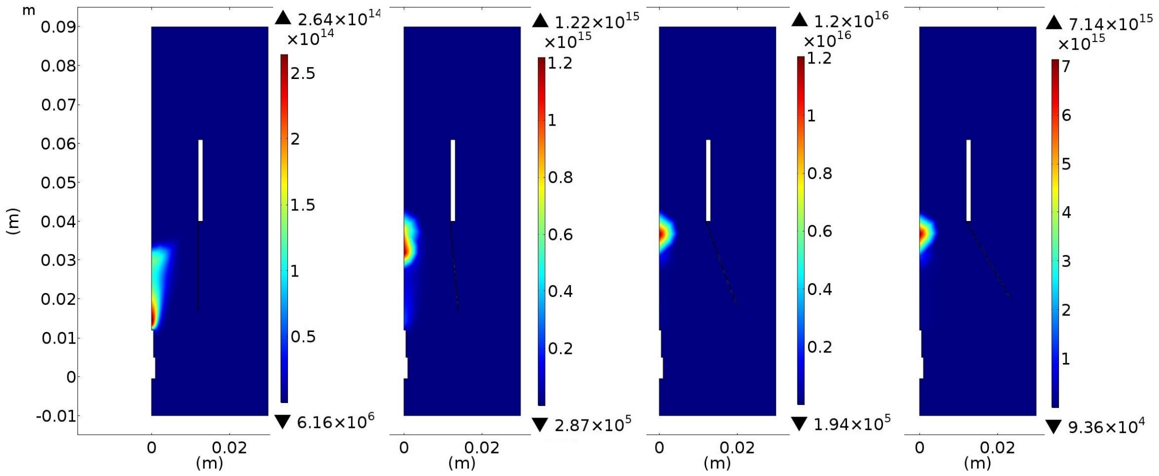

Ion density

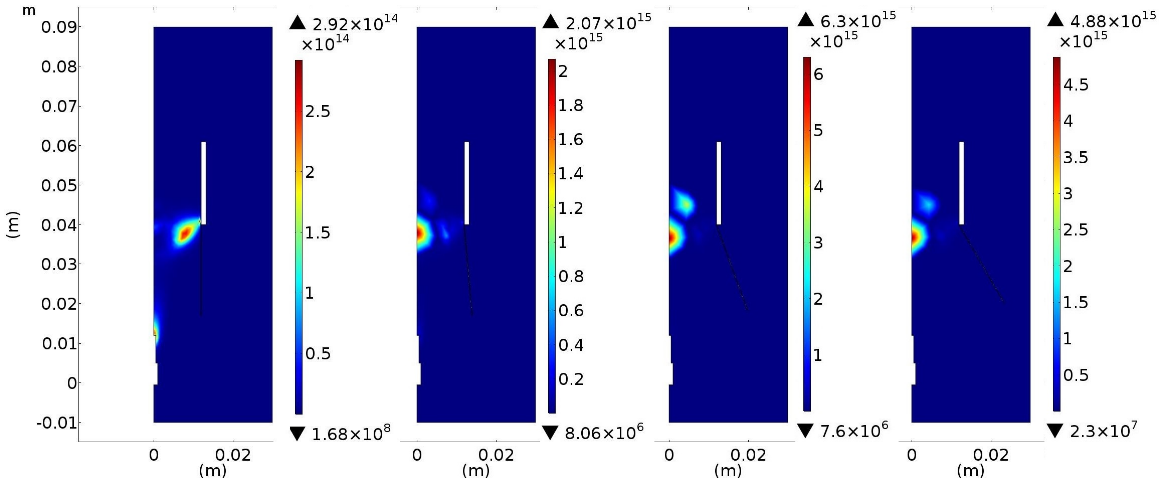

Figure 5.26: Particles distribution m^{-3}, for different sliding slab's aperture angle, from the left to the right, 0°, 10°, 20° and 30°. The first row are represented the neutral Ar atoms, the second row are represented the electrons and in the third row are represented the Ar^{+} ions.

Optimization of the cathode's length

The second part of this study consisted in changing both the applied voltage and the cathode's length, maintaining the values of the ballast resistor in $500\text{M}\Omega$, blocking capacitor of 1pF and secondary electron emission coefficient of 0.05. The dielectric slab was fixed with an aperture angle of $30°$. Although the simulation was performed for several different voltages, we will present the results regarding one specific case, more precisely, when $V_0 = 9$kV since as we will see later, it was the one with better thruster parameters.

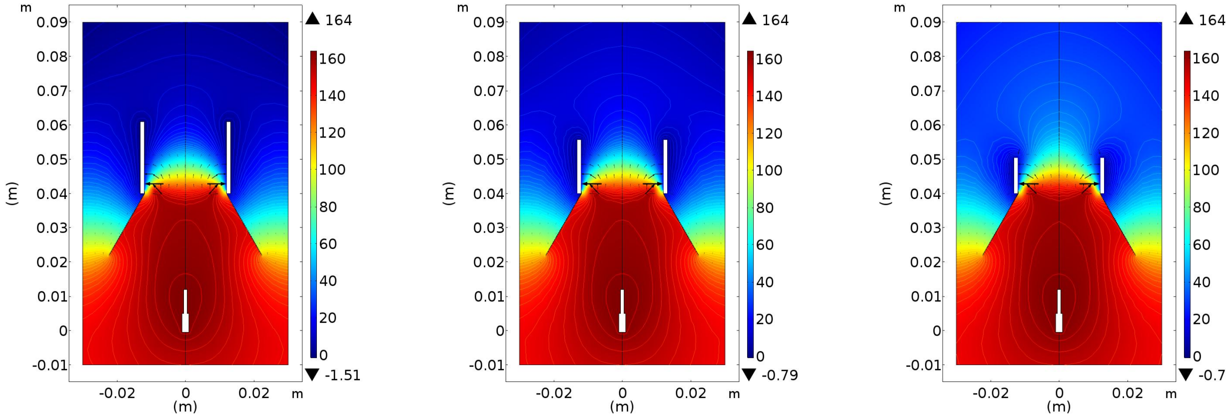

(a) (b) (c)

Figure 5.27: Electric potential distribution V of a plasma-sliding thruster for an initial applied voltage of 9kV for different cathode's lengths. (a) 21mm, (b) 15.8mm, (c) 10.5mm.

Starting analysing the electric potential distribution, it is possible to assess that the morphology of the electric field lines do not change, maintaining approximately the same intensity and behaviour. However for the half sized cathode, we observed a little propagation of the electric potential due to the shortened electrode ground.

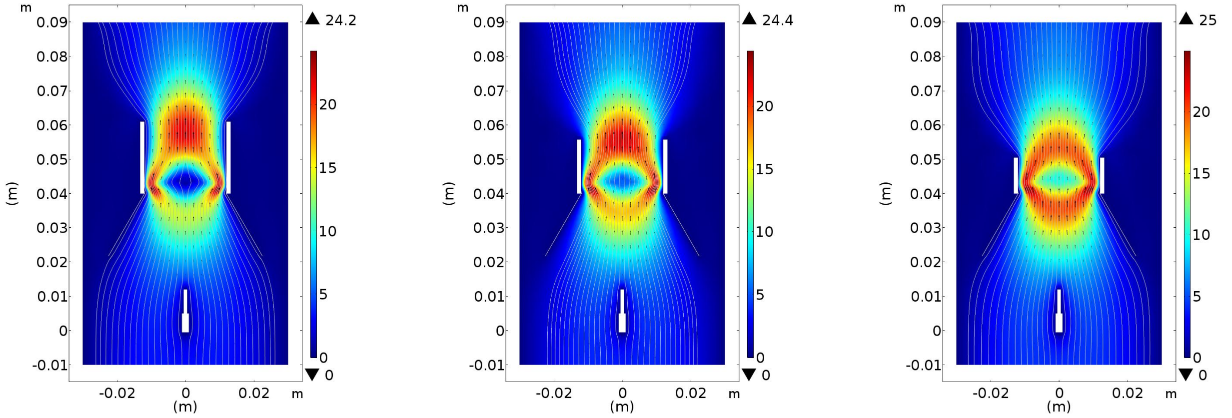

(a) (b) (c)

Figure 5.28: Two dimensional fluid velocity distribution cm · s^{-1}, of a plasma-sliding thruster for an initial applied voltage of 9kV for different cathode's lengths. (a) 21mm, (b) 15.8mm, (c) 10.5mm.

In terms of particle distributions, as it is depicted in figure (5.30), we can perceive that all the particles, both charged and non-charged, do not tend to scatter, instead they maintain the same distribution profile whenever the cathode's length is varying or not. We could also notice that in comparison to the non sliding thruster, the ionization degree is higher, reaching local values of $\approx 10^{-8}$.

Since there wasn't a considerable change in the particles distribution we do not expect a considerable modification in the plasma main velocity. Figure (5.28) displays that assumption well. Although the stationary region in the entry of the cathode ceases to exist for small lengths, we observed that the peak velocity do not varies so much, keeping the same speed ranges at $24 - 25$cm $\cdot$ s^{-1}. From this profiles we can also predict that the linear velocity profile at the cathode's exit will suffer a drastic change.

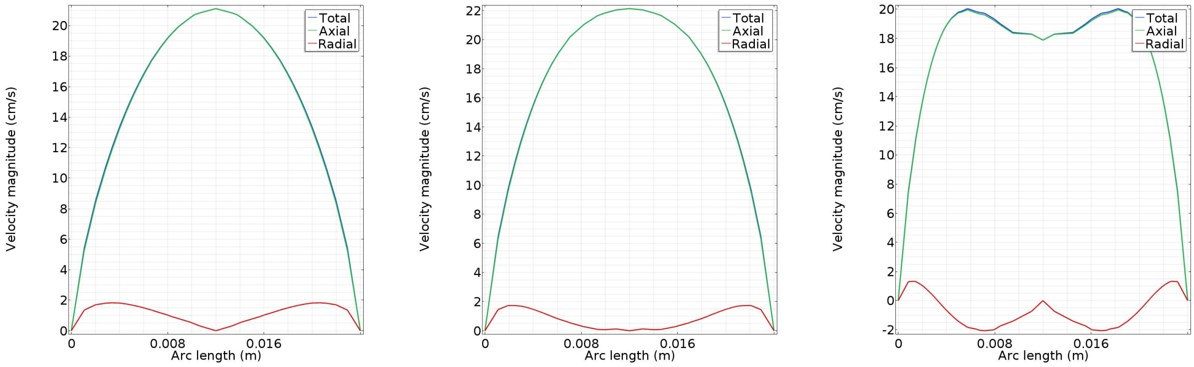

(a) (b) (c)

Figure 5.29: Fluid velocity components at cathode's exit cm $\cdot$ s^{-1}, of a plasma-sliding thruster for an initial applied voltage of 9kV for different cathode's lengths. (a) 21mm, (b) 15.8mm, (c) 10.5mm.

In figure (5.29) we observe that the cathode's exit velocity reaches a maximum value near 22cm $\cdot$ s^{-1} when the cathode has length of 15.8mm, 75% of the length of the previous developed thruster's cathode. For the half sized cathode, the quadratic profile ceases to exit, since in the middle region of the cathode, the velocity drops to around 2cm $\cdot$ s^{-1}.

The plasma-sliding thruster parameters, thrust and thrust-to-power ratio, are plotted in figure (5.31). In there we can assess that a dielectric slab affects considerably the EHD thruster since its presence doesn't allow high applied voltages. The simulations did not converge when we set the initial voltage at $V_0 = 20$kV and not all cases converge when $V_0 = 12$kV. Also at this last voltage, the output thrust was in the same order as the cases where $V_0 = 9$kV but in terms of its efficiency, this case gave worst results.

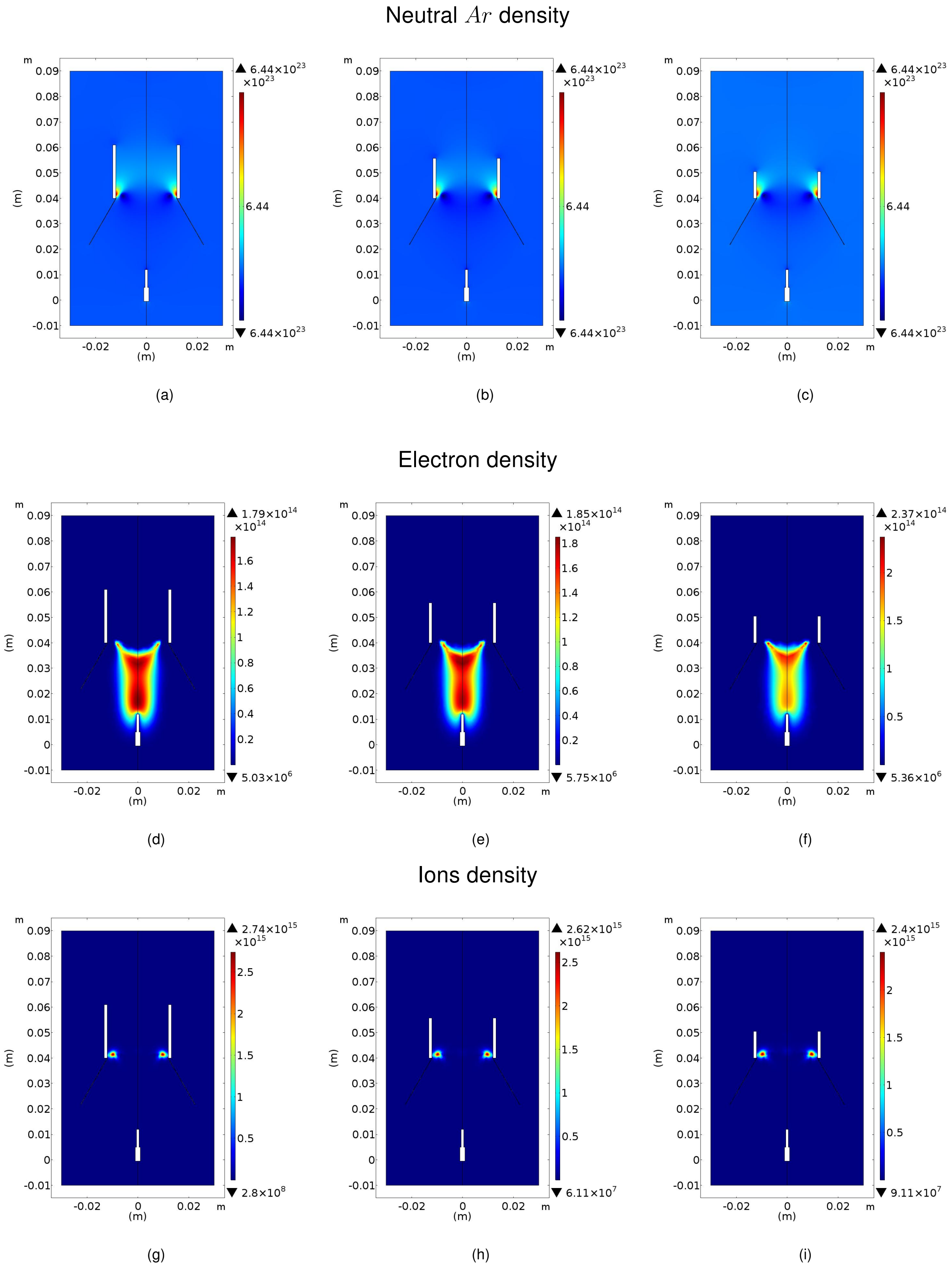

(a) (b) (c)

(d) (e) (f)

(g) (h) (i)

Figure 5.30: Particle densities, in SI units m^{-3}, for an initial applied voltage of 9kV for different cathode's lengths. (a,d,g) 21mm, (b,e,h) 15.8mm and (c,f,i) 10.5mm. First row are shows the Ar neutral density, the second row presents the e^{-} density and the third row shows the Ar^{+} ion density.

Overall, in comparison to non sliding argon thruster, we increased the net thrust from 43nN and 240nN up to 127nN and 500nN for the half sized cathode with applied voltages of 3kV and 9kV, respectively. The thruster's efficiency also increased as well, reaching values of 45mN/kW and 77mN/kW up to 120mN/kW and 173mN/kW for the same cases.

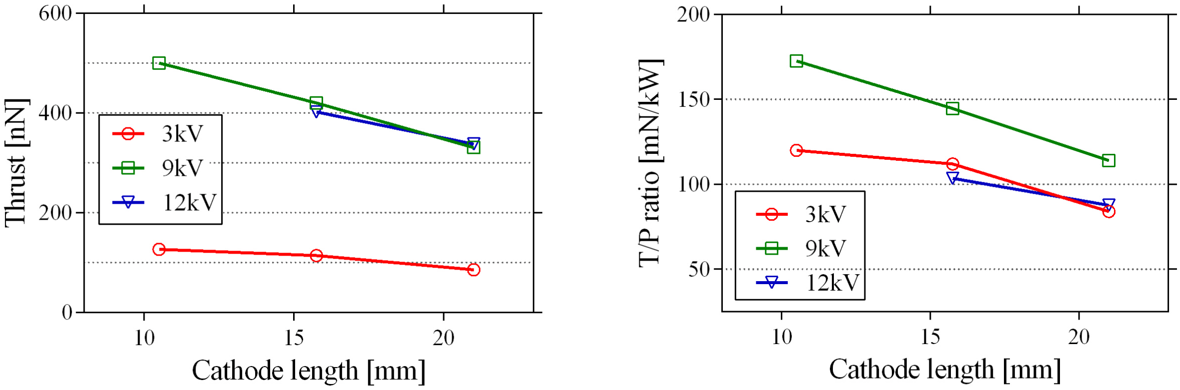

(a) (b)

Figure 5.31: Variation of plasma-sliding thruster parameters for different cathode's lengths and applied voltages (a) output thrust μN, (b) thrust-to-power ratio mN$/$kW.

Influence of the the secondary electron emission coefficient

The final part of the plasma-sliding thruster study consisted in changing both the applied voltage, cathode's length, and secondary electron emission coefficient. For consistency terms we maintained the values of the ballast resistor in $500\text{M}\Omega$, blocking capacitor of 1pF and dielectric slab was fixed at $30°$ aperture angle as well.

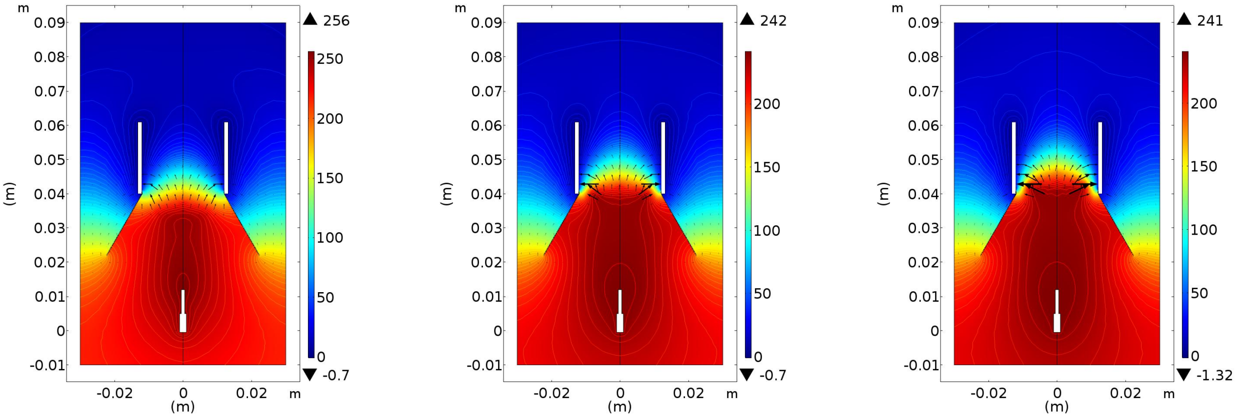

(a) (b) (c)

Figure 5.32: Electric potential distribution V of a plasma-sliding thruster with a secondary electron emission coefficient of 0.009 and cathode's length of $l_c = 21$mm for different applied voltages. (a) 3kV, (b) 9kV, (c) 12kV.

From the results gathered we already knew that the morphology of the electric field lines and the electrical potential would suffer significant changes with the variation of both cathode's lengths and secondary electron emission coefficients. Figure (5.32) portraits this behaviour for the best results simulated, which correspond to a $\gamma_i = 0.009$ and $l_c = 21$mm. Here, we observe that the intensity of the field lines inside the hollow cathode become well-defined as the applied voltage increases its value.

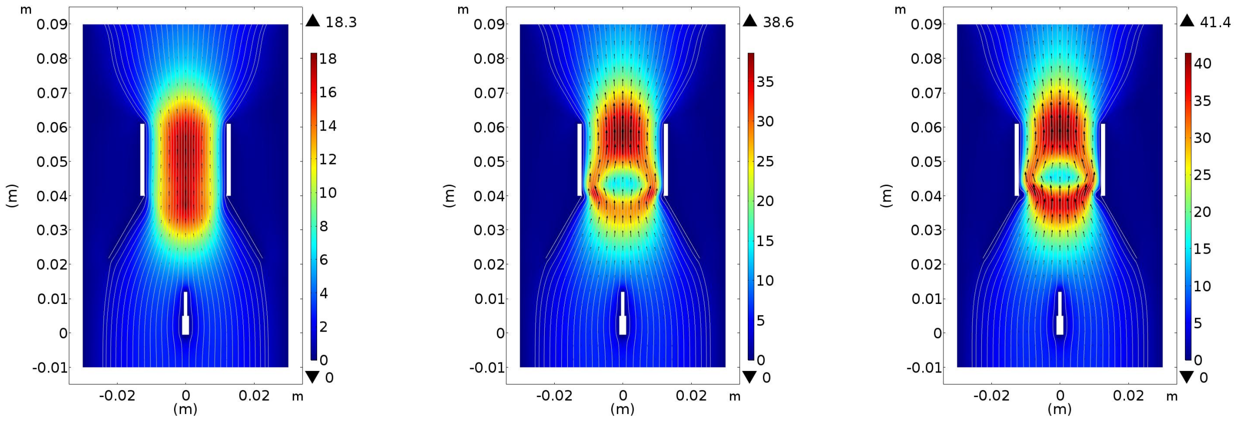

(a) (b) (c)

Figure 5.33: Two dimensional fluid velocity distribution cm $\cdot$ s^{-1}, of a plasma-sliding thruster with a secondary electron emission coefficient of 0.009 and cathode's length of $l_c = 21$mm for different applied voltages. (a) 3kV, (b) 9kV, (c) 12kV.

Nevertheless, the particles scatter along the reactor chamber in a different way from the previously recorded results. This new simulations, see figure (5.34), show that the electrons are more concentrated in the middle area of the domain, with maximum magnitude values of 10^{15}m^{-3}. On the contrary, the ion particles concentrate in specific areas within the hollow cathode with the same magnitude values. This allowed us to increase the local ionization degree to $\approx 10^{-8}$.

In summary, the plasma main velocity will increase with higher values of initial potential difference. This can be observed in the collection of two dimensional fluid velocity profiles of figure (5.33). From the well behaved plasma velocity profile with a maximum speed of a 18cm $\cdot$ s^{-1} at an applied voltage of 3kV, the velocity profile turns into a more dynamic profile, since it starts to appear an deceleration region inside the cathode, with lowest velocity reaching only 10cm $\cdot$ s^{-1} either for initial voltages of 9kV and 12kV. Nevertheless, the maximum speed that this thruster develops is 39cm $\cdot$ s^{-1} and 41cm $\cdot$ s^{-1} for applied voltages of 9kV and 12kV, respectively.

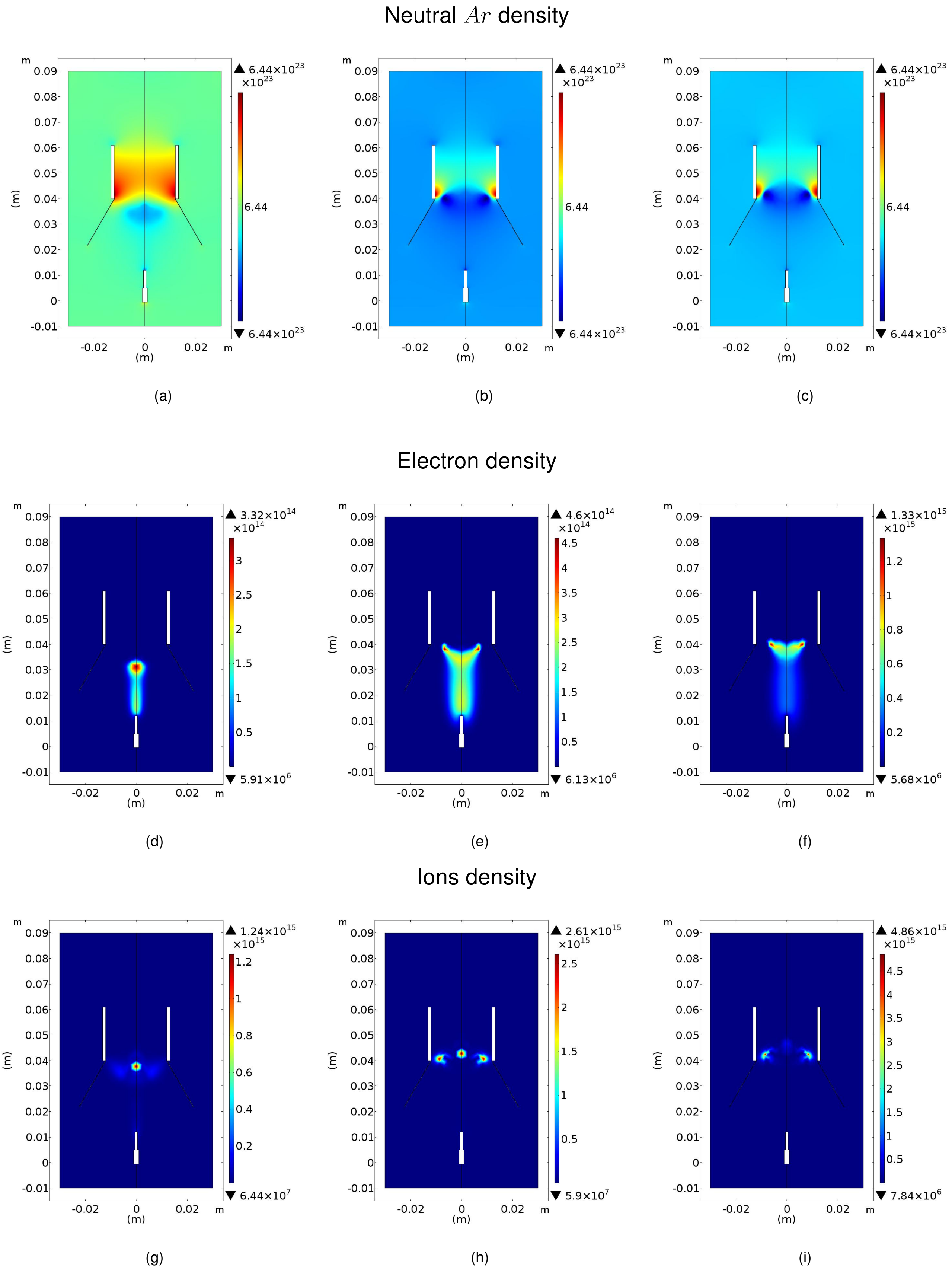

(a) (b) (c)

(d) (e) (f)

(g) (h) (i)

Figure 5.34: Particle densities, in SI units m^{-3}, of a plasma-sliding thruster for with a secondary electron emission coefficient of 0.009 and cathode's length of $l_c = 21$mm for different applied voltages. (a,d,g) 3kV, (b,e,h) 9kV and (c,f,i) 12kV. First row are shows the Ar neutral density, the second row presents the e^- density and the third row shows the Ar^+ ion density.

Regarding the cathode's exit velocity we found out that the linear profile kept the quadratic behaviour as we can perceive through figure (5.35). It is possible to observe that the peak velocity changed from 16cm · s^{-1} at low voltage levels up to 40cm · s^{-1} for high voltages with the same value of secondary electron emission coefficient and cathode's length, an expected increase due to the previous knowledge retrieved about this thrusters.

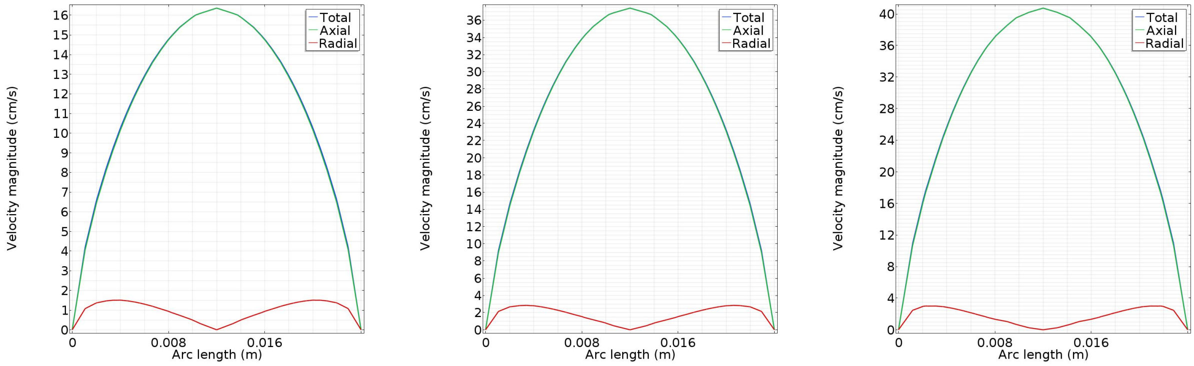

(a) (b) (c)

Figure 5.35: Fluid velocity components at cathode's exit cm · s^{-1}, of a plasma-sliding thruster for with a secondary electron emission coefficient of 0.009 and cathode's length of $l_c = 21$mm for different applied voltages. (a) 3kV, (b) 9kV, (c) 12kV.

These new results show that the dielectric slab does not work well at very low values of $\gamma_i = 0.005$, since the simulations did not converge and the ones that did, produce thrust values below the ones that we were expecting. Nonetheless, we found out that the plasma-sliding increases its thrust for high initial voltages, reaching values over the 1.2μN for $V_0 = 12$kV, presenting a different behaviour regarding the single stage EHD thrusters. For a potential difference between the cathode of 9kV, the thrust reached the micro newton stage as well.

Table 5.8: Argon plasma-sliding thruster's output thrust results in μN for different applied voltages and secondary electron emission coefficients.

	3kV		9kV		12kV	
Cathode length mm	0.005	0.009	0.005	0.009	0.005	0.009
21	0.25	0.20	0.54	1.02	0.64	1.23
15.8	–	0.25	–	0.35	–	0.25
10.5	–	0.17	–	–	–	–

As for the thruster efficiency, the plasma-sliding's thrust-to-power ratio reached values far above the results computed in the previous cases as it can be analysed in table (5.9). Thus, we saw that the efficiency increases up to 240mN/kW for an applied voltage of 9kV with cathode's length of 21mm and $\gamma_i = 0.009$, values in the same range that the half size cathode with an applied voltage of 20kV and $\gamma_i = 0.01$.

Table 5.9: Argon plasma-sliding thruster's efficiency results in mN/kW for different applied voltages and secondary electron emission coefficients.

	3kV		9kV		12kV	
Cathode length mm	0.005	0.009	0.005	0.009	0.005	0.009
21	161.01	139.19	127.81	240.40	102.74	217.44
15.8	–	180.70	–	81.35	–	47.39
10.5	–	132.69	–	–	–	–

5.3 ARGON DUAL STAGE EHD THRUSTER

In this section we present one of the main goals of this project, the dual-stage electrohydrodynamic thruster using argon as the working gas. The design of the two-stage thruster separates control of ionization and acceleration. Therefore we propose and study two different concepts, one by introducing four electrodes with two different sets of high voltage anode and cathode ground and the final geometry consists only with three different geometries, with an high voltage anode, a negative voltage cathode and a cathode ground.

Four electrodes geometry

We started by introducing a new set of high voltage-anode and ground-cathode above the first set. The new electrode's group geometry was designed with the same dimensions of the previous one, with an anode to anode distance of 12mm. Furthermore, we simulated several conditions for the applied voltages in each anode, either the first anode with higher input voltages then the second anode.

The gathered results also showed that for the case where the first anode voltage was lower then the second one, a vortex would rise up between the first cathode ground and the second anode, because of the electric potential distribution. On the other side, the results that converge without any type of vortices would be the cases where the first anode would have higher or equal voltage as the second anode. Then we proceed to discover what be the best potential difference set that would bring the best thruster's parameters. After several attempts, with thrust values in the range of the nano-newtons, we found out that the best set would be $20\text{kV} - 0\text{kV} - 20\text{kV} - 0\text{kV}$ with a secondary electron emission coefficient of $\gamma_i = 0.009$ in each cathode.

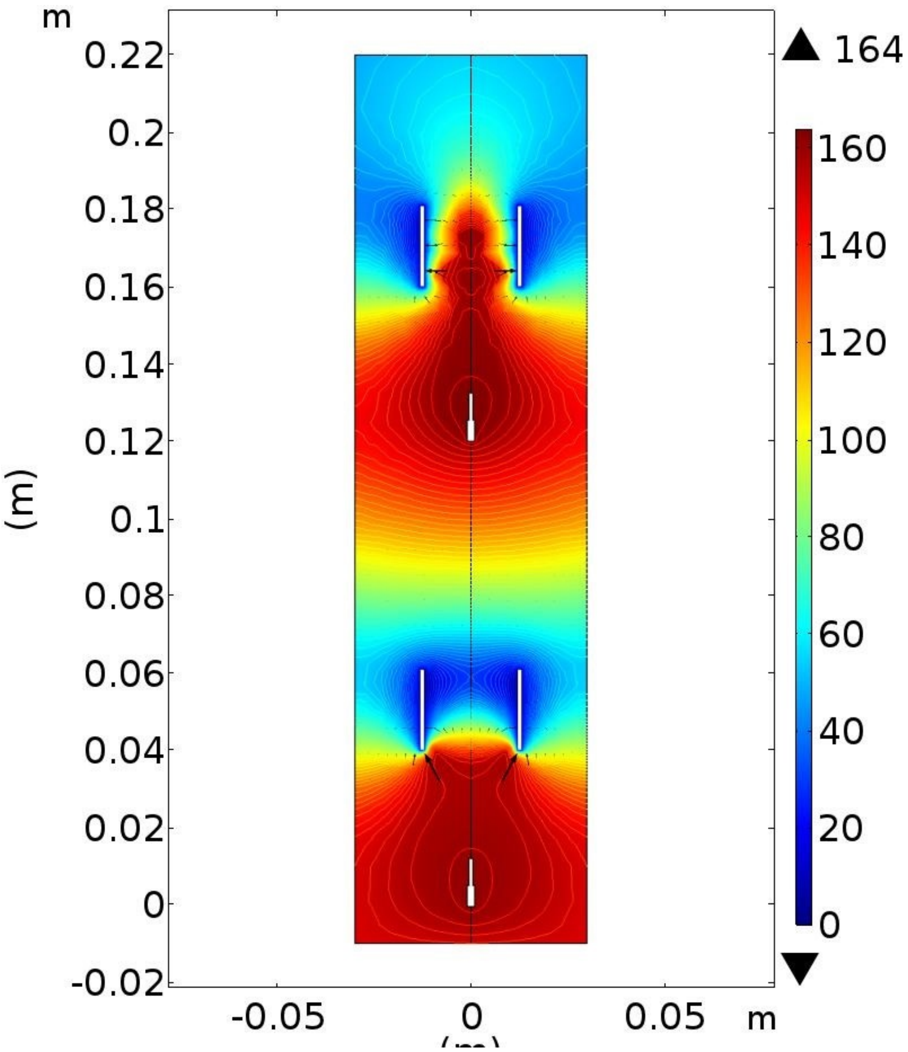

Figure 5.36: Electric potential distribution V, for a four electrodes dual stage EHD thruster with an applied voltages set of $20\text{kV} - 0\text{kV} - 20\text{kV} - 0\text{kV}$.

Although this was the best case, it is possible to perceive from the electric potential distribution, displayed in figure (5.36), that this type of geometry was not optimized mainly due to the potential gradient area between the first cathode and the second anode. Here we see that the ion particles suffer a great loss of momentum since they enter a desaceleration area, where the electric field turns contrary to the direction of movement.

Despite not having the optimal electric potential desired, this thruster compensates by delivering local ionization degrees of 10^{-7} as it can be observed in figures (5.42, 5.43 and 5.44). In fact, both electrons and ions had their maximum peak concentration inside of the second hollow cathode. Electrons scattered in the middle region of this cylindrical electrode, reaching values of $\approx 1.1 \times 10^{16}$m^{-3}, whereas the ions have its highest values near the second cathode's surface and distributed almost to the cathode's exit. They can reach concentrations above the 1.1×10^{16}m^{-3}.

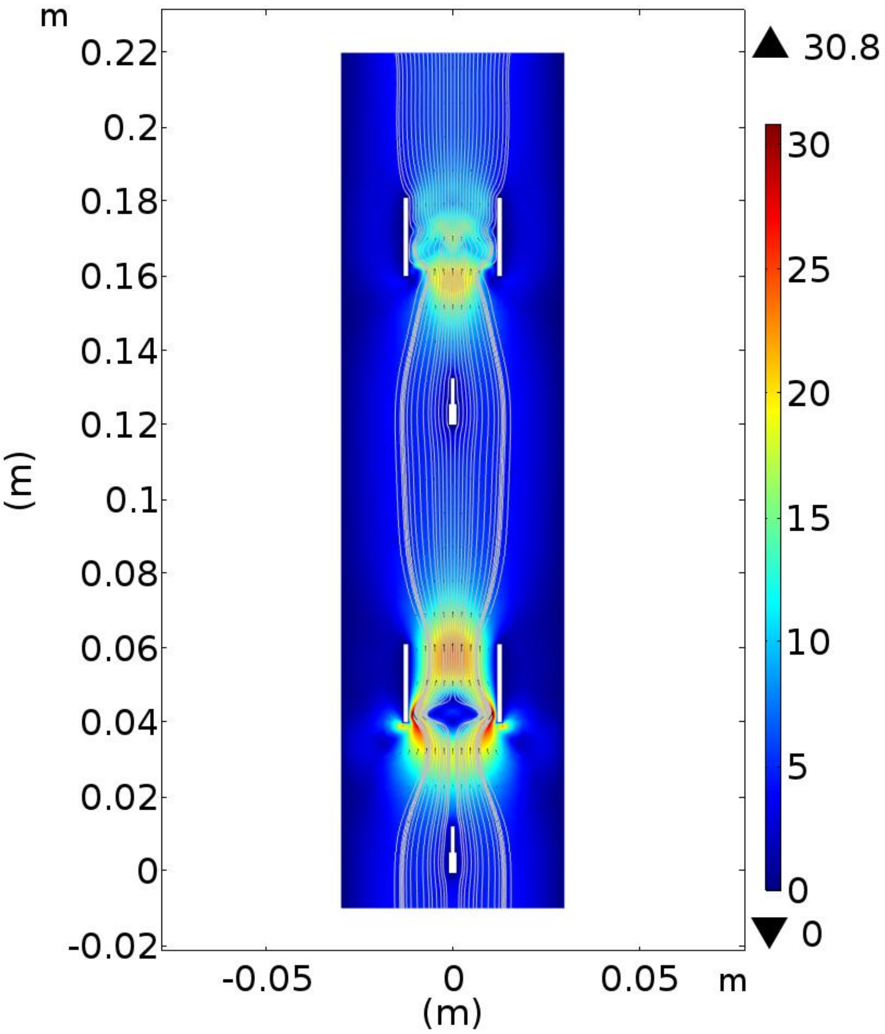

Figure 5.37: Two dimensional fluid velocity distribution cm · s^{-1}, for a four electrodes dual stage EHD thruster with an applied voltages set of 20kV $-$ 0kV $-$ 20kV $-$ 0kV.

The two dimensional plasma main velocity profile shows that the plasma reaches velocities near the first cathode of 30cm · s^{-1} but this reduces slightly to 20cm · s^{-1} in the entry of the second cylindrical cathode. In this region, the velocity profile drops again to velocities near the 10cm · s^{-1}. Overall, the deceleration area can be observed since between the first hollow cathode to the second needle anode, the plasma only reaches speeds of 5cm · s^{-1}.

The results of cathode's exit velocity profile, see figure (5.38), do not show the quadratic profile instead they present a maximum peak velocity in regions between the middle and the cathode's surface, where the middle area shows a reduction of the plasma's speed. After evaluating the thruster's parameters the dual stage argon EHD thruster with a four electrode configuration can deliver up to 53nN with an efficiency of 9mN/kW in the best simulation, pointing out that we were not in its optimal configuration and geometry.

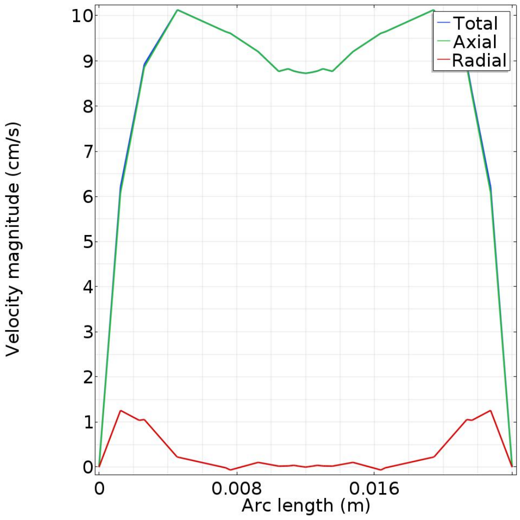

Figure 5.38: Fluid velocity components at cathode's exit cm $\cdot$ s^{-1}, for a four electrodes dual stage EHD thruster with an applied voltages set of 20kV $-$ 0kV $-$ 20kV $-$ 0kV.

Three electrodes geometry

The second part of this study was to develop a three electrode configuration, that is one high voltage anode, one negative voltage cathode and one cathode ground. This part was developed using two different configurations: in the first one, we introduce a negative voltage in the first cathode and set the second cylindrical hollow electrode as a ground voltage, then we simulate the opposite situation. However, we found out that the second case would result in instabilities and simulation errors, due to the fact that the region that neutralizes de gas was in the first cathode and few ions would be used to accelerate the plasma.

Then we ran several different sets of applied voltages and we found out the the thruster would respond very well with tensions of 18kV $-(-2)$kV $-$ 0kV and 15kV $-(-9)$kV $-$ 0kV. Nevertheless, this would only happen if the cathode's inner radius would be increased up to $r_i = 18$mm, since the results didn't converge at all or would form instabilities within the plasma.

The electric potential shows that this geometry set is the right choice, see figure (5.39). In direct comparison with the four electrode configuration, we see that the three electrodes develop an electric potential distribution more favourable to the acceleration of the ion charged particles. We also found out that by reducing the negative voltage down to -9kV, we created an acceleration region, that would be neutralized in the second anode, as we can find in several grid ion engines configurations (Sangregorio et al. (2018)).

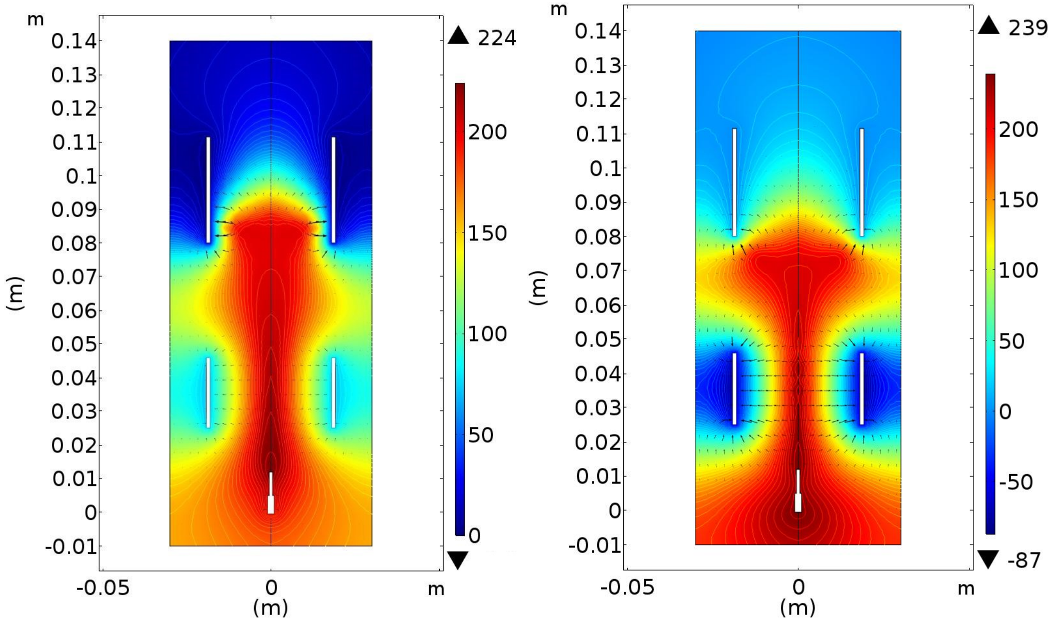

(a) (b)

Figure 5.39: Electric potential distribution V, for a three electrodes dual stage EHD thruster with an applied voltages set of (a) $18\text{kV} - (-2)\text{kV} - 0\text{kV}$ and (b)$15\text{kV} - (-9)\text{kV} - 0\text{kV}$.

The particles distribution are also very distinct from each voltage set as it can be observed in figure (5.45). For instance the first case, we saw a electrons scatter along the middle of the thruster, and although it reached its maximum peak of $7 \times 10^{15}\text{m}^{-3}$ it presents a uniform distribution from the anode to the second cathode. On the contrary for the second case, the electrons form local peaks inside the middle of the first cathode, with concentration values of $1.9 \times 10^{17}\text{m}^{-3}$, two orders of magnitude above. For the ions we also observe quite the similar behaviour despite the local peak concentrations in the second cathode we find for the first case. Meanwhile in the second one, we observe the same local concentrations that appear in the electrons, reaching also values of $1 \times 10^{17}\text{m}^{-3}$. From this point we can perceive that the ionization degree, in these regions is near 10^{-6}, the highest value reach in all of these simulations.

Since the particles had distinct profiles for each voltage set, it would be expected that the velocity profiles would be different. In fact this assumption can be verified in figure (5.40). The set with a negative voltage -2kV, presents a more uniform velocity profile along the three electrodes. After the anode, the plasma increases its speed up to $10\text{cm} \cdot \text{s}^{-1}$ within the first anode, decreases a little by the end of the first cathode and it accelerates again when the plasma reaches the second cathode, reaching is maximum velocity of $17\text{cm}\cdot\text{s}^{-1}$. Then the plasma decreases its velocity, due to a stationary region inside the second cathode.

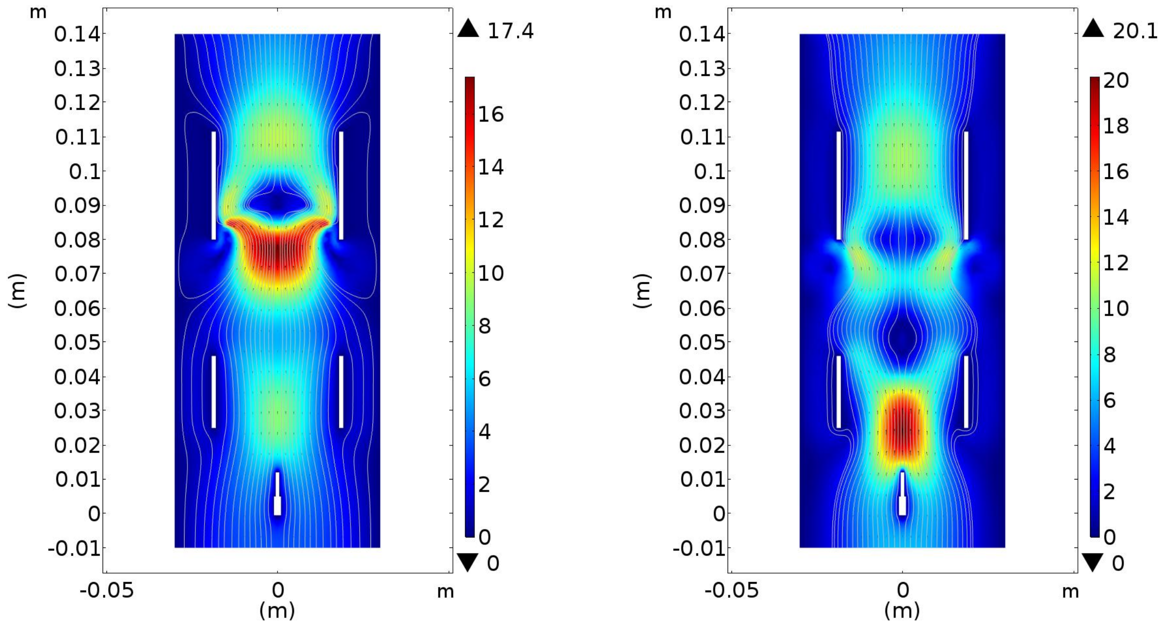

(a) (b)

Figure 5.40: Two dimensional fluid velocity distribution $\text{cm}\cdot\text{s}^{-1}$, for a three electrodes dual stage EHD thruster with an applied voltages set of (a) $18\text{kV} - (-2)\text{kV} - 0\text{kV}$ and (b)$15\text{kV} - (-9)\text{kV} - 0\text{kV}$.

On the opposite side, when we applied a negative voltage of -9kV, the two dimensional plasma velocity profile becomes more dynamic, with the appearance of two stationary regions, one at the exit of the first cathode and the other at the entry of the second cathode. Starting from the anode, the plasma speeds up to its maximum speed , with values of $20\text{cm}\cdot\text{s}^{-1}$, then it suffers a great reduction, reaching the first stationary stage. It is followed by an increase and a decrease of its speed, reaching the second stationary regime. Then the plasma's velocity speeds up again up to $11\text{cm}\cdot\text{s}^{-1}$.

The cathode's exit velocity profiles are also very distinct for each set of negative voltage, see figure (5.41). We observed that for the first case, the radial component of the velocity has a considerable presence and the axial component did not reach its peak in a quadratic profile, but instead it created a plateau right in the middle of the cathode. However, for the second set of negative voltage we observed the well behaviour of a quadratic profile with a maximum speed of $11\text{cm}\cdot\text{s}^{-1}$.

After evaluating the thruster's parameters for each case we discovered that the dual stage argon EHD thruster with a three electrode configuration can deliver up to 158nN with an efficiency of 20mN/kW for the applied voltage set 18kV $-$ (-2)kV $-$ 0kV and 215nN with an efficiency of 32mN/kW for the applied voltage set 15kV $-$ (-9)kV $-$ 0kV. This allows us to asses that the three electrode geometry produces better results then the four electrode configuration. Yet this part of the study is not fulling improved, lacking of a deep investigation.

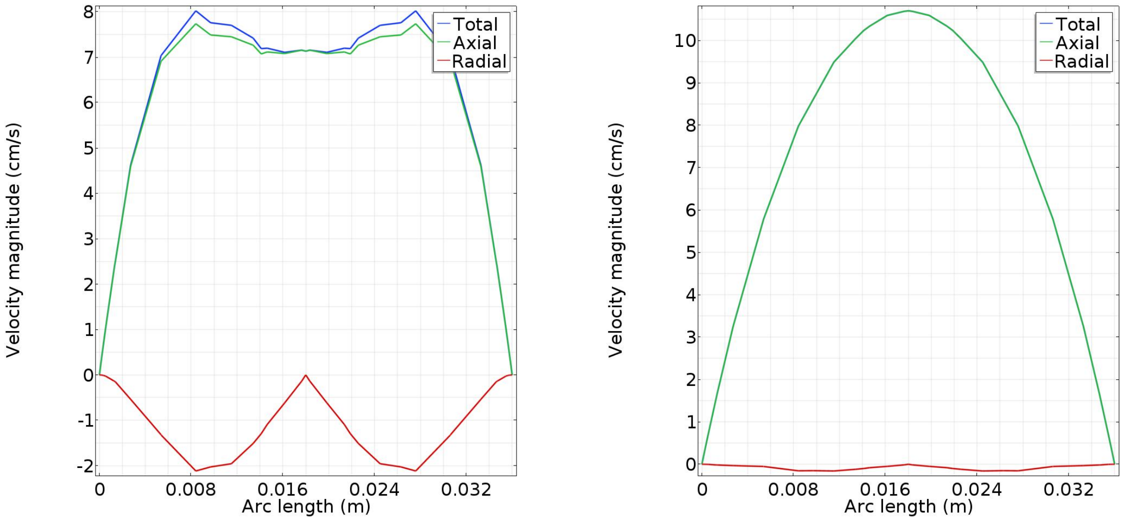

(a) (b)

Figure 5.41: Fluid velocity components at cathode's exit cm · s^{-1}, for a three electrodes dual stage EHD thruster with an applied voltages set of (a) 18kV $-$ (-2)kV $-$ 0kV and (b)15kV $-$ (-9)kV $-$ 0kV.

5.4 CONCLUSIONS

In conclusion we improved the previous argon propellant EHD thruster developed by Granados in his PhD Thesis by changing and studying the influence of several key parameters. We started by changing the discharge current by varying the ballast resistor or the applied voltage, which we found out that by reducing the resistor around 5 times, the thruster would deliver 5 times more output thrust and if we used an applied voltage of 20kV, we would deliver thrusts almost half of a micro-newton.

Then we studied the influence of the cathode's intrinsic geometry. We first saw that the inner radius was already optimized, so we dedicated this study to the improvement of the cathode's length. We set different applied voltages and we concluded that for each voltage, different results would be produced for each length. At this point, we improved the thruster up to 0.93μN by reducing to half the cathode's size.

Then we simulated the response of each cathode while decreasing the secondary electron emission coefficient. With this study and by using experimental results we improved the thruster up to 2.75μN and its efficiency up to 295mN/kW, the highest values using argon propellant by reducing the cathode's size in half, and applying a $\gamma_i = 0.009$.

Then we decided to study the plasma-sliding effect. We started by increasing the aperture angle (in the range of 0° to 30°) of a dielectric slab, the morphology of the electric field lines and the electrical potential inside the cathode changed considerable and the species distributions (electrons and positive ions) varied as well. With an increase of the aperture angle, there was an increase of the net thrust. Specifically, at 30ř, the deliver thrust was 106[nN], and the thrust-to-power ratio was 101mN/kW for 30° of aperture angle.

After fixing the aperture angle at 30°, we changed both cathodes height and the applied voltage. We observed that at 9kV, the thrust output was higher, given 500[nN] (with a cathode of 10.5mm), a 2 times increase, regarding the single stage EHD thruster without the dielectric chimney. These results showed that the efficiency of the T/P increased, reaching 172mN/kW.

Then we changed both length and secondary electron emission coefficient and we discover that the plasma-sliding thruster would deliver 1.23μN and 217μN with a lower voltage then the non-dielectric thruster.

At last we investigated the argon propellant dual-stage EHD thruster. The approach taken was to developed two different configurations, the four electrode and three electrode. We concluded that the best one was the three electrode since it developed distinct regions, acceleration and neutralization, that are essential for the development of the thruster. Overall by using a set of applied voltages of 15kV$-(-9)$kV-0kV, the improved thruster delivered 215nN with an efficiency of 32mN/kW, clearly this thruster is not so efficient as the others developed.

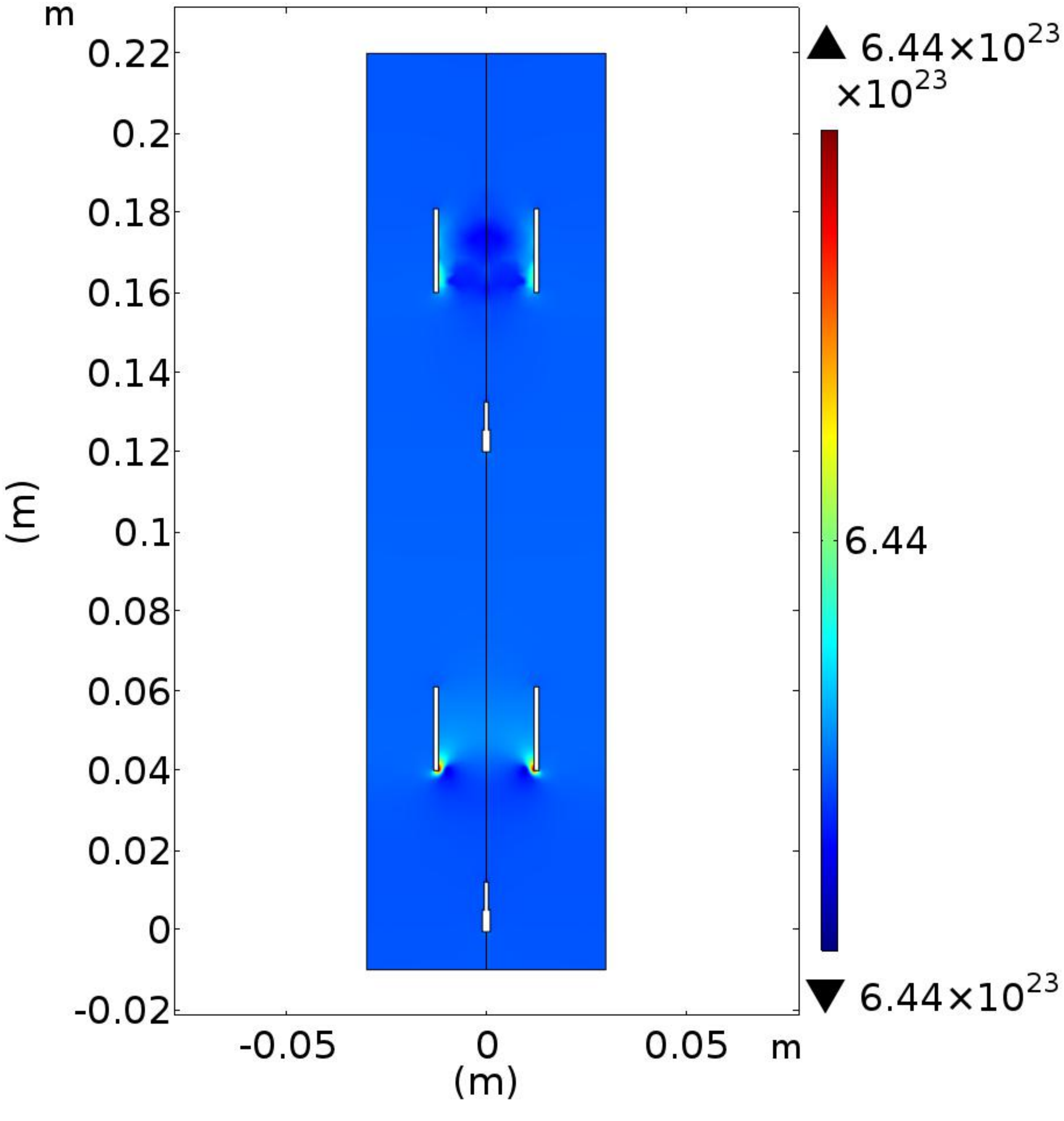

Figure 5.42: Neutral argon number distribution m^{-3}, for a four electrodes dual stage EHD thruster with an applied voltages set of $20\text{kV} - 0\text{kV} - 20\text{kV} - 0\text{kV}$.

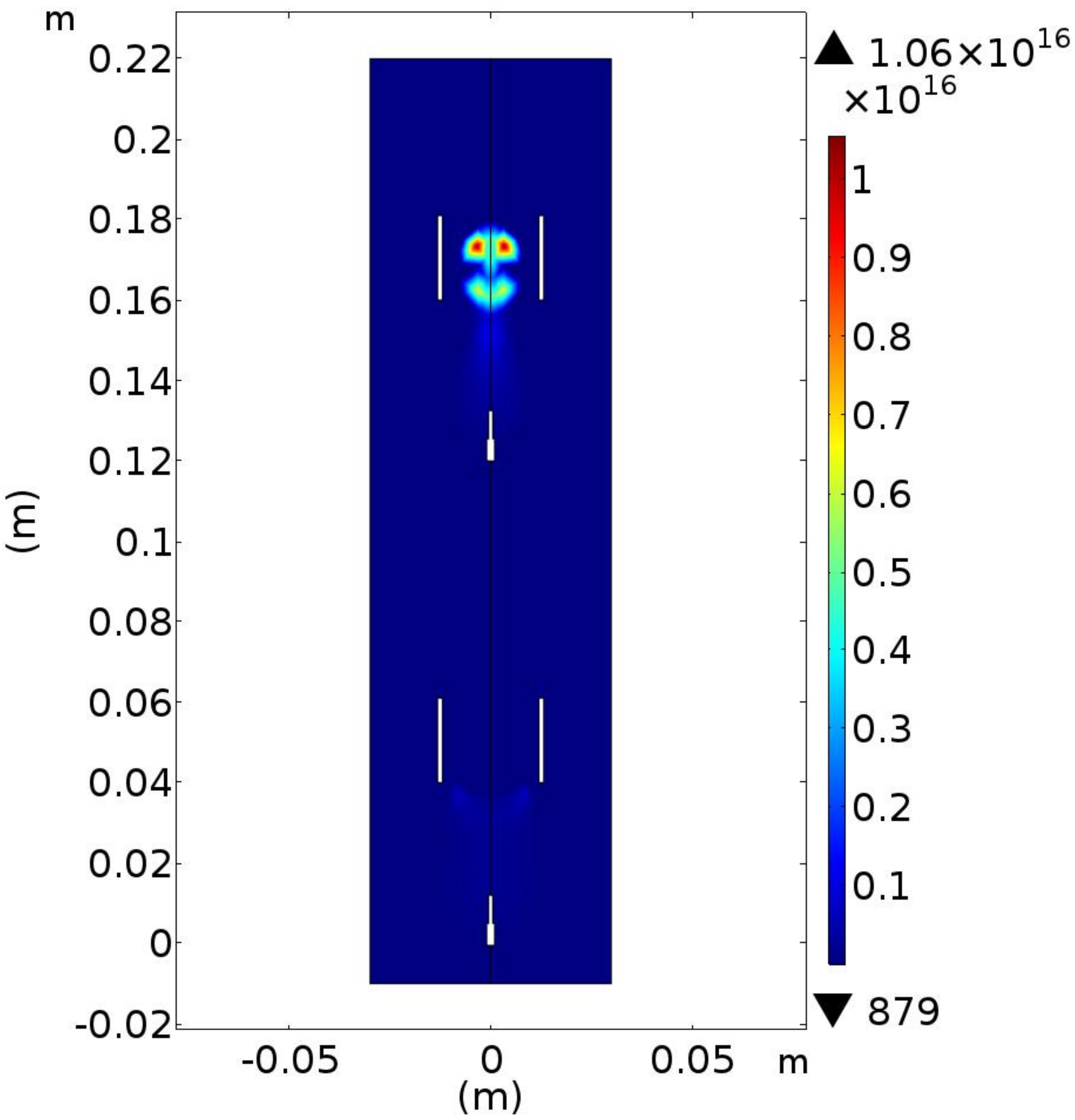

Figure 5.43: Electron number distribution m^{-3}, for a four electrodes dual stage EHD thruster with an applied voltages set of $20\mathrm{kV} - 0\mathrm{kV} - 20\mathrm{kV} - 0\mathrm{kV}$.

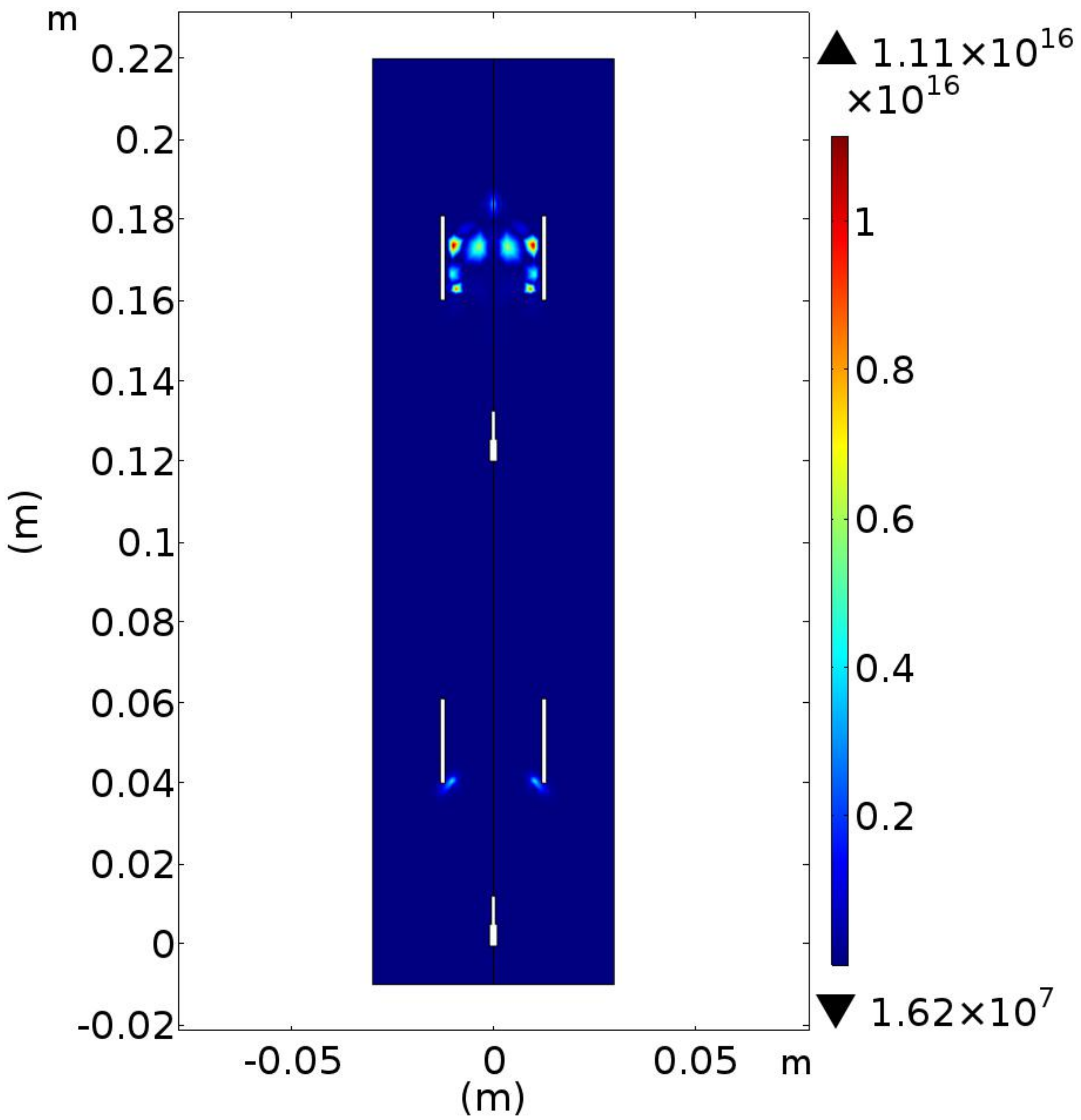

Figure 5.44: Ion argon number distribution m^{-3}, for a four electrodes dual stage EHD thruster with an applied voltages set of $20\mathrm{kV} - 0\mathrm{kV} - 20\mathrm{kV} - 0\mathrm{kV}$.

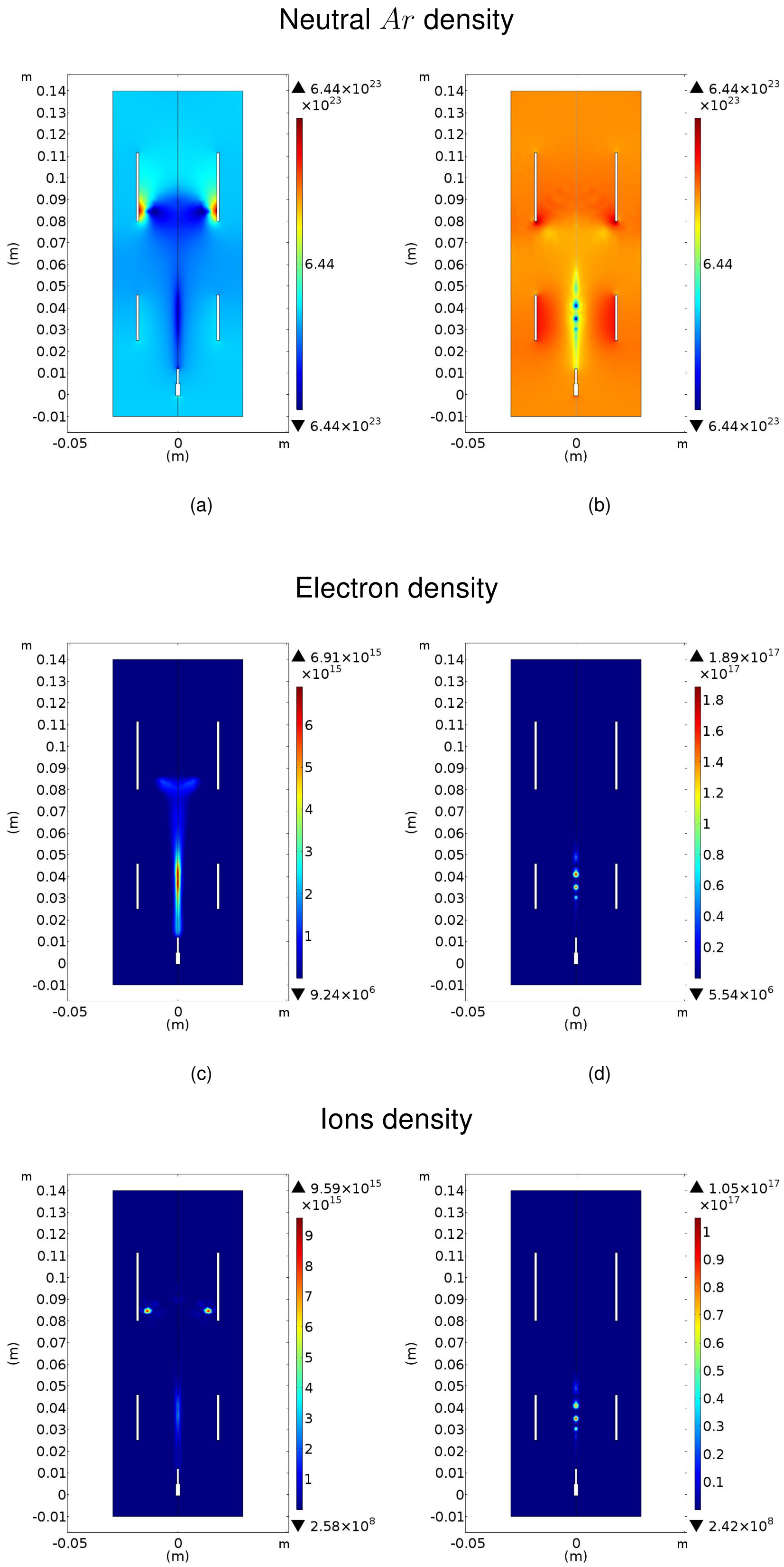

(a) (b)

(c) (d)

(e) (f)

Figure 5.45: Electric potential distribution V, for a three electrodes dual stage EHD thruster with an applied voltages set of (a) $18\text{kV} - (-2)\text{kV} - 0\text{kV}$ and (b)$15\text{kV} - (-9)\text{kV} - 0\text{kV}$.

Chapter 6.

Optimization of a xenon propellant EHD thruster

Xenon propellant is the most used in ion engines and Hall thrusters despite its costs and availability, making other noble gases, such as argon and krypton, potential substitutes. However, this last gases present more issues in terms of thruster performance specifications, due to the fact that have lesser molecular mass than xenon and need a higher ionization energy. In general, a more dense propellant will improve the output thrust and also its efficiency since is has a higher energy per particle for the same exhaust velocity (Crofton and Hain (2007)).

In this chapter we will present the the behaviour of the electrohydrodynamic thruster with this propellant. We started by improving the optimal geometry by changing the cathode's inner radius and its length. Then we decided to study the behaviour of the thruster, changing the secondary electron emission coefficient and the geometry of the cathode, changing from cylindrical into a cone, and varying the opening angle. Finally, we simulated a potential concept in a dual stage thruster, with a needle-type anode cover with a cylindrical anode.

6.1 INFLUENCE OF THE CATHODE'S GEOMETRY

In these simulations we used the experimental value for the secondary electron emission coefficient taken from table (3.3) in page (30), $\gamma_i = 6.87 \times 10^{-4}$, and the dynamic viscosity for xenon was taken from table (3.2) in page (27), $\eta = 2.31$. For the electric circuit parameters we used an applied voltage of $V_0 = 20$kV, a ballast resistor of $R_b = 500$MΩ and an blocking capacitor of $C_b = 1$pF.

Variation of the cathode's inner radius

We began our walk with xenon by increasing the hollow radius of the cathode from 12mm as the best inner radius to the argon working gas to 22mm. As we know from the previous chapter, this change can produce significant modifications in the electric potential distribution that will eventually improve the considered thruster.

Figure (6.1) displays the morphology of the electric potential distribution in the xenon gas at 10Torr and 300K. We can see that even at its narrower radius, 12mm, the thruster's potential distribution has a different profile in comparison to the same case in the argon thruster. However with xenon, the electric potential gradient is more distributed inside the cathode, allowing for a bigger particle acceleration volume. With the increase of the inner radius, the electric potential gradient expands to regions far off the the cathode's extremities.

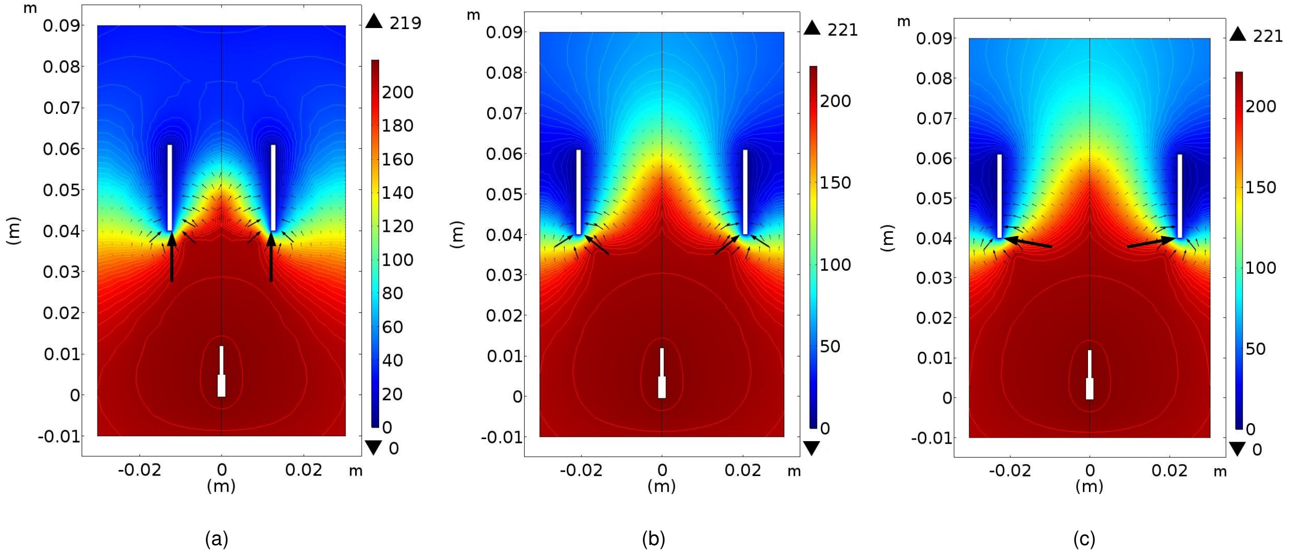

(a) (b) (c)

Figure 6.1: Electric potential distribution V for different inner radius of a xenon propellant hollow cathode EHD thruster. (a) 12mm, (b) 20mm, (c) 22mm.

As the electric potential changed, so changed also how the particles are scattered along the simulation domain, see figure (6.2). We observed that for several inner radius, both charged and non charged particles showed distinct distribution profiles. Although Xenon atoms distributed quite in the same behaviour as they reach its maximum concentrations near the cathode's entry surface where they were preceded by a lowest concentration, the charged particles demonstrated very different behaviours as the inner radius got bigger.

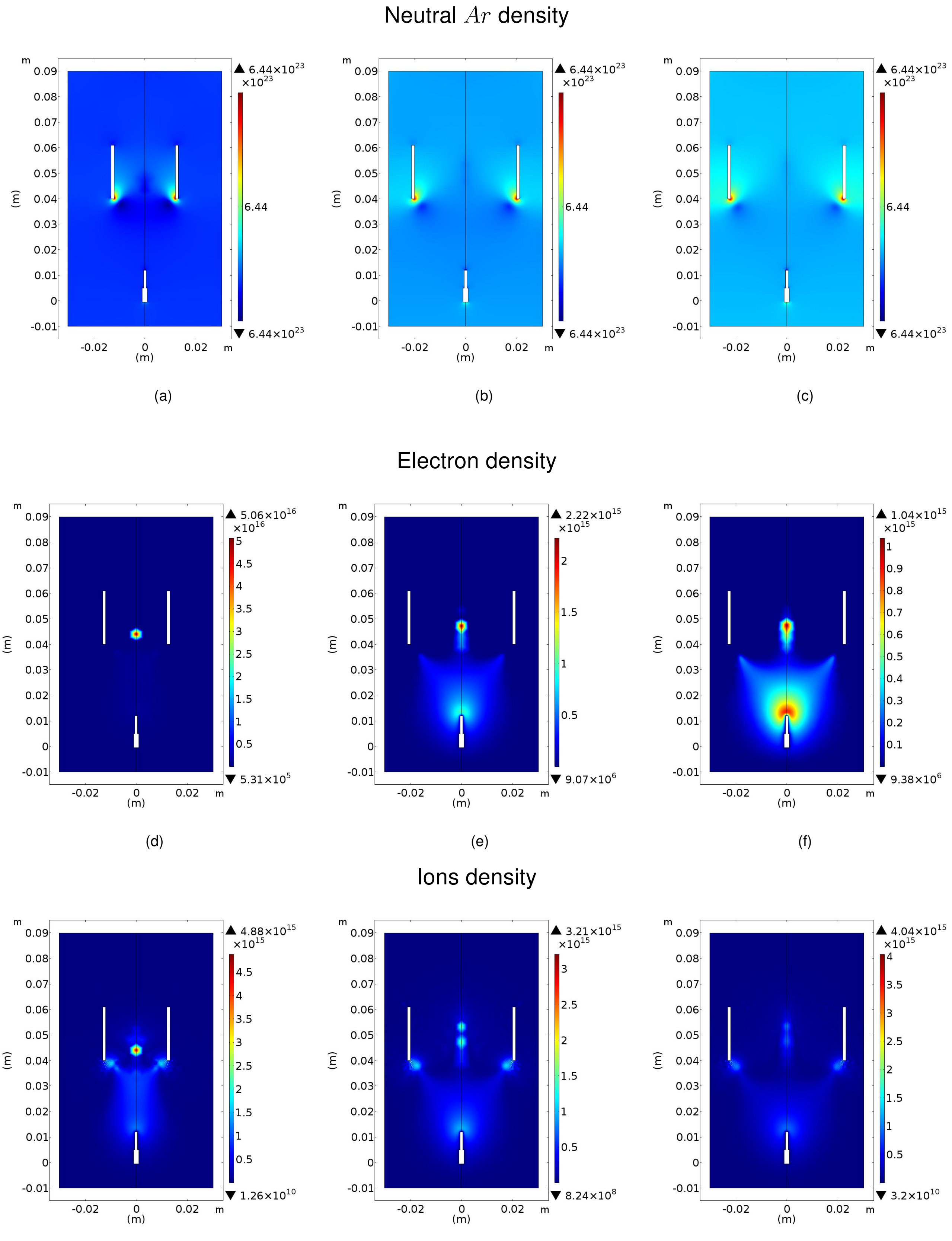
Neutral Ar density

(a) (b) (c)

Electron density

(d) (e) (f)

Ions density

(g) (h) (i)

Figure 6.2: Particle densities m^{-3}, for a varying cylindrical cathode's inner radius, r_i, of a xenon propellant EHD thruster. (a,d,g) 10mm, (b,e,h) 12mm and (c,f,i) 16mm. First row are shows the Xe neutral density, the second row presents the e^- density and the third row shows the Xe^+ ion density.

At first, electrons show a local concentration inside the hollow cathode of above 5×10^{16}m^{-3} that begins to disperse as the radius increases; we see that more electrons started to appear in the region between both electrodes and its maximum peak drops down to $\approx 1 \times 10^{15}$m^{-3}, for $r_i = 20$mm. In the meantime, the Xe^+ ions show specific patterns for each inner radius, but they always nearly maintain the same maximum peak magnitude of $\approx 1 \times 10^{15}$m^{-3}, pointing out that locally we reach high ionization degrees.

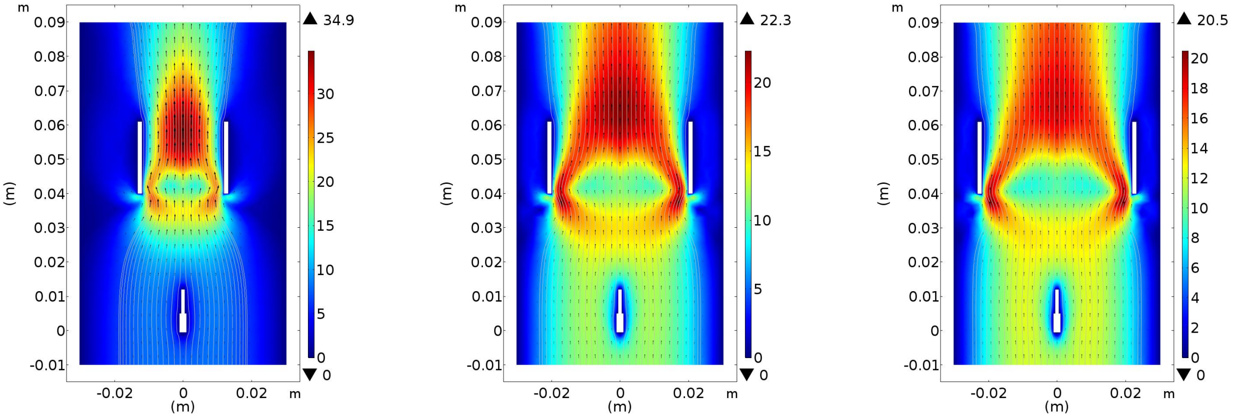

(a) (b) (c)

Figure 6.3: Two dimensional xenon plasma fluid's velocity profile cm $\cdot$ s^{-1} for different inner radius. (a) 12mm, (b) 20mm, (c) 22mm.

As for the main plasma velocity, the two dimensional profile can be observed in figure (6.3). In a first analyses we can perceive that the plasma shows a laminar behaviour, checking that it shows the *Bernoulli*'s principle due to the fact that by increasing the inner radius, that increases the area inside the cathode and consequently the main speed drops. In a more detailed approach we found out that for a inner radius of $r_i = 12$mm, the fluid velocity profile is quite similar to the correspondent case of the argon thruster, where the stationary region is converted to a lower velocity area and the maximum velocity is nearly 35cm $\cdot$ s^{-1}. However the same did not happen as the inner radius got bigger. Although its maximum peak has dropped down to 20cm $\cdot$ s^{-1}, the rest of plasma increased up its speed, even the plasma expelled from the cathode maintains its high velocity values.

The results of the axial component of the fluid velocity at the cathode's exit show that, although the maximum peak velocity is found at the narrower cathodes, its the wider hollow cylindrical electrodes that have more particles with higher speeds, which is a more favourable regime for the development of better thrust results.

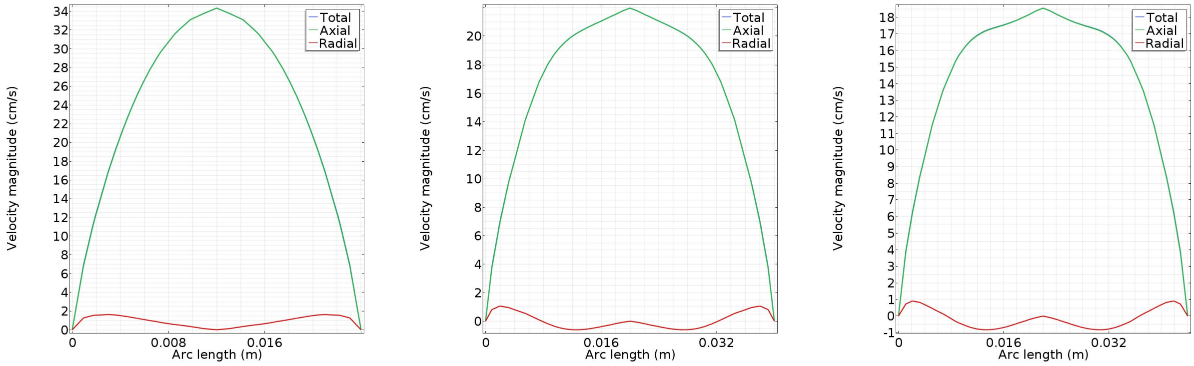

(a) (b) (c)

Figure 6.4: Expelled xenon plasma fluid's velocity cm $\cdot$ s^{-1} for different inner radius at the exit of the cathode. (a) 12mm, (b) 20mm, (c) 22mm.

Variation of the cathode's length

In this study we used the same parameters as those previously used in the previous study. In summary, the experimental value for the secondary electron emission coefficient was taken from table (3.3), $\gamma_i = 6.87 \times 10^{-4}$, and the dynamic viscosity for xenon was taken from table (3.2), $\eta = 2.31$. For the electric circuit parameters we used an applied voltage of $V_0 = 20$kV, a ballast resistor of $R_b = 500\text{M}\Omega$ and an blocking capacitor of $C_b = 1$pF. The cathode's inner radius was set at $r_i = 20$mm.

We started by reducing the cathode's length down to 12.6mm . These modifications can generate significant changes in the electric potential distribution that could improve the main thruster. As we were reducing its length, we observed that values under the 12.6mm wouldn't not improve but instead would produce instabilities in the plasma.

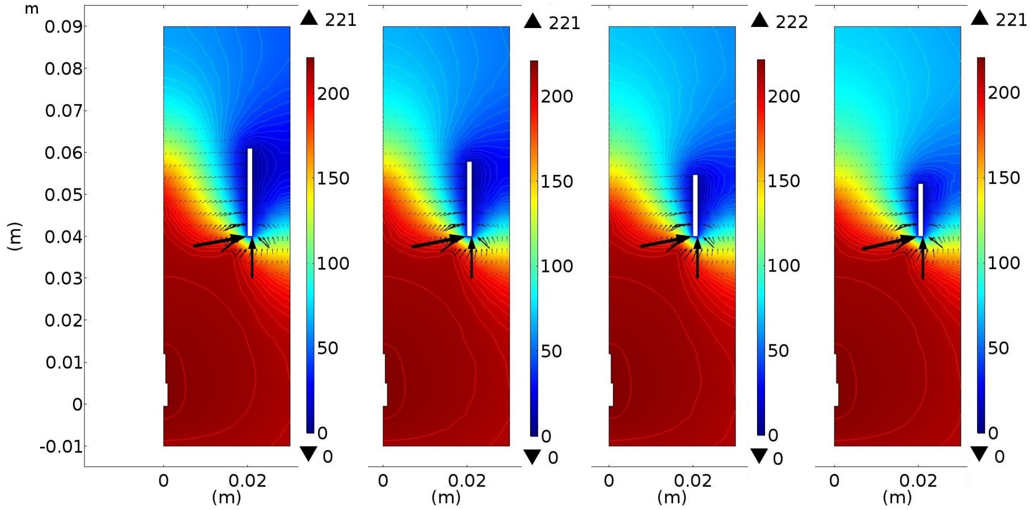

Figure 6.5: Electric potential distribution in V, for different cathode's lengths of the xenon EHD thruster. From the left to the right, 21mm, 17.9mm, 14.7mm and 12.6mm.

Neutral Ar density

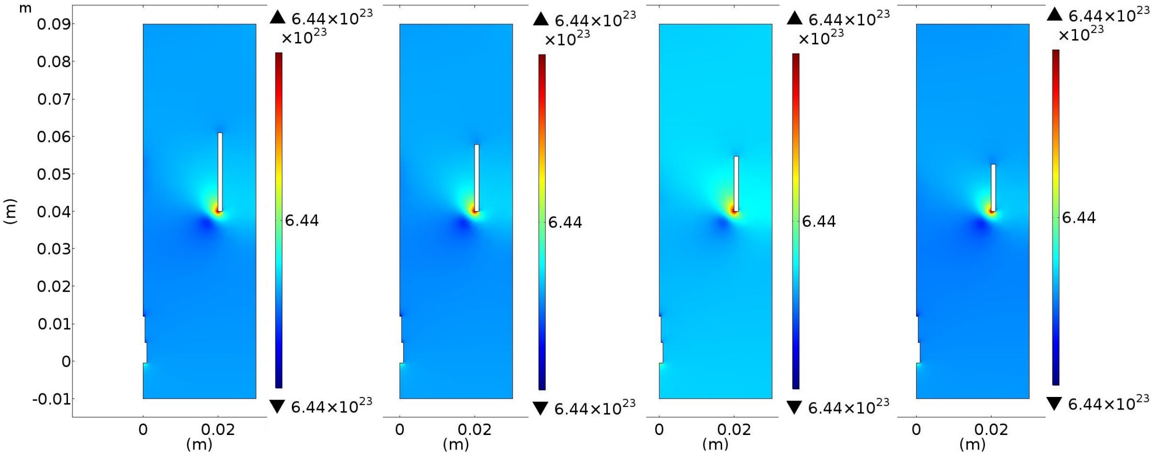

Electron density

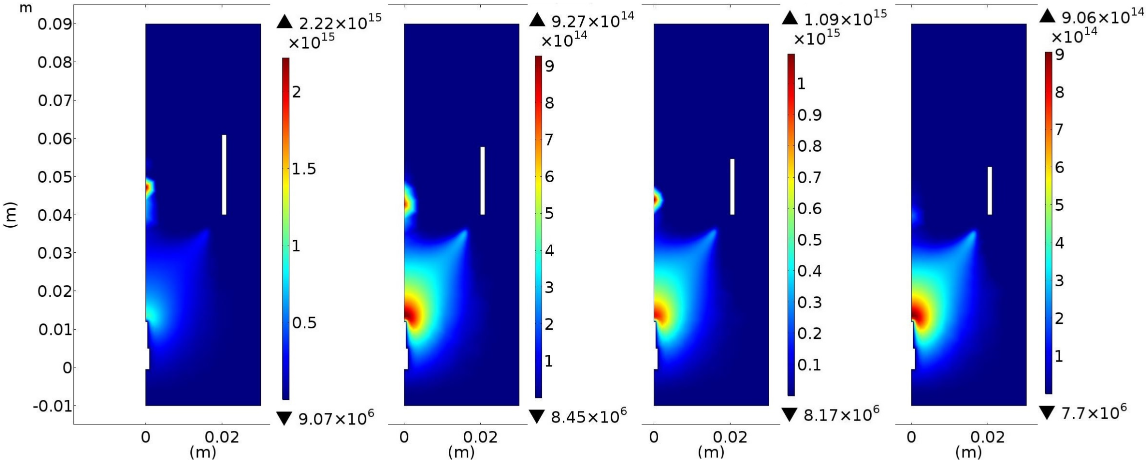

Ion density

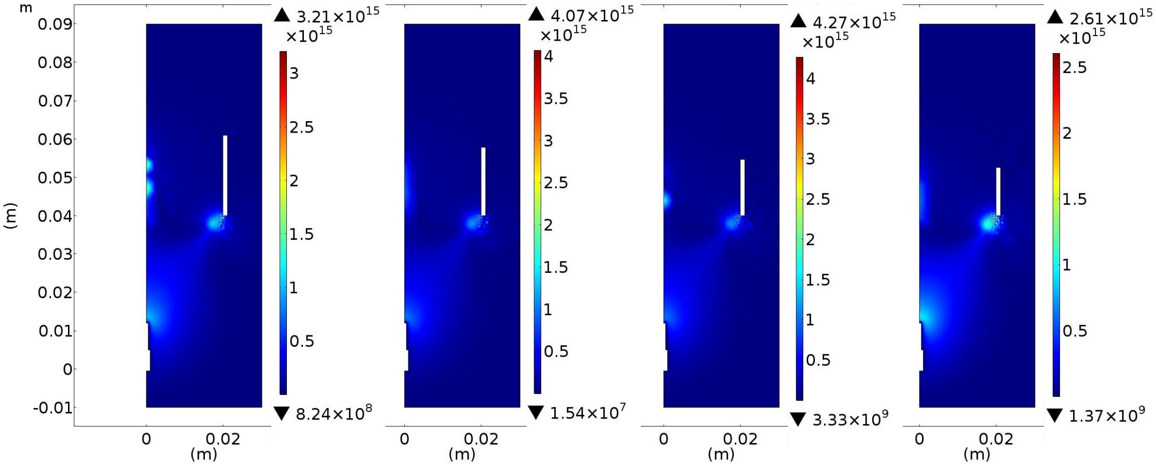

Figure 6.6: Particles distribution m^{-3}, , for different cathode's lengths of the xenon EHD thruster. From the left to the right, 21mm, 17.9mm, 14.7mm and 12.6mm. The first row is represented the neutral Ar atoms, the second row is represented the electrons and in the third row is represented the Ar^+ ions.

Figure (6.5) displays how the morphology of the electric potential distribution in a xenon gas changes slightly has the cathode's dimensions decreases. In this set of results, we can perceive that electric potential is already optimized since the profiles are similar in each case. However we should point out that the electric field has the orientation desirable even when it is outside the hollow cathode.

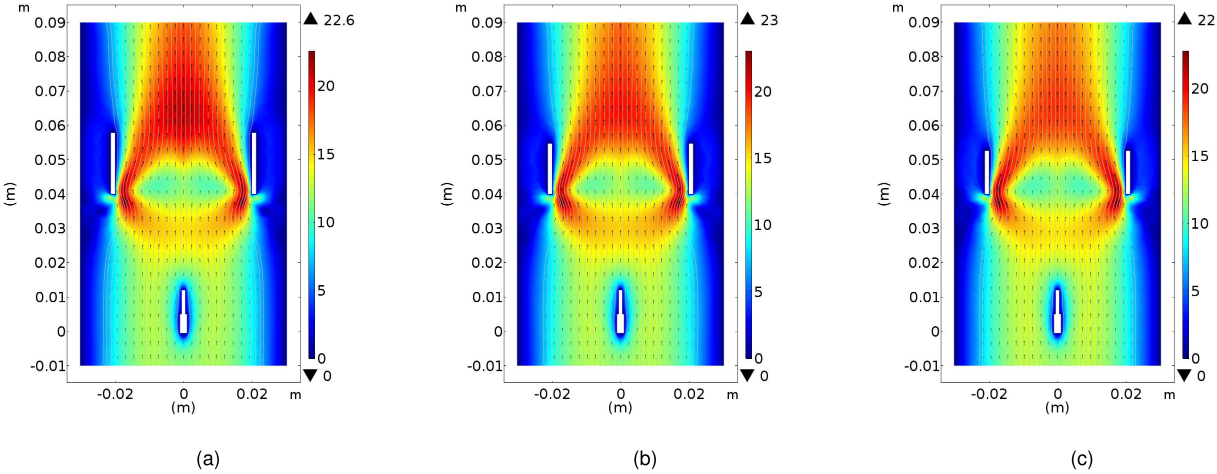

Figure 6.7: Two dimensional xenon plasma fluid's velocity profile cm·s^{-1} for different cathode's lengths. (a) 17.9mm, (b) 14.7mm and (c) 12.6mm.

In terms of particle distribution we also found out that it changes slightly as the cathode's dimensions decreases, as we were expecting due to the similarities on the electric potential distribution. Yet we must mention that for a cathode's length of $l_c = 14.7$mm we reached the maximum ion local concentration of 4.27×10^{15}m^{-3}, indicating that this regime would be the most prospecting to deliver the best thrust since it produces the higher ionization degree.

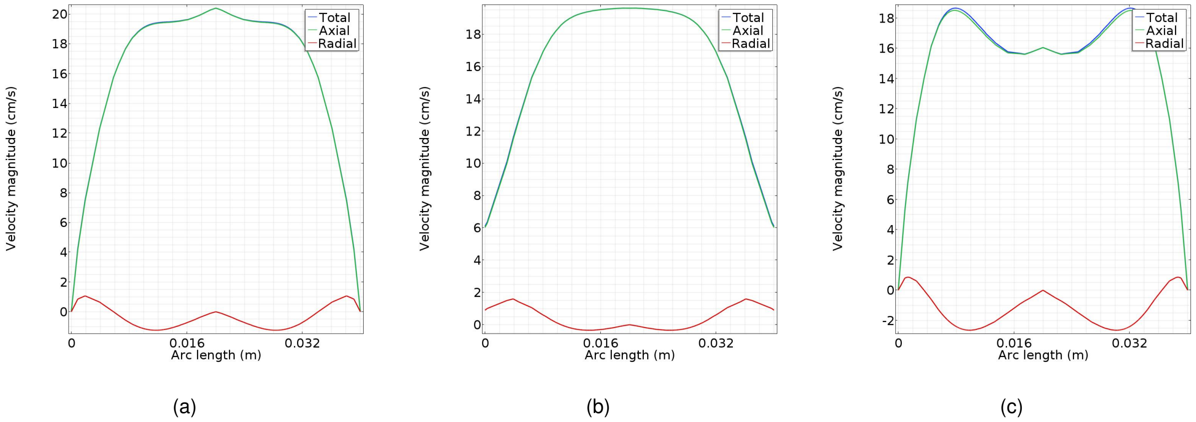

Figure 6.8: Expelled xenon plasma fluid's velocity cm $\cdot$ s^{-1} for different cathode's lengths. (a) 17.9mm, (b) 14.7mm and (c) 12.6mm.

In figure (6.7) we observe the two dimensional profile of the xenon gas' main velocity for various cathode's sizes. Overall, we found out that the plasma maintains approximately the same behaviour with maximum peak velocities of $23\text{cm} \cdot \text{s}^{-1}$. However the expelled velocity changes considerably when the cathode decreases in size, which eventually develop different thrust values.

Thruster's parameters vs cathode geometries

In the next paragraphs we will discuss the thruster's performance regarding each geometry's change. Figure (6.9) shows all the recorded data. The first row shows how the thrust changes with the variation of the inner radius and with the cathode's length,t where the red curves show the xenon gas with a $\gamma_i = 6.84 \times 10^{-4}$ and the blue curves represent the argon gas $\gamma_i = 0.05$. These results were presented to the 9^{th} International Workshop & Summer School on Plasma Physics, IWSSPP-2020.

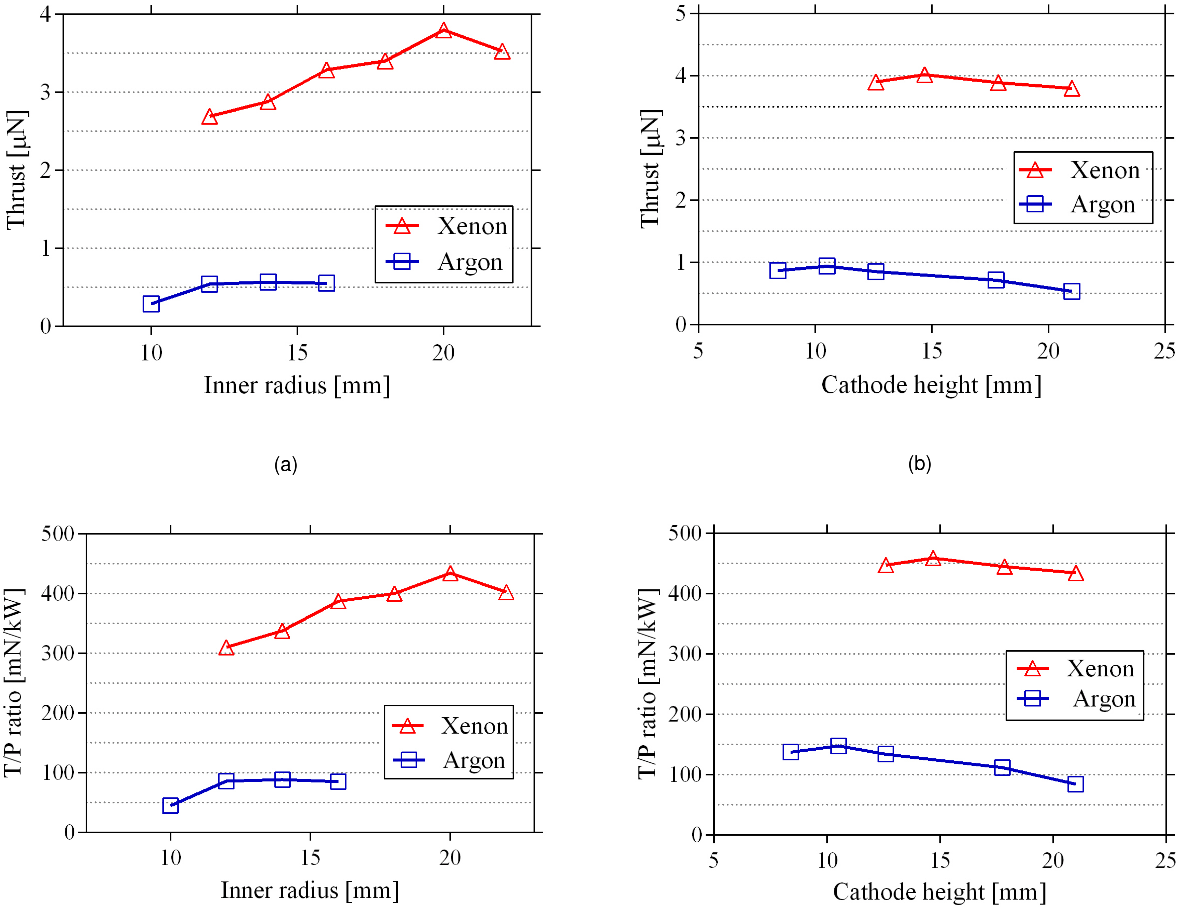

(a)

(b)

(c)

(d)

Figure 6.9: Variation of plasma-sliding thruster parameters for different cathode's lengths and applied voltages (a) output thrust μN, (b) thrust-to-power ratio mN/kW.

With Argon as the propellant gas, we verified that the width was already optimized in 12mm, since any other variation, upper or lower, would decrease the output thrust and the thruster efficiency. On the opposite hand, when using Xenon, we concluded that the optimal hollow radius was 20mm. With the change of the cathode's length we discovered that the xenon propellant would reach its optimal state with an length of 14.7mm. Overall the xenon thruster delivered an output thrust of 3.80μN and thrust-to-power ratio of 434mN/kW, values that when comparing with the current state-of-art of the modern electric propulsion systems reach the same order of magnitude see table (2.2) in page (20).

6.2 INFLUENCE OF THE SECONDARY ELECTRON EMISSION COEFFICIENT

After we acquired sufficient knowledge regarding the cathode's geometry, it was time to study the influence of second *Towsend* discharge parameter,γ_i in the xenon propellant EHD thruster. For this study we set the initial voltage at 20kV, a ballast resistor of $R_b = 500\text{M}\Omega$ and an blocking capacitor of $C_b = 1$pF and we vary the secondary electron emission coefficient from $[4.87 \times 10^{-4} - 6.00 \times 10^{-2}]$.

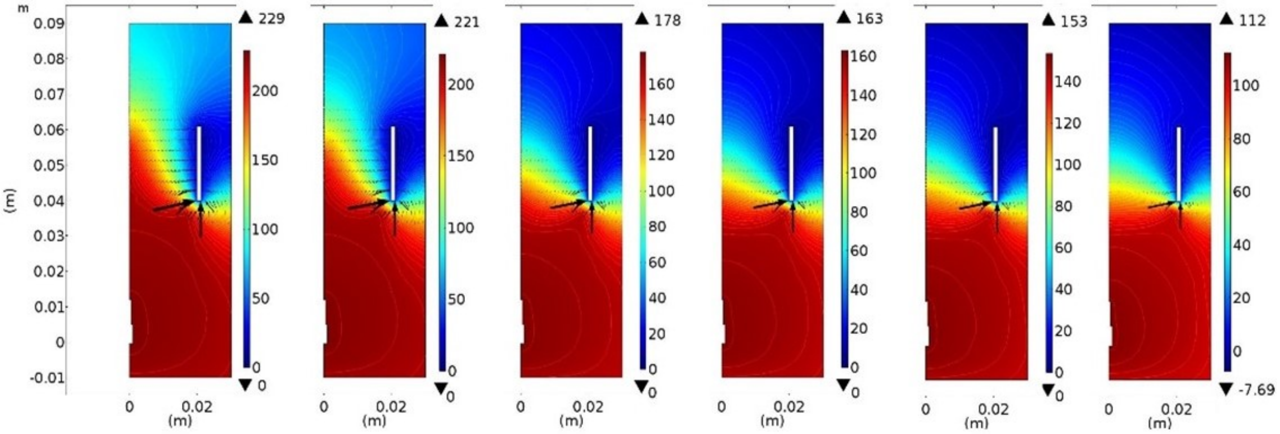

Figure 6.10: Electric potential distribution V, for different γ_i values for a Xenon propellant thruster, from the left to the right, i) 4.87×10^{-4}, ii) 6.87×10^{-4}, iii) iv) 4.87×10^{-3}, v) 6.87×10^{-3}, vi) 1.00×10^{-2} and vii) 6.00×10^{-2}.

We observed computationally that the secondary electrons play an important role in the modulation of a xenon electrohydrodynamic thruster as it did in the argon thruster. Figure (6.10) shows how the morphology of the electric field lines and the electric potential distribution change as γ_i increases its value. For values above 10^{-3}, the electric field showed a similar profile, where the electric potential stairway gradient ends inside the cathode. Whereas for values of γ_i smaller then

10^{-3}, the electric profile passes the extremities of the cathode.

These two different potential profiles make all the particle species within the simulation domain demonstrate two different behaviours as we can observe in figure(6.14). We observed that for higher coefficients, electrons show a maximum concentration near the cathode, that changes up to the middle of the hollow cathode, as the γ_i decreases in magnitude. Whereas the ions tend to form local concentrations inside the cathode as long the cathodes emit a low number of secondary electrons. Although the thruster present two different behaviours regarding the secondary electron emission coefficient, the xenon thruster always delivers the same ionization degree, which is approximately 10^{-8}.

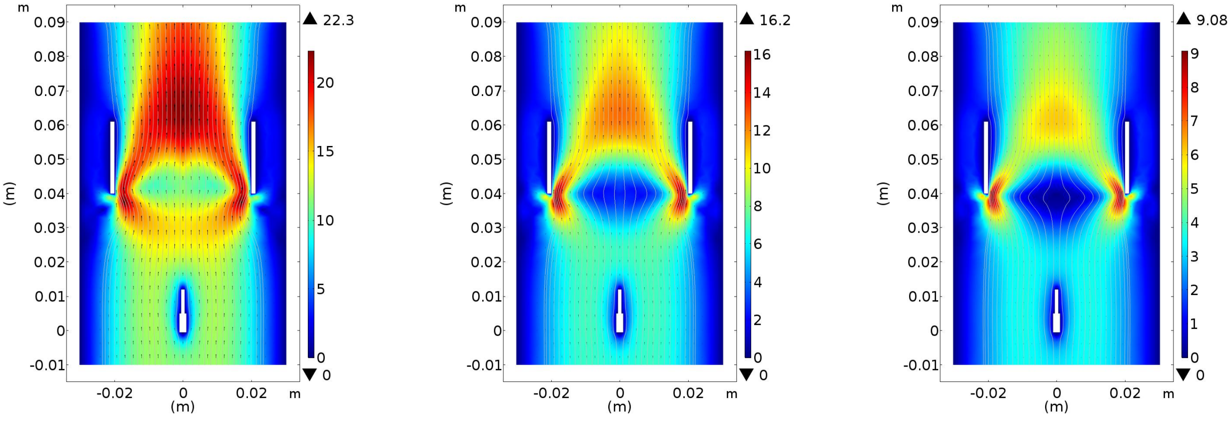

(a) (b) (c)

Figure 6.11: Two dimensional xenon plasma fluid's velocity profile cm $\cdot$ s^{-1} for different secondary electron emission coefficient γ_i. (a) 6.87×10^{-4}, (b) 6.87×10^{-3}, (c) 6.00×10^{-2}.

The less electrons are emitted from the cathode, more ions concentrate inside the cathode, and this phenomenon leads to an increase of the xenon main velocity as it is shown in figure (6.11). For high coefficient values the thrust only reached speeds of 9cm $\cdot$ s^{-1} as for lower values, the velocity increased up to 22cm $\cdot$ s^{-1}, a near 2.5 times increase. Analyzing more precisely the plasma velocity, we found out that the stationary region created within the cathode's entry (for high γ_i values) became a dynamic region, reaching speeds of 10cm $\cdot$ s^{-1}. We also pointed out that after the cathode, the plasma still maintained velocities above 20cm $\cdot$ s^{-1} for secondary electron emission coefficient values lower then 10^{-3}.

At the cathode's exit the xenon gas velocity is also distinct for each electron emission coefficient. We observed that for lower γ_i values the exit velocity stayed approximately the same, 22cm $\cdot$ s^{-1}, to the one of maximum plasma velocity along the simulation domain. Yet when more electrons started to be emitted from the cathode, the expelled velocity dropped down to nearly $12\text{cm} \cdot \text{s}^{-1}$ for $\gamma_i = 6.87 \times 10^{-3}$ and only to $6\text{cm} \cdot \text{s}^{-1}$ for $\gamma_i = 6.0 \times 10^{-2}$.

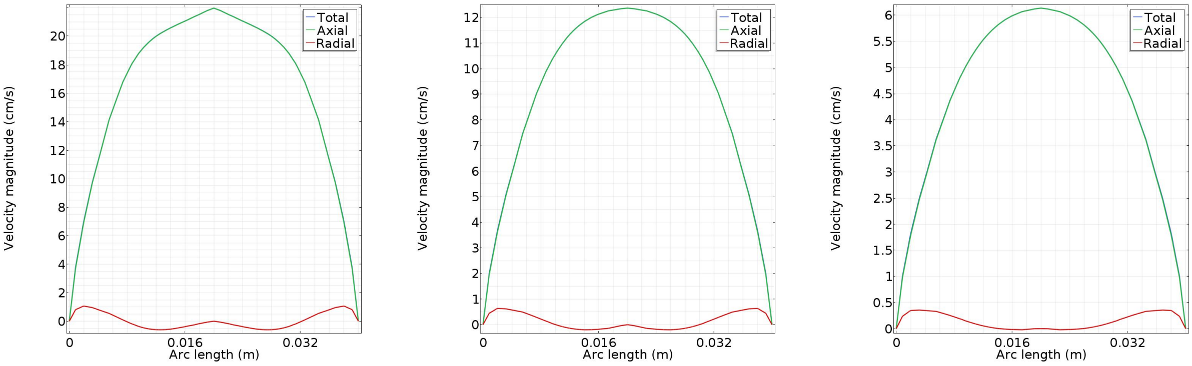

(a) (b) (c)

Figure 6.12: Expelled xenon plasma fluid's velocity $\text{cm} \cdot \text{s}^{-1}$ for different secondary electron emission coefficient γ_i. (a) 6.87×10^{-4}, (b) 6.87×10^{-3}, (c) 6.00×10^{-2}.

Overall we plotted all the thruster parameters into a thrust vs γ_i and thrust-to-power ratio vs γ_i graphics, see figure (6.13), and we observed that only by reducing the electrons emitted by the cathode's surface, the thruster reached output thrust of 4μN and efficiencies of nearly 460mN/kW. Whereas for higher γ_i values, the thrust would only deliver a thrust of 0.24μN and an efficiency of 80mN/kW.

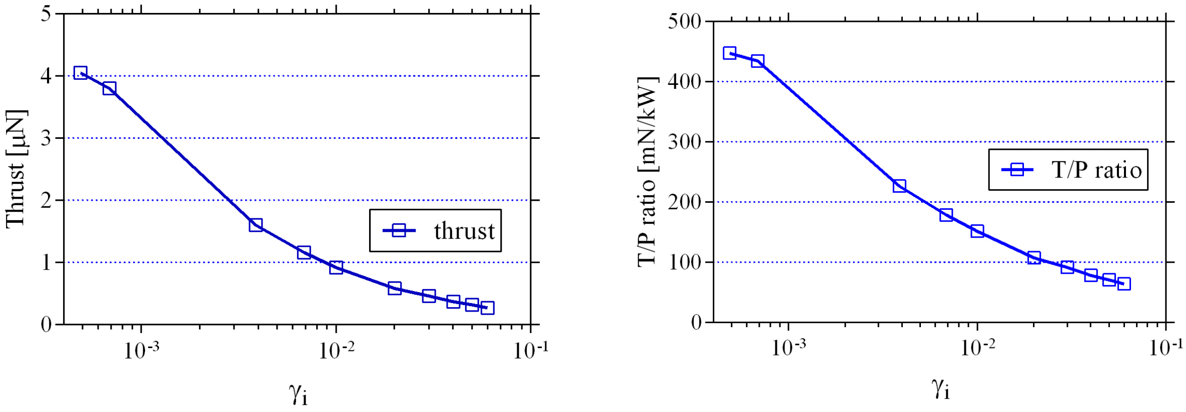

(a) (b)

Figure 6.13: Variation of xenon propellant thruster parameters for different values of secondary electron emission coefficient, γ_i at an applied voltage of 20kV. (a) output thrust μN, (b) thrust-to-power ratio mN/kW.

Neutral Ar density

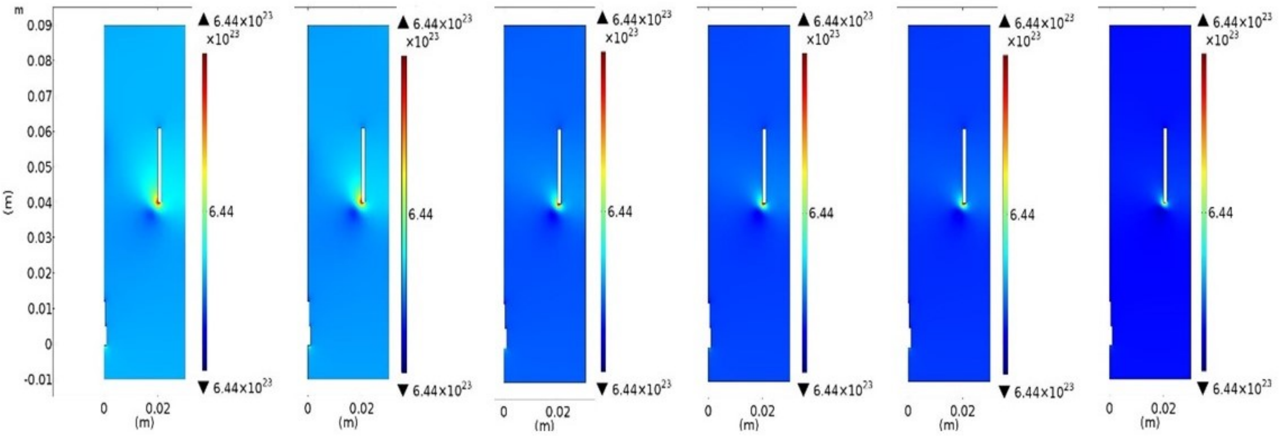

Electron density

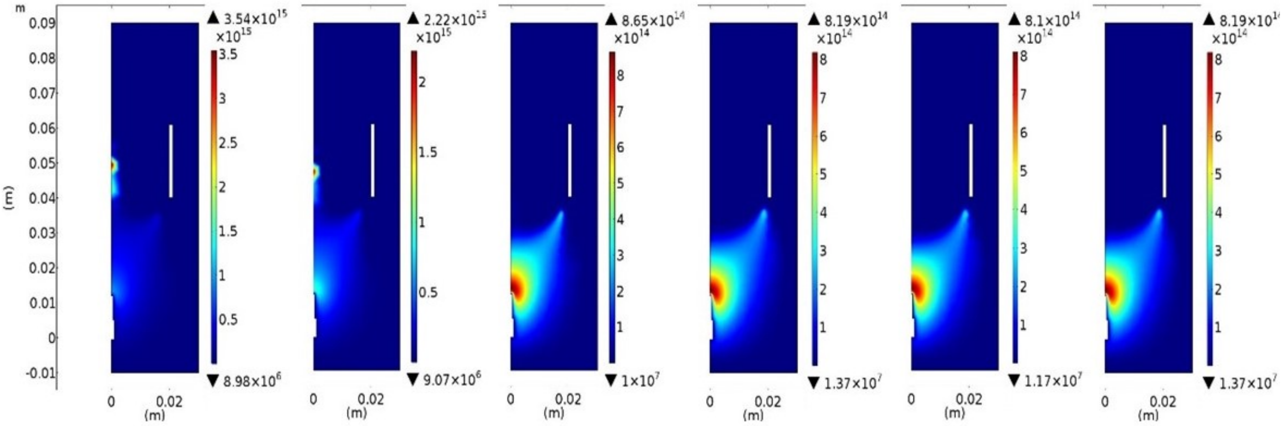

Ion density

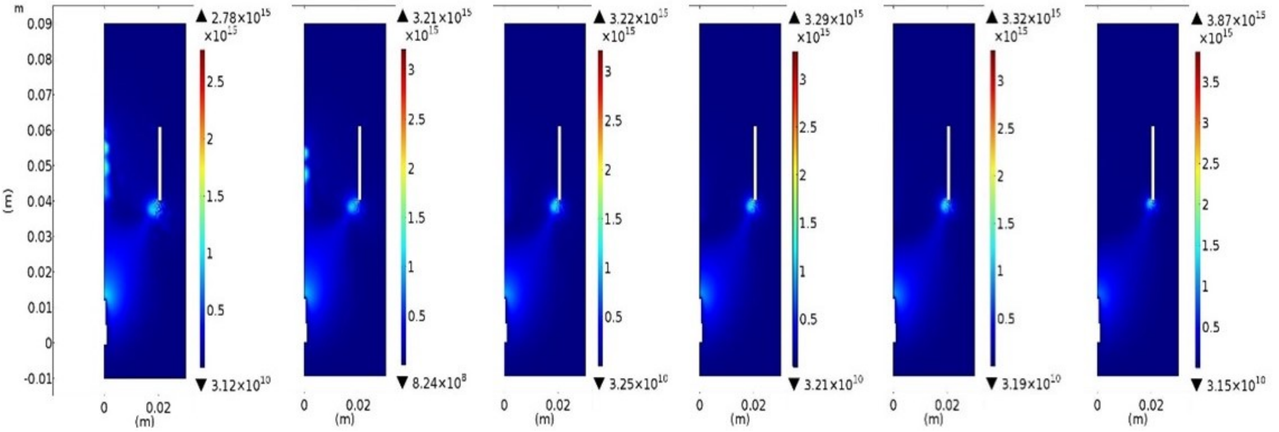

Figure 6.14: Particles distribution m^{-3}, for a Xenon propellant thruster, from the left to the right, i) 4.87×10^{-4}, ii) 6.87×10^{-4}, iii) iv) 4.87×10^{-3}, v) 6.87×10^{-3}, vi) 1.00×10^{-2} and vii) 6.00×10^{-2}. In the first row is represented the neutral Xe atoms, the second row is represented the electrons and in the third row is represented the Xe^{+} ions.

6.3 INFLUENCE OF THE CONE ANGLE

In this section we decided to turn the cylindrical cathode into an cathode cone, by increasing or reducing its aperture angle. In these simulations we set the initial voltage at 20kV, a ballast resistor of $R_b = 500\text{M}\Omega$ and an blocking capacitor of $C_b = 1$pF and we vary the secondary electron emission coefficient from 6.87×10^{-4}. The angle interval used in this study was from $[-15°, 15°]$.

Through figure (6.15) we can assess that for negative angles, the thruster would not be in its favourable regime despite having the smallest area at the cathode's exit. This is because the electric potential does not scatter far away the cathode's point of exit, situation that we already verify as the most desirable.

The non charged and charged particles, due to the distinct electric potentials, show very different distribution profiles regarding the cone angle. From figure (6.22) we observed that for negative angles, the electrons have a maximum concentration inside the cathode and as long the angle increased, they tend to scatter to regions near the anode. Whereas, xenon ions tend to be more concentrated near and inside the hollow cathode.

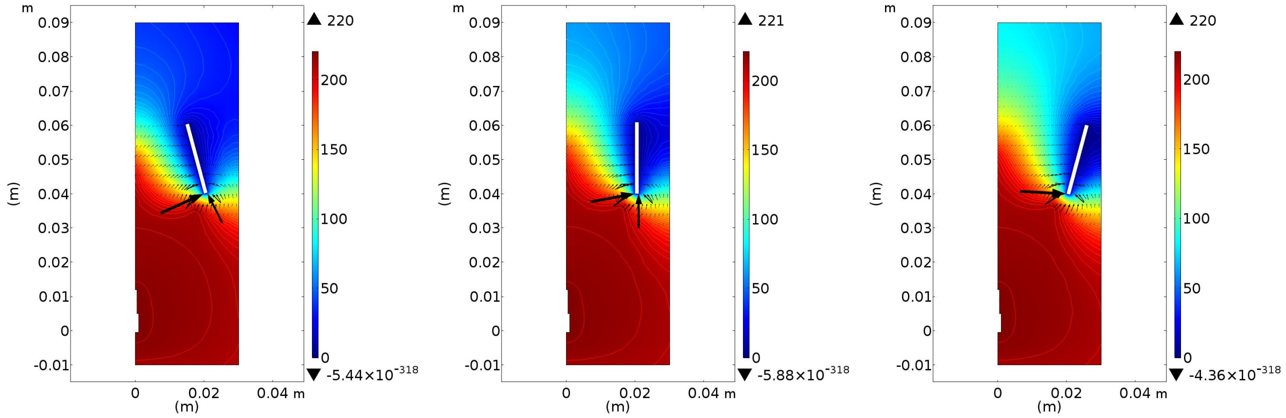

(a) (b) (c)

Figure 6.15: Electric potential distribution V, for different cone angles, with applied voltage of 20kV. (a) $-15°$, (b) $0°$ and (c) $15°$.

As it would be expected the plasma developed different velocity profiles as well. We see from figure (6.15) that for negative angles, the cathode's exit area is smaller, which tends to increase the fluid velocity, due to the fact the gas has a laminar behaviour. However, as we will see later, this velocity increased did not compensate for the fact that for wider areas, more plasma is passing through. Nevertheless, we can observe by the fluid velocity behaviour alone, that the cylindrical cathode produces better results.

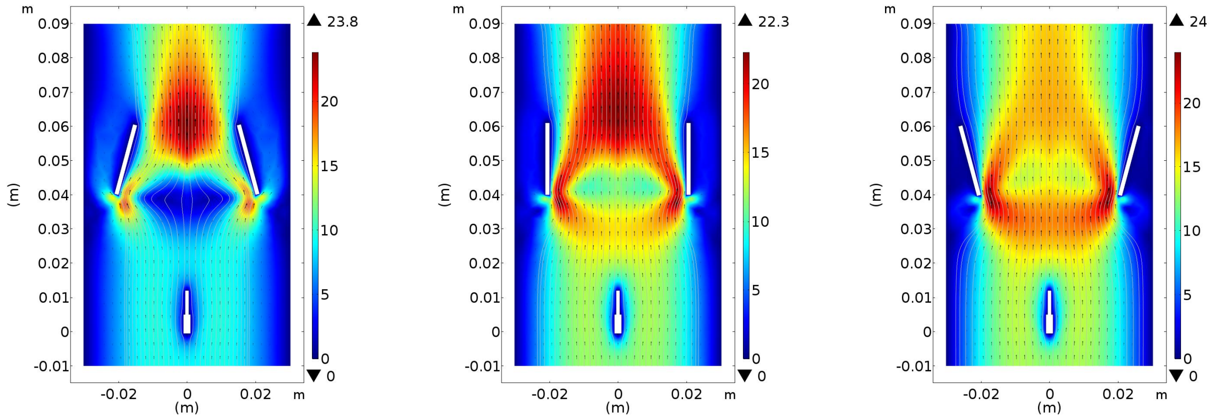

(a) (b) (c)

Figure 6.16: Two dimensional fluid velocity distribution cm $\cdot$ s^{-1} for different cone angles, with applied voltage of 20kV. (a) $-15°$, (b) $0°$ and (c) $15°$.

At the cathode's exit area, the plasma velocity also shows different patterns. We see from figure (6.17) that as long as the cone angle increases, the expelled velocity tends to flatten its maximum peak. As we were expecting from *Bernoulli*'s principle, the narrower cone delivers higher speeds, reaching values of nearly 24cm $\cdot$ s^{-1} regarding the wider cone that reaches only 17cm $\cdot$ s^{-1}.

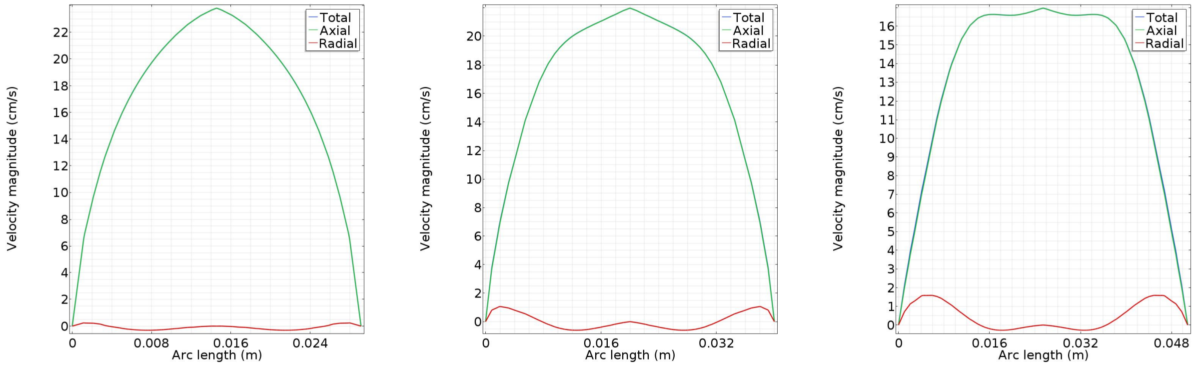

(a) (b) (c)

Figure 6.17: Fluid velocity components at cathode's exit cm $\cdot$ s^{-1} for different cone angles, with applied voltage of 20kV. (a) $-15°$, (b) $0°$ and (c) $15°$.

As for the thruster parameters, we assessed that at negative angles, the thruster would drop considerable, to nearly half, both its thrust and its thrust-to-power ratio and for positive angles, the cone cathode would improve slightly the thruster as we can observed in figure (6.18). From this point we can conclude that the use of the cylindrical cathode did not affect at all the development of this thruster. However the cone configurations could easily damage the cathode surface due to etching effects.

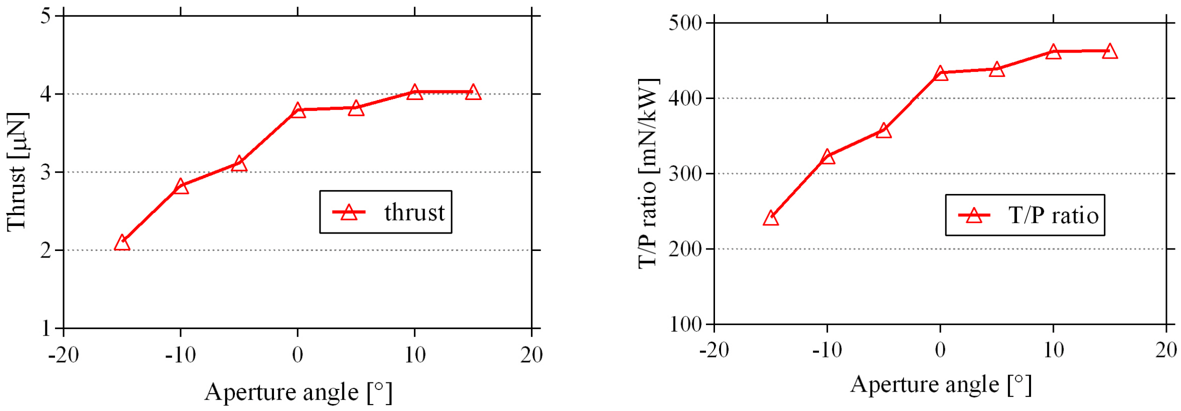

(a) (b)

Figure 6.18: Variation of xenon propellant thruster parameters for different cone angles ° at an applied voltage of 20kV. (a) output thrust μN, (b) thrust-to-power ratio mN/kW.

6.4 XENON DUAL STAGE EHD THRUSTER

In this section we expanded the dual stage EHD thruster by developing a new geometry concept. Since the design of the two-stage thruster separates control of ionization and acceleration, here we covered the needle-type anode with a hollow cylindrical anode and we maintained the same ground-cathode geometry. We set the γ_i coefficient at 6.87×10^{-4}, the dynamic viscosity for xenon as $\eta = 2.31$. The electric circuit parameters were also fixed, the applied voltage used was $V_0 = 20$kV, the ballast resistor was $R_b = 500\text{M}\Omega$ and the blocking capacitor was $C_b = 1$pF. The ring chapped electrode has similar dimensions as the cylindrical cathode, however its length was reduced in half, that is 10.5mm .

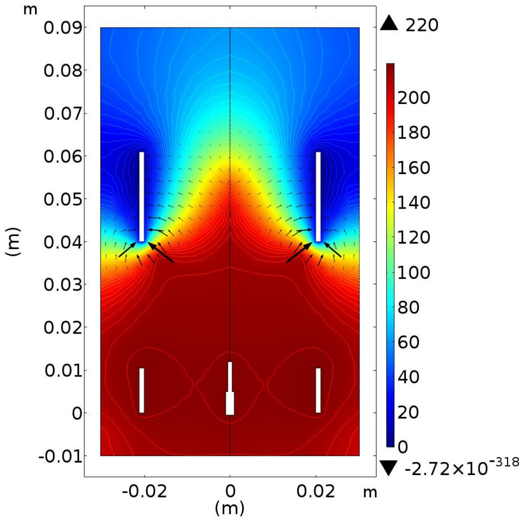

Figure 6.19: Electric potential distribution V for the dual stage xenon EHD thruster.

The electric potential for this thruster can be observed in figure (6.19). In comparison to the single stage, the use of a ring chapped electrode allowed an expansion in the high voltage plateau. Nevertheless, in the regions inside the cathode, we see that the electric gradient line as a similar shape to the xenon single stage thruster. However the particles distribution have different shapes, since we see a low region of neutral Xe atoms between the ring anode and the cylindrical cathode.

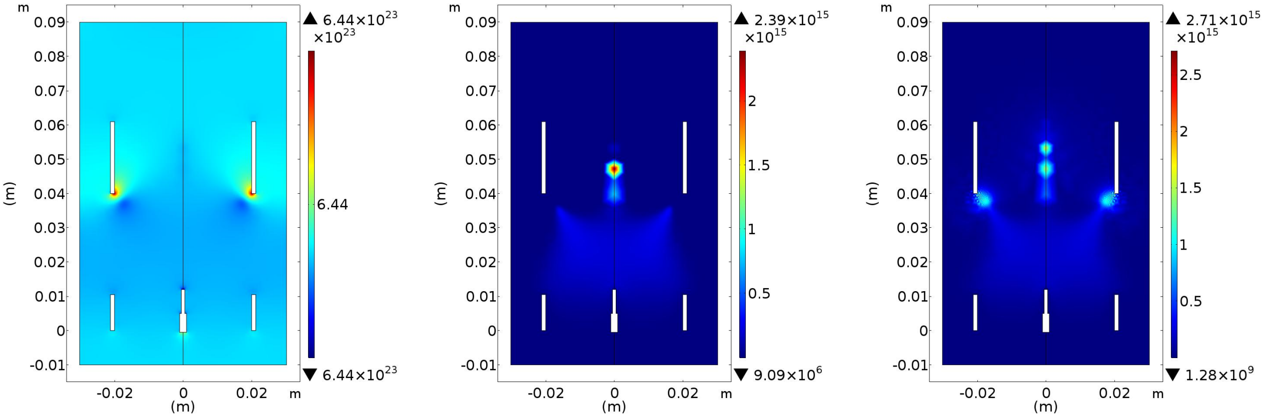

(a) (b) (c)

Figure 6.20: Particle densities m^{-3}. From the left to the right Xe neutral density, e^{-} density and Xe^{+} ion density.

In the meantime, at the same area, we see more charged particles, although they reached its maximum concentrations inside the cathode, reaching values of 2.39×10^{15}m^{-3} in the case of electrons and 2.71×10^{15}m^{-3} for the xenon ions. This traduces in a local maximum degree of ionization of $\approx 10^{-8}$. These results are displayed in figure (6.20).

In terms of fluid velocity we see that the plasma became more confined which allowed it to increase its speed inside the reactor chamber. Although the plasma managed to maintain its maximum speed values, 21cm $\cdot$ s^{-1}, its speed decreased drastically to 17cm $\cdot$ s^{-1} in the cathode's exit. The profile for the expelled fluid velocity has a rapid decay from the middle of the cathode to the surface, which in terms of thruster performance is not favourable. After evaluating the thruster performance we found out that this thruster delivered 2.22μN of net thrust and its efficiency was 254mN/kW.

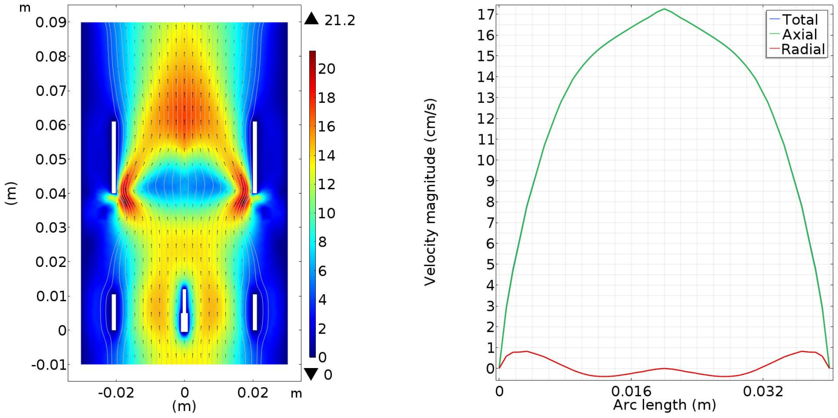

(a) (b)

Figure 6.21: Velocity profiles for the xenon dual stage EHD thruster cm · s^{-1}. (a) two dimensional fluid velocity profile (b) expelled fluid velocity at the cathode's exit.

6.5 CONCLUSIONS

The influence of the intrinsic geometry on the output rocket parameters has been studied in a EHD thruster plasma model. The goal was to find the best cathode length and inner radius that would produce the better net thrust and the better efficiency. Using Argon, we verified that the width was already optimized in 12mm, since any other variations, upper or lower, would decrease the output thrust and the thruster efficiency. On the opposite hand, when using Xenon, we concluded that the optimal hollow radius was 20mm since it resulted in a better output thrust and thruster efficiency.

Next, we proceeded to verify the influence of the cylinder length by decreasing its size and posteriorly increasing it again. At 20kV, we discovered that for Ar, the cylinder height should be halved, to around 10.5mm, and that for the Xe, the cylinder height should be reduced by about 30%, i.e. to 14.7mm. By observing this behaviour we concluded that a higher cathode would not be more efficient then a smaller one. Also, we found out that this geometry is not the same if the propellant gas differs. The numerical results were consistent with the ones produced in the previous studies and showed that Xenon is more efficient then Argon, since it has a higher atomic mass.

On our second approach we studied the influence of the secondary electron emission coefficient, and we found out that for a low value of γ_i, both thrust and thrust-to-power ratio would increase considerable relative to a higher coefficient. Then, the plasma was modulated to simulate γ_i with experimental values. The numerical simulations results proved once more that Xenon is more efficient then Argon.

Neutral Ar density

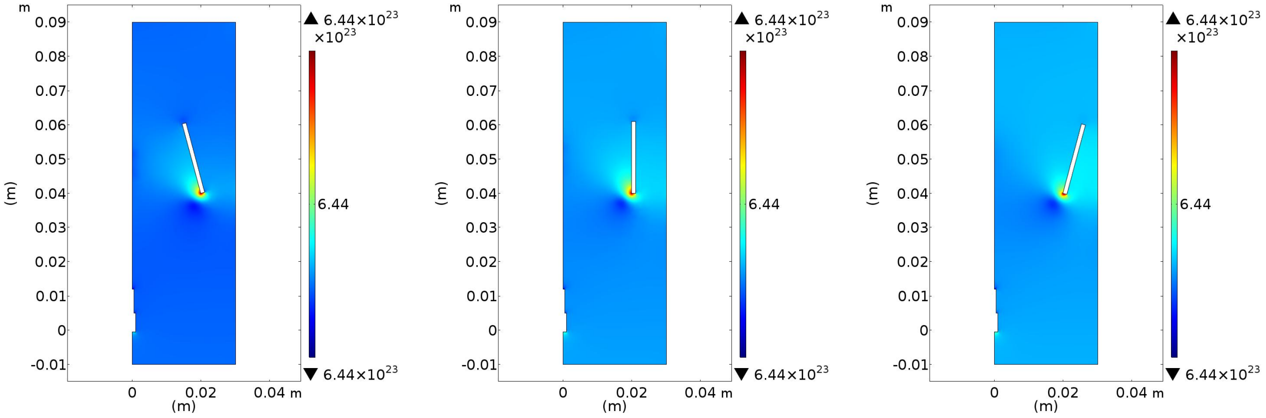

(a) (b) (c)

Electron density

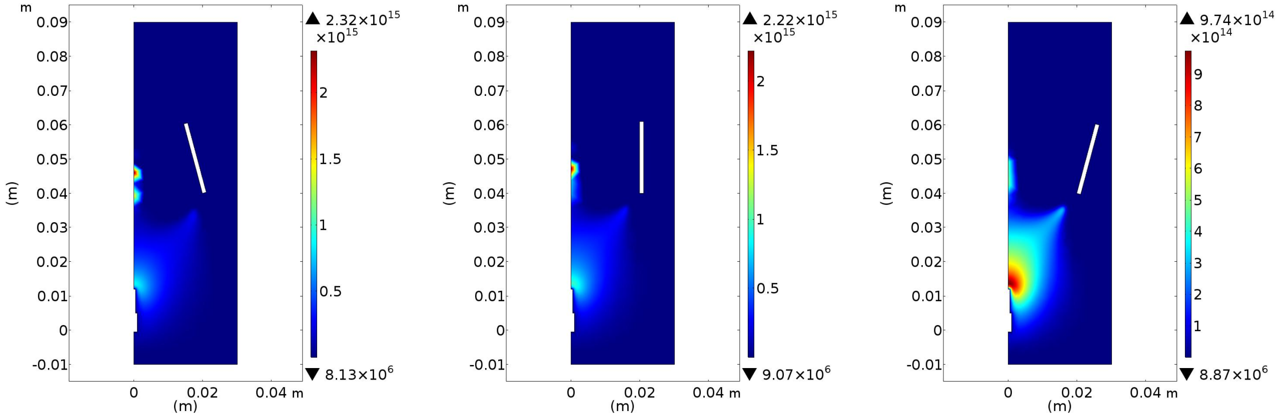

(d) (e) (f)

Ions density

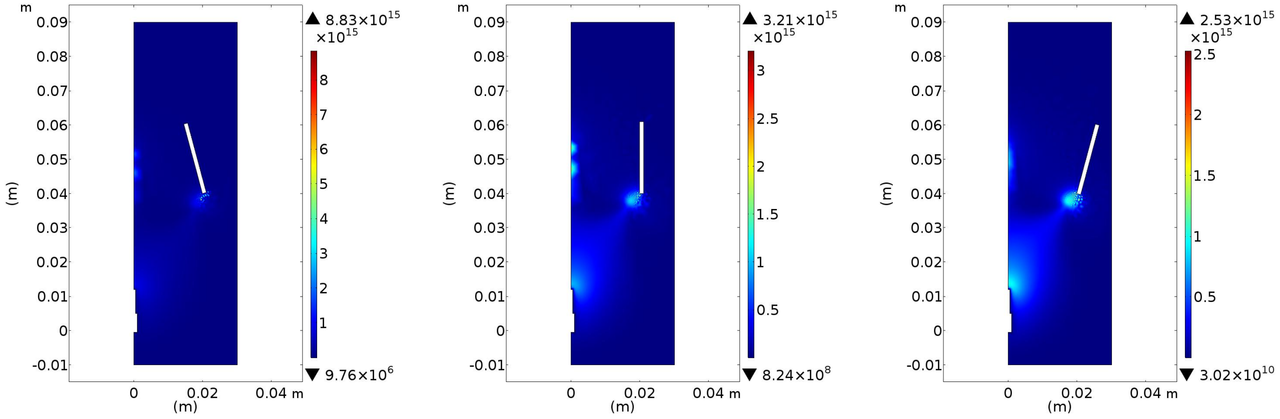

(g) (h) (i)

Figure 6.22: Particle densities m^{-3}, for different cone angles of a xenon propellant EHD thruster. (a,d,g) $-15°$, (b,e,h) $-0°$ and (c,f,i) $15°$. In the first row is shows the Xe neutral density, the second row presents the e^{-} density and the third row shows the Xe^{+} ion density.

Chapter 7.

Conclusions and Future work

This chapter presents the main conclusions drawn from improving the previous electrohydrodynamic thruster and possible future work that could be developed on the modulation and simulation of electric propulsion systems.

First we started by studying the external density force term in NSE that should be used in the modulation of an electrohydrodynamic thruster. By simulating different force terms, we concluded that the coulomb force term, ρ_c**E**, should be the one used, since it was the only one that provided a more physical consistency with the plasma discharge theory and, also important, could reduced simulation time.

We improved the previous thruster from the nano-Newtons range to the micro-Newtons by changing the discharge parameters, relative to those parameters previously used in the PhD Thesis of Granados. Now we used the following values, ballast resistor of 500MΩ, blocking capacitor of 1pF, an applied voltage of 20kV and the experimental values of the secondary electron emission coefficient $\gamma_i = 0.0009$. We also studied the effects of cathode's geometry and concluded that for the argon propellant single stage thruster, the inner radius of the cathode should be 12mm and the cathode's length should be 10.5mm.

Next we studied the plasma-sliding effect and we found out that this was a great method to improve the argon propellant EHD thruster for low applied voltages, that reached also the micro-Newton range with an applied voltage of 12kV. In this thruster we studied several parameters, such as the aperture angle, that we found out that it should be $30°$. We also studied the influence of the cathode's length, the applied voltage, and the secondary electron emission coefficient.

Finally we developed one main goal of this work, a argon propellant dual stage EHD thruster, where we studied two different configurations, the four electrodes and three electrodes. We concluded that the optimal configuration should be the three electrodes because we created two distinct regions, an acceleration potential region and a neutralization region. With xenon we develop a new concept, by introducing a needle anode covered by a ring anode with the same voltage.

The second main goal consisted in using xenon as the propellant gas for the EHD thruster. First we found out that the optimal cathode geometry was completely different from the argon thruster, as the optimal inner radius of the cathode should be 20mm and the cathode's length should be 14.7mm. We also studied the influence of the cylindrical aperture angle, and if we should use a cylinder or a cone as cathode. Here we found that both cylinder or cone would deliver similar results, however this last one could bring some mechanical issues due to etching and other effects that could rise up in the cathode's surface. Overall, the xenon thruster deliver the highest values we measures in this work, a thrust of 3.80μN and an efficiency of 450mN/kW. We can conclude that this objective was also achieved with great satisfaction because this results are currently used in the state-of-art.

For the future work we propose introducing a magnetic field across the cylindrical cathode, in order to capture electrons inside the cathode. This concept is already used in Hall-effect thrusters and potentially, the development of this thrust could be the future line of work as well.

Appendix A.

Physics behind the electrohydrodynamic processes

A.1 ELECTRON BOLTZMANN EQUATION AND TRANSPORT COEFFICIENTS

Each moment of the Boltzmann equation (BE) contains information on transport coefficients which are important when it is dealing with a gas discharge. Here we will focus on how to compute the distribution function for instance, on an ensemble of electrons in a ionized gas. The BE for electrons can be written as (Bittencourt (2004), Roth (1995), Krall et al. (1973), Boyd and Sanderson (2003)):

$$\frac{\partial f}{\partial t} + \mathbf{v} \cdot \nabla_{\mathbf{r}} f - \frac{e}{m_e}(\mathbf{E} + \mathbf{v} \times \mathbf{B}) \cdot \nabla_{\mathbf{v}} f = \left(\frac{\delta f}{\delta t}\right)_{coll} \tag{A.1}$$

where f is the electron distribution in phase space, v are the velocity coordinates, $\nabla_{\mathbf{r}}$ is the gradient operator in real space, on the other hand,$\nabla_{\mathbf{v}}$ is the gradient operator in the phase space. The constants e and m_e are, respectively, the electron elementary charge and mass, while **E** is the applied electric field and **B** are the applied magnetic field. The right side of the equation corresponds to the change of rate of the distribution function from collisions, either elastic, inelastic, superelastic and coulomb collisions. What we will present in this section follows closely the work of Hagelaar and Pitchford when they wrote an article explaining how their BE solver works, the *BOLSIG+,* and the physical theory behind it, such as the classical two-term expansion and equations to both transport and rate coefficients that are dependent on the Boltzamnn equation and collision cross-section information (Hagelaar and Pitchford (2005)).

This section will present a briefly summary of their theory and assumptions. To simplify the

Boltzmann equation, equation (A.1), it is assumed that magnetic field is turned off and the electric field is spatially uniform, then electron distribution function, f, is spherically symmetric in the phase space and it can be written as an expansion of two terms of Legendre polynomials (spherical harmonic expansion). Using a first order approximation, the distribution function is:

$$f(\mathbf{r}, \mathbf{v}, t) = f_0(\mathbf{r}, v, t) + f_1(\mathbf{r}, z, t)\cos\theta \tag{A.2}$$

where the quantity v represents the magnitude of the velocity vector and the angle θ is the angle between the velocity and the direction of the electric field. f_0 and f_1 represent the isotropic and anisotropic parts of f, respectively. Then f is normalized as

$$\int\int\int f(\mathbf{r}, \mathbf{v}, t)d^3v = 4\pi\int_0^{\infty} f_0(\mathbf{r}, \mathbf{v}, t)v^2dv = n_e(\mathbf{r}, t) \tag{A.3}$$

where $n_e(\mathbf{r}, t)$ is our first transport coefficient, the electron spatial density or **electron number density**.

Now the velocity part of the electron distribution function is suppose to be independent from the time and space. In the conditions of a weakly ionized gas, this method is often very good because of the domination of the collisions between electrons and neutral particles that are mainly elastic over most of the energy range (Lieberman and Lichtenberg (2005)). It is possible to apply a change in variables, i.e, the electron velocity v is changed into the electron energy ε, using the relation $v = \gamma(\varepsilon)^{1/2}$, where $\gamma = (2e/m_e)^{1/2}$. So the new distribution function can be written as:

$$f_j(\mathbf{r}, \mathbf{v}, t) = \frac{n_e(\mathbf{r}, t)}{2\pi\gamma^3}F_j(\varepsilon) \tag{A.4}$$

where the subscript j represents both the isotropic part of the Legendre function, $j = 0$ and the anisotropic part, $j = 1$. These two parts play a great role since the first one, F_0, corresponds to the electron energy distribution function (EEDF) and the second one, F_1, carries the electric mean velocity and the transport coefficients. The EEDF is usually normalized as:

$$\int_0^{\infty} \varepsilon^{1/2}F_0(\varepsilon)d\varepsilon = 1 \tag{A.5}$$

and the electric mean velocity, or the **drift velocity**, the most used term, is defined as

$$w = \frac{\gamma}{3} \int_0^\infty \varepsilon F_1(\varepsilon) d\varepsilon \tag{A.6}$$

Since the electrons drift against the electric field their movement and spatial density grow exponentially with a constant rate α, the **Townsend coefficient**, which is the symmetrical ratio of the **net production frequency** and the drift velocity.

$$\alpha = -\frac{\bar{\nu}_i}{w} \tag{A.7}$$

where $\bar{\nu}_i$ is the net production frequency which is defined as:

$$\bar{\nu}_i = N\gamma \int_0^\infty \left(\sum_{k=ionization} x_k \sigma_k - \sum_{k=attachment} x_k \sigma_k \right) \times \varepsilon F_0(\varepsilon) d\varepsilon \tag{A.8}$$

where N is the neutral gas density and the sums are over ionization and attachment reactions. The corresponding x_k and σ_k terms are both the mole fraction of the target species of the collision process and the collision process cross-section data, respectively.

Meanwhile, the **electron flux** can be defined as the product of the electron number density with the drift velocity, such as:

$$\Gamma = nw = \frac{\gamma}{3} n_e \int_0^\infty \varepsilon F_1(\varepsilon) d\varepsilon \tag{A.9}$$

where it leads to very important transport coefficients, the **reduced electron mobility**, $\mu_e N$, and the **reduce electron diffusion coefficient**, $D_e N$, which are given by:

$$\mu_e N = -\frac{\gamma}{3} n_e \int_0^\infty \frac{\varepsilon}{\tilde{\sigma}_m} \frac{\partial}{\partial \varepsilon} F_0(\varepsilon) d\varepsilon \tag{A.10}$$

$$D_e N = \frac{\gamma}{3} n_e \int_0^\infty \frac{\varepsilon}{\tilde{\sigma}_m} F_0(\varepsilon) d\varepsilon \tag{A.11}$$

where $\tilde{\sigma}_m$ is the effective momentum transfer cross-section, which is defined as $\tilde{\sigma}_m = \sigma_m + \bar{\nu}_i / N\gamma\varepsilon^{1/2}$ whereas σ_m is the total momentum cross-section, defined as the sum of all possible collision processes, k within the gas particles, i.e.

$$\sigma_m = \sum_k x_k \sigma_k \tag{A.12}$$

From collision processes it is also important to define the **rate coefficients** which as units of volume per time as:

$$k_k = \gamma \int_0^\infty \varepsilon \sigma_k F_0(\varepsilon) d\varepsilon \tag{A.13}$$

since they will perform an important role in the evaluation of continuity equations, after all they belong to the source terms.

A.2 THEORY OF THE ELECTROHYDRODYNAMIC DENSITY FORCE

The volume density force that acts on the neutral gas particles is equal to momentum transfer per unit volume and per unit time of the electric charged particles to the neutral particles. Since the average velocity of the neutral particles are much smaller then the drift velocities of the charged particles, then it is possible to write the volume density forces of ions, $\mathbf{f}_i$, and electrons, $\mathbf{f}_e$, as

$$\mathbf{f}_i = n_i m_i \nu_{in} \mathbf{u}_i \tag{A.14}$$

$$\mathbf{f}_e = n_e m_e \nu_{en} \mathbf{u}_e \tag{A.15}$$

where m_i, m_e are the ion mass and the electron mass respectively; ν_{in}, ν_{en} are the frequency of transference of momentum from ion-neutral or electron-neutral and $\mathbf{u}_i$ and $\mathbf{u}_e$ are the ion and electron drift velocities.

As it is known, the flow of a charge particle in an ionized gas is the product of the particle number density over the average particle velocity, so the ion and electron fluxes, $\mathbf{\Gamma}_i$ and $\mathbf{\Gamma}_e$ with SI units of m$^{-2}\cdot$ s^{-1}, can be written as (Bittencourt (2004)):

$$\mathbf{\Gamma}_i = n_i \mathbf{u}_i = n_i \mu_i \mathbf{E} - D_i \nabla n_i \tag{A.16}$$

$$\mathbf{\Gamma}_e = n_e \mathbf{u}_e = -n_e |\mu_e| \mathbf{E} - D_e \nabla n_e \tag{A.17}$$

In the set of equations (A.16) and (A.17), the variables μ_i and μ_e are the ion and electron mobility, which are related to the particle charge, particle mass and particle transference frequency, $\mu_j = e_j(m_j \nu_{jn})^{-1}$, where the j index indicates if its a positive or negative charge particle. The variables D_i and D_e are the ion and electron diffusivity respectively. Since the current density vector $\mathbf{J}$, with SI units of A$\cdot$m^{-3}, is computed directly by multiply the particle charge over the number density over the average particle velocity, then it is possible to relate this physical quantity with the particle flux

$$\mathbf{J}_i = e n_i \mathbf{u}_i = e\mathbf{\Gamma}_i = e n_i \mu_i \mathbf{E} - e D_i \nabla n_i \tag{A.18}$$

$$\mathbf{J}_e = -e n_e \mathbf{u}_e = e\mathbf{\Gamma}_e = e n_e |\mu_e| \mathbf{E} + e D_e \nabla n_e \tag{A.19}$$

According to Boeuf and Pitchford (2005), the force that acts on the ions and electrons is proportional to the current density vector, that is:

$$\mathbf{f}_i = e\frac{n_i}{\mu_i}\mathbf{u}_i = \frac{\mathbf{J}_i}{\mu_i} = e n_i \mathbf{E} - \frac{e D_i}{\mu_i}\nabla n_i \tag{A.20}$$

$$\mathbf{f}_e = -e\frac{n_e}{|\mu_e|}\mathbf{u}_e = -\frac{\mathbf{J}_e}{|\mu_e|} = -e n_e \mathbf{E} - \frac{e D_e}{|\mu_e|}\nabla n_e \tag{A.21}$$

through the *Einstein* relation, $eD_i/\mu_i = k_B T_i$ and $eD_e/|\mu_e| = k_B T_e$, where k_B is the *Boltzmann* constant and the variables T_i and T_e are respectively the ion and electron temperature given in [eV].

Since $\mathbf{f} = \mathbf{f}_i + \mathbf{f}_e$, we derived to the general expression for the density force, by adding equation (A.20) and (A.21), which results in

$$\mathbf{f} = e(n_i - n_e)\mathbf{E} - k_B T_i \nabla n_i - k_B T_e \nabla n_e \tag{A.22}$$

However a more complex deduction, which describes all the phenomena can be found in Bittencourt (2004). Overall, a general equations can be deduced by a set of partial differential equations that describe both temporal and spatial variation through the Boltzmann momentum equations. First, let us assume that f_α is the Boltzmann function for a particle α, where $\alpha = i, e$ then continuity equation is simply given by

$$\frac{\partial \rho_{m\alpha}}{\partial t} + \nabla \cdot (\rho_{m\alpha} \mathbf{u}_\alpha) = m_\alpha S_\alpha \tag{A.23}$$

where $\rho_{m\alpha} = n_\alpha m_\alpha$ is the mass density, $\mathbf{u}_\alpha$ is the α-particle's mean velocity and S_α is a collision term, defined as

$$S_\alpha = \int_v \left(\frac{\delta f_\alpha}{\delta t} \right)_{coll} = \left(\frac{\delta n_\alpha}{\delta t} \right)_{coll} \tag{A.24}$$

The physical meaning of this term is the rate per unit volume which particles of type α (with mass m_α) are created or destroyed as result of collisions. There are several processes but they usually are related to inelastic collisions, such as ionization, recombination, or attachment.

The momentum transport equation, in its general form can be written as

$$\rho_{m\alpha} \left[\frac{\partial \mathbf{u}_\alpha}{\partial t} + (\mathbf{u}_\alpha \cdot \nabla)\mathbf{u}_\alpha \right] + \nabla \cdot P_\alpha - n_\alpha < \mathbf{F} >_\alpha = \mathbf{A}_\alpha - m_\alpha \mathbf{u}_\alpha S_\alpha \tag{A.25}$$

where P_α is the pressure tensor, $\mathbf{F}$ is the external force term applied to the α particles and $\mathbf{A}_\alpha$ is a the rate of change of the mean momentum per unit volume, due to collisions. The first two terms in the left side of equation (A.25) correspond to the total time derivative operator D/Dt.

Meanwhile the divergence of the pressure tensor represents the force exerted in a unit volume of the plasma, due to random variations in the particle velocities. This term includes forces which are associated with the scalar pressure and tangential shear stress. When the fluid is isotropic, the viscosity effects can be neglected, the non diagonal terms of P_α are zero and the diagonal terms are all equal, corresponding also to the scalar kinetic pressure. So the force per unit volume becomes $\nabla \cdot P_\alpha = \nabla p_\alpha$, whereas $p_\alpha = n_\alpha k_B T_\alpha$

If we consider that our particles are inside an electric field, the external force term, which is the fourth term in the left side of the equation (A.25), corresponds simply to the *Coulomb* force, then this terms become $n_\alpha < \mathbf{F} >_\alpha = n_\alpha q_\alpha \mathbf{E}$, where q_α is the particle charge and **E** is the applied electric field.

The first term in the right side, the rate of change of the mean momentum per unit volume, can be express as

$$\mathbf{A}_\alpha = -\rho_{m\alpha} \sum_\beta \nu_{\alpha\beta}(\mathbf{u}_\alpha - \mathbf{u}_\beta) \tag{A.26}$$

which assume that the force exerted on α particles due to collisions with β particles is proportional to the difference between their mean velocities or mean relative velocity between the two types of particles, where the proportionality constant is defined as the **collision frequency for momentum transfer** between these types of particles, having dimensions of s^{-1}.

With these simplifying approximations, the momentum equation becomes

$$\rho_{m\alpha} \frac{D\mathbf{u}_\alpha}{Dt} = n_\alpha q_\alpha \mathbf{E} - \nabla p_\alpha - m_\alpha \mathbf{u}_\alpha S_\alpha - \rho_{m\alpha} \sum_\beta \nu_{\alpha\beta}(\mathbf{u}_\alpha - \mathbf{u}_\beta) \tag{A.27}$$

Physically, this expression states that a time rate of the mean momentum, in each fluid element is produced by an external force term, in this case a *Coulomb* force, by shear and pressure forces of the fluid itself, internal forces from collision interactions and the forces from inelastic collisions.

The generation of electric charge particles by ionization processes in a collisional plasma can be responsible for creation of a volume density force generation (in the direction of the charged particle motion), even when the plasma is neutral and uniform. This force is called charged-particle momentum divergence force and was studied in detail by Leiby and Oskam (1969).

Consider a plasma in the steady-state and consider that $\beta = n$, if the mean velocity of the neutral particles with respect the the charged particles is neglected, $\mathbf{u}_n = 0$, the electron momentum-transfer equation, $\alpha = e$, can be written as

$$0 = -|e|n_e\mathbf{E} - \nabla(n_e k_B T_e) - m_e\mathbf{u}_e S_e - n_e m_e \nu_{en}\mathbf{u}_e \tag{A.28}$$

Taking the same operations, the ion momentum-transfer equation, $\alpha = i$, can be written as

$$0 = |e|n_i\mathbf{E} - \nabla(n_i k_B T_i) - m_i\mathbf{u}_i S_i - n_i m_i \nu_{in}\mathbf{u}_i \tag{A.29}$$

The last terms in this set of equations, correspond to the electron and ion forces per unit volume, that is $\mathbf{f}_e = n_e m_e \nu_{en}\mathbf{u}_e$ and $\mathbf{f}_i = n_i m_i \nu_{in}\mathbf{u}_i$. Since the momentum transferred per unit volume and per unit time from charged particles to neutral molecules corresponds to the force acting on the neutral gas comes form the collision from the charged particles, then the final expression for the electrohydrodynamic force is

$$\mathbf{f} = e(n_i - n_e)\mathbf{E} - k_B T_i \nabla n_i - k_B T_e \nabla n_e - m_i\mathbf{u}_i S_i - m_e\mathbf{u}_e S_e \tag{A.30}$$

A.3 THEORY OF THE EHD OUTPUT THRUST

To compute the output of the thrust, equation (3.31) in page (37), we integrate the force over the cylindrical area in exit of the cathode. As it was explain, an element of propulsion force $d\mathbf{F}_{prop}$ can be written as

$$d\mathbf{F}_{prop} = M\frac{d\mathbf{v}}{dt} = \mathbf{v}_{ex}\frac{dM}{dt} \tag{A.31}$$

The variation of propellant mass that are being expelled, dM at the cathode's exit is an element over the surface area, that is

$$dM = \rho_f z dA = \rho_f (u_{ex} dt) dA \tag{A.32}$$

where ρ_f is the fluid mass density, z is the azimuthal component and dA is an element of area of the cathode's exit.

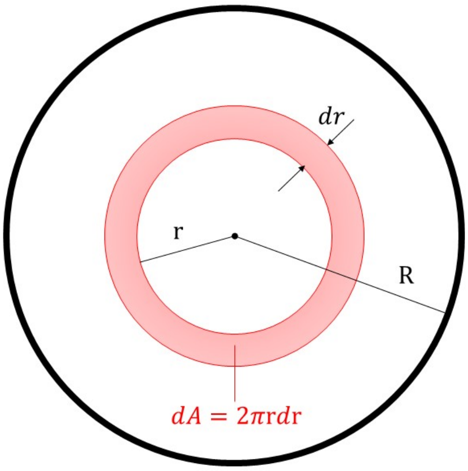

Figure A.1: Schematic of an element of area, dA, within the cathode's exit.

Substituting the expression of dA into the expression of dM we get

$$dM = \rho_f (u_{ex} dt)(2\pi r dr) \tag{A.33}$$

and rearranging now this equation we get a final expression for the dM/dt:

$$\frac{dM}{dt} = 2\pi \rho_f u_{ex} r dr \tag{A.34}$$

If we integrate this expression over the inner radius of the cathode's exit, that is from $r = 0$ to $r = R$, we get the total magnitude value of the output thrust. Since $u_{ex} = v_z(r)$, then :

$$T = 2\pi \rho_f \int_0^R r v_z^2(r) dr \tag{A.35}$$

Bibliography

Almeida, P. G. C. and Benilov, M. S.: 2013, Multiple solutions in the theory of direct current glow discharges: Effect of plasma chemistry and nonlocality, different plasma-producing gases, and 3d modelling, *Physics of Plasmas* **20**(10), 101613.

Auday, G., Guillot, P., Galy, J. and Brunet, H.: 1998, Experimental study of the effective secondary emission coefficient for rare gases and copper electrodes, *Journal of Applied Physics* **83**(11), 5917–5921.

Bedolla, P., Vorlaufer, G., Sequard-Base, P., Vernes, A. and Franek, F.: 2017, Altitude dependence of electrohydrodynamic flow in an electrostatic lifter, *Journal of Electrostatics* **87**, 32 – 44.

Bettinger, R. A. and Black, J. T.: 2014, Mathematical relation between the hohmann transfer and continuous-low thrust maneuvers, *Acta Astronautica* **96**, 42 – 44.

Biagi: 2019, database www.lxcat.net. retrieved on october 10.

Bittencourt, J. A.: 2004, *Fundamentals of Plasma Physics*, 3 edn, Springer-Verlag New York.

Boeuf, J.-P.: 2017, Tutorial: Physics and modeling of hall thrusters, *Journal of Applied Physics* **121**(1), 011101.

Boeuf, J. P., Lagmich, Y., Unfer, T., Callegari, T. and Pitchford, L. C.: 2007, Electrohydrodynamic force in dielectric barrier discharge plasma actuators, *Journal of Physics D: Applied Physics* **40**(3), 652–662.

Boeuf, J. P. and Pitchford, L. C.: 2005, Electrohydrodynamic force and aerodynamic flow acceleration in surface dielectric barrier discharge, *Journal of Applied Physics* **97**(10), 103307.

Bogaerts, A. and Gijbels, R.: 1995, Modeling of metastable argon atoms in a direct-current glow discharge, *Phys. Rev. A* **52**, 3743–3751.

Boyd, T. J. M. and Sanderson, J. J.: 2003, *The Physics of Plasmas*, Cambridge University Press.

Cannat, F., Lafleur, T., Jarrige, J., Chabert, P., Elias, P.-Q. and Packan, D.: 2015, Optimization of a coaxial electron cyclotron resonance plasma thruster with an analytical model, *Physics of Plasmas* **22**(5), 053503.

Chang Díaz, F., Carr, J., Johnson, L., Johnson, W., Genta, G. and Maffione, P. F.: 2019, Solar electric propulsion for human mars missions, *Acta Astronautica* **160**, 183 – 194.

Charles, C.: 2009, Plasmas for spacecraft propulsion, *Journal of Physics D: Applied Physics* **42**(16), 163001.

Conde, L., Domenech-Garret, J. L., Donoso, J. M., Damba, J., Tierno, S. P., Alamillo-Gamboa, E. and Castillo, M. A.: 2017, Supersonic plasma beams with controlled speed generated by the alternative low power hybrid ion engine (alphie) for space propulsion, *Physics of Plasmas* **24**(12), 123514.

Crofton, M. W. and Hain, T. D.: 2007, Environmental Considerations for Xenon Electric Propulsion, pp. 1–30.

Curtis, H.: 2019, *Orbital Mechanics for Engineering Students*, 4th edn, Butterworth-Heinemann.

El-Sayed, A. F.: 2016, *Rocket Propulsion*, Springer London, London, pp. 907–991.

Felicetti, L. and Santoni, F.: 2013, Nanosatellite swarm missions in low earth orbit using laser propulsion, *Aerospace Science and Technology* **27**(1), 179 – 187.

Fitzwilson, R. L. and Chanin, L. M.: 1973, Positive ion ratio measurements in ar, kr, and xe glow discharges, *Journal of Applied Physics* **44**(12), 5337–5346.

Fylladitakis, E. D., Theodoridis, M. P. and Moronis, A. X.: 2014, Review on the history, research, and applications of electrohydrodynamics, *IEEE Transactions on Plasma Science* **42**(2), 358–375.

Goebel, D. M. and Katz, I.: 2008, *Fundamentals of Electric Propulsion: Ion and Hall Thrusters*, John Wiley & Sons, Inc.

Gousset, G., Ferreira, C. M., Pinheiro, M., Sa, P. A., Touzeau, M., Vialle, M. and Loureiro, J.: 1991, Electron and heavy-particle kinetics in the low pressure oxygen positive column, *Journal of Physics D: Applied Physics* **24**(3), 290–300.

Granados, V.: 2018, *Modelling and simulation of plasma thrusters for electric propulsion technologies*, PhD thesis, Faculty of Engeneering of University of Porto.

Granados, V. H., Pinheiro, M. J. and Sá, P. A.: 2016, Electrostatic propulsion device for aerodynamics applications, *Physics of Plasmas* **23**(7), 073514.

Granados, V. H., Pinheiro, M. J. and Sá, P. A.: 2017, Study of the design and efficiency of single stage ehd thrusters at the sub-atmospheric pressure of 1.3 kpa, *Physics of Plasmas* **24**(12), 123513.

Griffiths, D. J.: 2013, *Introduction to electrodynamics*, 4ed. edn, Pearson, Addison-Wesley.

Hagelaar, G. J. M. and Pitchford, L. C.: 2005, Solving the boltzmann equation to obtain electron transport coefficients and rate coefficients for fluid models, *Plasma Sources Science and Technology* **14**(4), 722–733.

Henninger, H. C.: 2015, *Study of the solutions of low-thrust orbital transfers on the two and three body problem*, PhD thesis, Nice Sophia Antipolis University.

Holste, K., Dietz, P., Scharmann, S., Keil, K., Henning, T., Zschätzsch, D., Reitemeyer, M., Nauschütt, B., Kiefer, F., Kunze, F., Zorn, J., Heiliger, C., Joshi, N., Probst, U., Thüringer, R., Volkmar, C., Packan, D., Peterschmitt, S., Brinkmann, K. T., Zaunick, H.-G., Thoma, M. H., Kretschmer, M., Leiter, H. J., Schippers, S., Hannemann, K. and Klar, P. J.: 2020, Ion thrusters for electric propulsion: Scientific issues developing a niche technology into a game changer, *Review of Scientific Instruments* **91**(6), 061101.

Hoskins, W. A., Cassady, R. J., Morgan, O., Myers, R. M., Wilson, F., King, D. Q. and de Grys, K.: 2013, 30 Years of Electric Propulsion Flight Experience at Aerojet Rocketdyne, *Iepc-2013* p. 439.

Jahn, R. G.: 2006, *Physics of electric propulsion*, Courier Corporation.

Jamil, Y., Saeed, H., Raza Ahmad, M., Ahmad Khan, S., Farooq, H., Shahid, M., Zia, K. M. and Amin, N.: 2013, Measurement of ablative laser propulsion parameters for aluminum, CoNi ferrite and polyurethane polymer, *Applied Physics A* **110**(1), 207–210.

Johnson, L., Whorton, M., Heaton, A., Pinson, R., Laue, G. and Adams, C.: 2011, Nanosail-d: A solar sail demonstration mission, *Acta Astronautica* **68**(5), 571 – 575. Special Issue: Aosta 2009 Symposium.

Johnson, T. H., Cartland, H. E., Genoni, T. C. and Hunter, A. M.: 1989, A comprehensive kinetic model of the electronbeamexcited xenon chloride laser, *Journal of Applied Physics* **66**(12), 5707–5725.

Kahnfeld, D., Duras, J., Matthias, P., Kemnitz, S., Arlinghaus, P., Bandelow, G., Matyash, K., Koch, N. and Schneider, R.: 2019, Numerical modeling of high efficiency multistage plasma thrusters for space applications, *Reviews of Modern Plasma Physics* **3**(1), 11.

Keidar, M., Zhuang, T., Shashurin, A., Teel, G., Chiu, D., Lukas, J., Haque, S. and Brieda, L.: 2014, Electric propulsion for small satellites, *Plasma Physics and Controlled Fusion* **57**(1), 014005.

Kindracki, J., Paszkiewicz, P. and ukasz Myk: 2019, Resistojet thruster with supercapacitor power source design and experimental research, *Aerospace Science and Technology* **92**, 847 – 857.

Kluever, C. A.: 2015, Designing transfers to geostationary orbit using combined chemicalelectric propulsion, *Journal of Spacecraft and Rockets* **52**(4), 1144–1151.

Krall, N., Trivelpiece, A. and Kempton, J.: 1973, *Principles of Plasma Physics*, International series in pure and applied physics, McGraw-Hill.

Leiby, C. C. and Oskam, H. J.: 1969, Axial pressure gradient in directcurrent discharges, *The Physics of Fluids* **12**(11), 2449–2451.

Levchenko, I., Xu, S., Teel, G., Mariotti, D., Walker, M. L. R. and Keidar, M.: 2018, Recent progress and perspectives of space electric propulsion systems based on smart nanomaterials, *Nature Communications* **9**(1), 879.

Lieberman, M. and Lichtenberg, A.: 2005, *Principles of Plasma Discharges and Materials Processing*, Wiley.

Loureiro, J. and Amorim, J.: 2016, *Fundamentals of Electrical Gas Discharges*, Springer International Publishing, Cham, pp. 3–41.

Loureiro, J. and Ferreira, C. M.: 1986, Coupled electron energy and vibrational distribution functions in stationary n2discharges, *Journal of Physics D: Applied Physics* **19**(1), 17–35.

Marić, D., Savić, M., Sivoš, J., Škoro, N., Radmilović-Radjenović, M., Malović, G. and Petrović, Z. L.: 2014, Gas breakdown and secondary electron yields, *The European Physical Journal D* **68**(6), 155.

Martins, A. A.: 2013, Modelling of an improved positive corona thruster and actuator, *Journal of Electrostatics* **71**(1), 61 – 67.

Masuyama, K. and Barrett, S. R. H.: 2013, On the performance of electrohydrodynamic propulsion, *Proceedings of the Royal Society A: Mathematical, Physical and Engineering Sciences* **469**(2154), 20120623.

Mathew, P., George, J., Mathews T, S. and Kurian, P. J.: 2019, Experimental verification of modified paschens law in dc glow discharge argon plasma, *AIP Advances* **9**(2), 025215.

Mazouffre, S.: 2016, Electric propulsion for satellites and spacecraft: established technologies and novel approaches, *Plasma Sources Science and Technology* **25**(3), 033002.

Mazouffre, S. and Grimaud, L.: 2018, Characteristics and performances of a 100-w hall thruster for microspacecraft, *IEEE Transactions on Plasma Science* **46**(2), 330–337.

Miernik, J., Statham, G., Fabisinski, L., Maples, C. D., Corp, Q. and Percy, T.: 2011, FUSION PROPULSION Z-PINCH ENGINE CONCEPT, *NASA, George C. Marshall Space Flight Center. ED04/Advanced Concepts Office* **7**.

Morgan: 2015, database www.lxcat.net. retrieved on january 25.

Munson, B., Young, D. and Okiishi, T.: 2005, *Fundamentals of Fluid Mechanics*, Wiley.

Mushyam, A., Rodrigues, F. and Pascoa, J.: 2019, A plasma-fluid model for ehd flow in dbd actuators and experimental validation, *International Journal for Numerical Methods in Fluids* **90**(3), 115–139.

O'Malley, T. F., Cunningham, A. J. and Hobson, R. M.: 1972, Dissociative recombination at elevated temperatures. II. Comparison between theory and experiment in neon and argon afterglows, *Journal of Physics B: Atomic and Molecular Physics* **5**(11), 2126–2133.

Plasma Module Users Guide: n.d.

Power, J. L.: 1992, Microwave electrothermal propulsion for space, *IEEE Transactions on Microwave Theory and Techniques* **40**(6), 1179–1191.

Rafalskyi, D. and Aanesland, A.: 2019, Development and Testing of the NPT30-I2 Iodine Ion Thruster, *the 36th International Electric Propulsion Conference* pp. 1–11.

Raizer, Y., Kisin, V. and Allen, J.: 2011, *Gas Discharge Physics*, Springer Berlin Heidelberg.

Roth, J. R.: 1995, *Industrial Plasma Engineering: Volume 1: Principles*, 1 edn.

Roth, J. R.: 2001, *Industrial Plasma Engineering, Volume 2: Applications to Nonthermal Plasma Processing*, CRC Press.

Salgado, M. C. V., Belderrain, M. C. N. and Devezas, T. C.: 2018, Space Propulsion: a Survey Study About Current and Future Technologies, *Journal of Aerospace Technology and Management* **10**.

Sangregorio, M., XIE, K., WANG, N., GUO, N. and ZHANG, Z.: 2018, Ion engine grids: Function, main parameters, issues, configurations, geometries, materials and fabrication methods, *Chinese Journal of Aeronautics* **31**(8), 1635 – 1649.

Shvydky, A., Nagorny, V. P. and Khudik, V. N.: 2004, Electron avalanche sliding along a dielectric surface, *Journal of Physics D: Applied Physics* **37**(21), 2996–2999.

Smirnov, B. M.: 2008, *Reference Data on Atomic Physics and Atomic Processes*, Springer Series on Atomic, Optical, and Plasma Physics 51, 1 edn, Springer-Verlag Berlin Heidelberg.

Torres, C., Reyes, P. G., Castillo, F. and Martínez, H.: 2012, Paschen law for argon glow discharge, *Journal of Physics: Conference Series* **370**, 012067.

Townsend, John, S.: 1910, *The theory of ionization of gases by collision*, London :Constable,.

Turner, M. J. L.: 2009, *Rocket and Spacecraft Propulsion: Principles, Practice and New Developments*, 3 edn, Springer-Verlag Berlin Heidelberg.

Walker, M. L., Russell, R. P. and Singh, L. A.: 2012, Utilization of residual helium to extend satellite lifetimes and mitigate space debris, *Journal of Propulsion and Power* **28**(6), 1406–1412.

Wollenhaupt, B., Le, Q. H. and Herdrich, G.: 2018, Overview of thermal arcjet thruster development, *Aircraft Engineering and Aerospace Technology* **90**(2), 280–301.

Yildiz, M. S. and Celik, M.: 2017, Numerical investigation of the electric field distribution and the power deposition in the resonant cavity of a microwave electrothermal thruster, *AIP Advances* **7**(4), 045021.

Zhang, Y., Wu, J., Ou, Y., Li, J. and Tan, S.: 2019, Modified electromechanical modeling and parameters analysis of magnetoplasmadynamic thruster, *Energies* **12**(12).